LONGSHORE VARIABILITY IN DUNE EROSION

MODELLING THE COUPLING BETWEEN OUTER BAR MORPHOLOGY AND DUNE EROSION USING XBEACH

J.P.M. Verdoes, 6628664
First supervisor: Dr. T.D. Price
Second supervisor: Prof. Dr. B.G. Ruessink
13-06-2021

Utrecht University
Faculty of Geosciences
Department of Physical Geography
Msc Earth, Surface Water

The Sea of Faith
Was once, too, at the full, and round earth's shore
Lay like the folds of a bright girdle furled.
But now I only hear
Its melancholy, long, withdrawing roar,
Retreating, to the breath
Of the night-wind, down the vast edges drear
And naked shingles of the world.

Matthew Arnold (1867)

Cover images: Upper image, Castelle et al. (2015). Bottom image, de Winter et al. (2015)

Abstract

Dunes are often a first line of defence against the against storm impact in coastal regions. It is therefore important to understand the driving processes of dune erosion. As Castelle et al. (2015) observed in the field, longshore variation in dune erosion can be coupled to the outer bar morphology. In this research a crescentic outer bar in a 2DH XBeach domain is combined with a uniform dune topography based on Egmond aan Zee, the Netherlands. Storm conditions consist of time-constant and time-varying wave height and angle of incidence. These conditions are simulated in XBeach using both the multi-dir method (Roelvink et al. 2009) and the single-dir method (Roelvink et al. 2018).

The hydrodynamic processes in the nearshore area are coupled to the outer bar morphology. Under small wave angles, the currents are characterized by a cell-circulation pattern with rips over the outer bar bays. As the wave angle becomes larger, the importance of the longshore component of the mean current increases with a meandering longshore current under a 45° wave angle as a result.

More erosion is observed on locations where the longshore current is strongest. This determines the location where the slope steepens the most and as a result avalanches occur. Under a 0° wave angle a relatively high dune erosion is observed at longshore location with an outer bar bay. These locations shift downstream in the longshore dimension under larger wave angles.

The infra-gravity wave energy at the dune of the foot is distributed in a crest-trough pattern in the longshore dimension, with high values (crests) at locations where a bay is present in the outer bar. The infra-gravity waves contribute considerably to the total water level and therefor to the magnitude of avalanching events.

Longshore variation in dune erosion is driven by the current and the total water level. A coupling between the outer bar morphology and longshore variable dune erosion using XBeach is confirmed.

The single-dir method leads to more erosion as a result of a stronger longshore current and larger infra-gravity wave heights, leading to a higher longshore maximum total water level. The magnitude of the avalanche events in the single-dir method is larger compared to the multi-dir method, this might be the result of larger infra-gravity wave heights in the single-dir method, due to less directional spreading of short-wave groups.

Contents

1. Introduction

1.1 Defining the problem

Coastal dunes are common features on wave-dominated coasts all around the world. They often are the first line of defence against flooding by the sea, protecting population against storm conditions. This is also the case in the Netherlands, where 45.000 ha of coastal dunes protect the hinterland against flooding (Arens et al., 2013). Storms can have large impacts on the dunes, eroding large volumes of sediment in a couple of hours. It is therefore essential to understand the erosional processes. With a predicted increase in future extreme storm surges in the North Sea due to climate change (Woth et al., 2005), it is also of great importance to manage our coastal defences to be prepared for hazardous situations.

Over the years, a lot of research has been done on dune erosion (Vellinga, 1982, van Gent et al., 2008, Nishi & Kraus, 1996). Studying the impact of storms on the dune front in the field brings logistic challenges. Therefore, numerical models can be used as a tool to understand the processes during storm conditions and predict the loss of dune volume in the future. In 2009, Roelvink et al. developed XBeach as a process-based model and has since been used for multiple coastal implications. The original surfbeat mode solves hydrodynamic process, averaged over depth for a horizontal two-dimensional area. More research suggested that the model underpredicted the contribution of infragravity waves to the set-up (Palmsten & Splinter, 2016). As infragravity waves are an important factor in swash dynamics (Guza & Thornton, 1982), an accurate prediction of the infragravity contribution is important. Therefore, Roelvink et al. 2018 developed a new numerical scheme to adjust the directional spread of short-wave groups.

As the observations of Castelle et al. (2015) suggest, the bathymetry can lead to a variability in longshore dune erosion by influencing the wave field as it propagates towards the shore. To understand this variation in dune erosion, first a domain is constructed based on Egmond aan Zee. XBeach can then be used to acquire an understanding of the processes over a variable bathymetry, which in reality occur under high energy conditions. This research focuses specifically on the hydrodynamic characteristics driving the longshore variability under different storm conditions over a crescentic sandbar. A detailed look to the longshore components of XBeach is obtained to build on the research of van Thiel De Vries et al. (2011). Also, the implications of the new numerical scheme by Roelvink et al. (2018) (single-dir) available in XBeach on these longshore components is implemented.

2. Literature Review

The main focus of this thesis is on the processes driving dune erosion at Egmond aan Zee using the numerical model XBeach. As hydrodynamic conditions vary, the output generated by XBeach can be used to study the distribution of the high and low frequency energy and their effects on the processes in the nearshore throughout a storm. In order to analyse the results of the model, an understanding of physical processes is essential.
In this chapter, the most dominant processes inherent to the topic of this thesis will be discussed. One of the main elements in studying coastal morphology is the hydrodynamical conditions in the coastal region. Within the framework of the hydrodynamic conditions, the focus will be on the understanding the behaviour of infragravity waves, short waves and mean currents and the relation with the morphological characteristics of the coastline, with an emphasis on Egmond aan Zee features.
Subsequently, the impact on coastal dunes during storms will be evaluated together with the erosional mechanisms observed at the dune front.
Finally, different ways to model dune erosion will be evaluated. Multiple studies, in which XBeach is used, are reviewed in order to evaluate its skill in modelling coastal behaviour. The framework used by XBeach to model these physical processes, is clarified in appendix A.

2.1 Hydrodynamic conditions

2.1.1 Infragravity waves

When considering the hydrodynamic conditions on low sloping beaches, the dynamics of infragravity waves (IG waves) play an important role. IG waves are defined as waves with a frequency between 0.04 and 0.004 Hz and potential wavelengths of up to a kilometre (Bertin et al., 2018).
In current research, three main generation mechanisms can be distinguished. The first mechanism occurs in deep water. Here IG waves are the result of differences in radiation stress caused by short wave groups. Radiation stress is defined as the force exerted on an obstacle due to a gradient in flow of wave momentum. High waves in a wave group produce a higher flow of momentum in the direction of propagation. The relatively high flow of momentum results in a higher level of radiation stress. This is manifested in a force exerted on the water. This force pushes the water level down.
To preserve continuity, the water level rises where the waves of the group are small, and the radiation stress is relatively low.
The observed difference in water level over the length of a wave group can be seen as a low frequency wave (Longuet-Higgins & Stewart, 1964) (Figure 1). The created IG wave is ‘bound’ to the wave group. The mathematical derivation of radiation stress used by XBeach is included in section 9.1.

Another mechanism generating IG waves is based on the moving breakpoint of incoming wave groups. As the incoming wave group approaches the shore, high waves start to break in deeper water than smaller waves. The point where the waves break therefore shifts over the length of a wave group. This means that the radiation stress, as the result of breaking, shifts over time in the cross-shore dimension. The created difference in water level is a ‘free’ IG wave as well (Symonds et al., 1982, Schäffer, 1993).
Van Dongeren et al. (2007) argued that the relative importance of the driving mechanisms depends on the slope of the beach. On steep sloping beaches (1:10), the moving breakpoint mechanism is expected to be dominant. While on mild sloping beaches such as Egmond aan Zee (1:30), the incoming bound IG waves strongly determine the IG energy (Van Dongeren et al., 2003).

Some studies have also suggested a transfer of energy towards higher frequencies as a result of 'bore merging' in the inner-surf zone. Consecutive bores, produced by breaking waves, overtake each other and merge in the process. This leads to an increase of wave period in the surf zone and therefore an increase in energy in the low-frequency spectrum (Bertin et al., 2018). This phenomenon has proven to be less dominant in driving IG waves than the breaking-point and wave group mechanisms (Tissier et al., 2017).

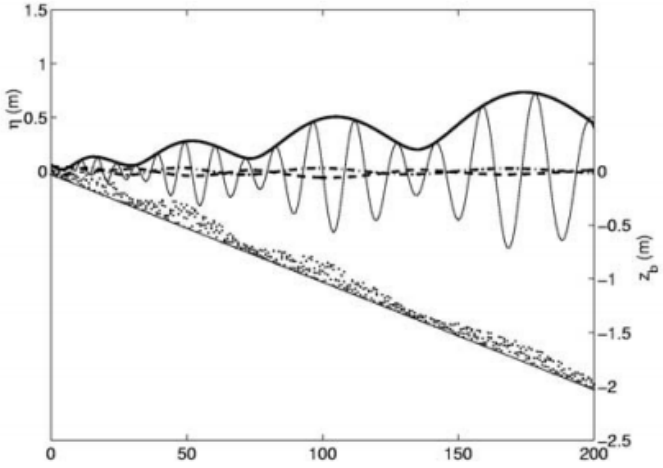

Figure 1: Water surface elevation as the result of short-wave groups (thin solid) creating bound IG waves (dotted) through radiation stress differences. Reflected free IG waves (dash-dotted). Figure by Reniers (2004).

When short waves break at the shoreline, the long waves are no longer bound to the wave groups, but free (Masselink, 1995). If the IG wave energy is not dissipated in the nearshore area, the free IG waves are reflected offshore. The seaward movement of the free IG waves and the interference with incoming low frequency waves, can result in a series of nodes and anti-nodes (standing waves). This can lead to IG wave heights up to 1 meter in the coastal zone (Suhayda, 1974, Huntley et al., 1977, Guza & Thornton, 1982).

If the incoming wave groups approach the shore at an oblique angle, the IG wave is reflected in a non-incident angle as well. When the free IG wave escapes seaward, it can be defined as a 'leaky' wave. If the reflected waves refract back towards the coast, the low frequency energy stays trapped in the coastal zone, propagating in the longshore direction in or just seaward of the surfzone. This leads to longshore variation in set-up at low-frequency periods, which is defined as an 'edge' wave (Figure 2) (Ursell, 1952, Gallagher, 1971). The trapped energy of the edge waves can be an important driver of swash oscillations (Bowen & Inman, 1971, Huntley et al., 1981, Guza & Thornton, 1985). Research of Reniers et al. (2006) also suggest that a coupling between edge waves and rhythmic bar morphologies can occur. In figure 3, velocity f-k_y-spectra are depicted. Reniers et al. (2006) suggested that the presence of longshore travelling IG edge waves where present as a result of interaction with a rip-charactirized morphology.

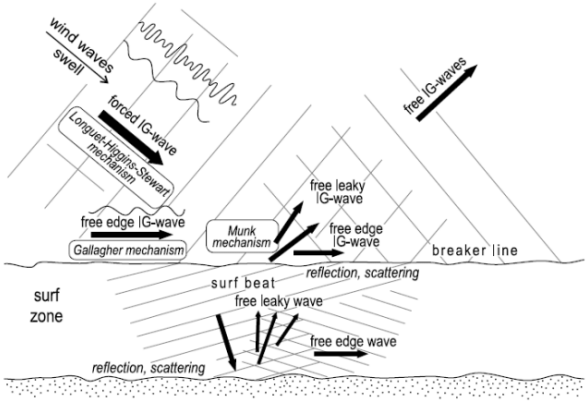

Figure 2: An overview of different incoming bound- and outgoing free IG wave types. Corresponding mechanisms are displayed in text boxes. Figure by Nielsen et al. (2015).

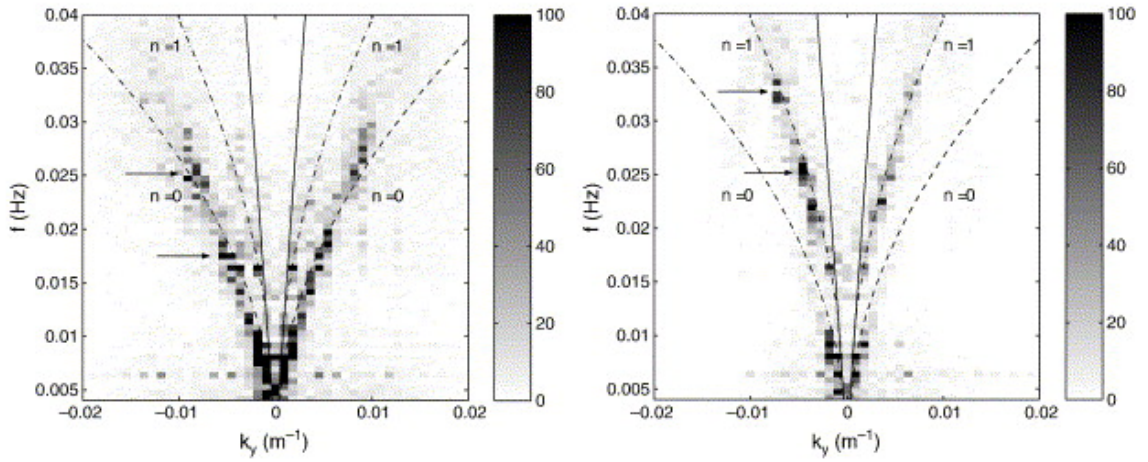

Figure 3: The left panel represents the velocity f-k_y-spectra near the shoreline, while the right panel is observed at the outer edge of the surfzone. Near the shoreline IG energy with a low longhore wavenumber (k_y) and a low frequency is observed, suggesting mode 0 (n = 0) edge waves, while at the edge of the surfzone higher frequencies of IG energy are observed suggesting mode 1 edge waves (n = 1). In the research of Reniers et al. (2006) an amplification of IG energy occurred at the scale of the rip channel spacings. Figure by Reniers et al. (2006).

Field, laboratory and numerical modelling studies suggest that not all the IG energy is reflected (B. G. Ruessink, 1998, Henderson et al., 2006, Thomson et al., 2006, Battjes, 2004, van Dongeren et al., 2007, de Bakker et al., 2014, de Bakker et al., 2015). In these studies, considerable loss of energy at IG frequencies can be observed near the shoreline.

The energy dissipation was first attributed to bottom friction (Henderson, 2002). This was discarded in later studies, as the bottom friction on sandy beaches is relatively low and therefore not able to result in the observed amount of IG energy loss (Henderson et al., 2006). Other studies suggested that energy loss was due to interactions between IG frequencies. On gentle sloping beaches, wave non-linearity occurred, which manifested itself in the development of a "borelike" shape of the IG wave. This suggests that breaking could act as a dominant mechanism for low frequency energy dissipation (Battjes et al. 2004, Van Dongeren et al. 2007, Lin and Hwung 2012, De Bakker et al. 2014).

2.1.2 Total water level

In the next sections, some basic concepts are reviewed. The concepts create a framework wherein the influence of IG waves on dune erosion can be studied. Sallenger (2000) based his storm impact theory on the total water level. The total water level can be dissected in three main elements, the tidal water level, the storm surge and run-up. The impact of tidal forces on the water level depends on the location and can be diurnal or semi-diurnal.

As dune erosion often occurs during storm conditions, the storm surge has a significant impact on the total water level as well. According to Harris (1963), a storm surge is defined as the difference between the water level during storm conditions and the water level in absence of the storm. Multiple hydrodynamic processes drive the generation of a storm surge. The most obvious process associated with a storm surge is the 'direct wind effect'. Winds can create a surface current, which transports water down-wind. The result can be a 'wind set-up', a rise in water level at down-wind locations. Other processes like the pressure effect, effect of waves, the rotation of the earth and the rainfall effect are described in more detail by Harris (1963).

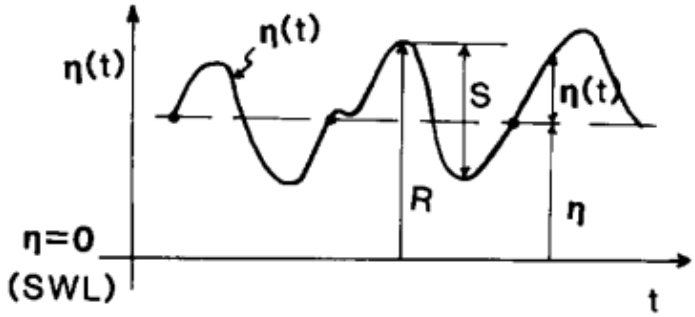

Figure 4: A schematic view of total run-up (R). $\eta = 0$ is the still water level measured offshore. S is the swash range between two zero crossings. Setup can be seen as the mean η. Figure by Holman (1986)

The final component of total water level is run-up. Run-up is best described as the local maximum elevation of the shoreline. Figure 4 illustrates the two main components that determine the elevation of the run-up (R); set-up (η) and swash (S). In short, the set-up can be defined as the time-averaged elevation of the shoreline, compared to the offshore still water level (SWL) (Holman, 1986, Stockdon et al., 2014). In a broad sense, it consists of all the changes in radiation stress, resulting in variation of the still water level

Focusing on nearshore area, the inner surf zone is characterized by a significant increase in set-up in the landward direction. Inside the surf zone the wave energy is dissipated as the result of breaking. This leads to a decline in radiation stress, driving the set-up. The maximum elevation of the shoreline will increase, causing it to migrate up and along the cross-shore profile.

The slope of the beach is an important factor in driving the potential set-up. If the slope is very steep, a relatively high reflectance of wave energy will be present. A high reflection of energy means less dissipation by breaking and therefore less set-up. In general, on low sloping beaches higher set-up levels are observed (Longuet-Higgins & Stewart, 1964).

Two main distinctions in forcing mechanism of swash oscillations can be identified (Baldock & Holmes, 1999, Elfrink & Baldock, 2002). The first driver of swash oscillations are high frequency waves approaching the coast. At a certain point the waves start breaking due to the decreasing water depth. In the final approach towards the shore, a turbulent bore arises. This turbulent wall of foam accelerates and decreases in height, eventually collapsing on the shore creating a thin layer of run-up and back-wash (Hibberd & Peregrine, 1979, Shen & Meyer, 1963).

Assuming saturated surf zone conditions, the elevation of these swash oscillations does not increase with wave height for waves with incident wave periods. If the wave height of incoming short waves increases, energy dissipation starts further offshore. By the time the waves reach the shoreline most of their energy is dissipated (Huntley et al., 1977, Guza & Thornton, 1982).

Swash oscillations are also driven by IG waves. The cross-shore standing wave pattern mentioned earlier, also drives the oscillation of the shoreline (Guza & Thornton, 1982). With increasing offshore wave heights, the amplitude of the standing wave patterns can potentially increase. This will lead to higher swash run-up compared to the breaking of high frequency waves.

To determine the role of low-frequency energy versus high-frequency energy in driving swash elevation on a specific site, the Irribaren number ξ_o is used as a parameter (Holman & Sallenger, 1985).

$$\xi_o = \frac{\beta}{(H_o/L_o)^2} \tag{2.1}$$

where β is the beach slope and H_0 and L_o are respectively deep water wave height and wavelength. If $\xi_0 < 1.75$, the swash oscillations are dominated by low-frequency energy (gradual beaches). At higher values of ξ_0 (relatively steep beaches), sea and swell waves are increasingly dominant in driving swash oscillations. In the case of Egmond aan Zee the beach has a relatively low slope, resulting in low ξ values. Swash is therefore mostly dominated by low-frequency energy (Elfrink et al., 2006).

2.2 Dune erosion

2.2.1 Impact regimes

During storms, erosion of coastal dunes is a frequently occurring phenomenon, increasing the risk of flooding. Sallenger (2000) divided the impact of storm conditions on the geomorphological features of barrier islands in the United States into four different regimes.
The impact is based on the landward vertical margins of the total water level (Section 2.1.2), relative to the dune crest and base. R_{low} and R_{high} are respectively the low and high elevations of run-up (Figure 5). As depicted in figure 6, the dune base is referred to as D_{low} and the dune crest as D_{high}.
Based on these definitions the first regime is defined as the 'swash regime'. During the swash regime, erosion is confined to the beach foreshore. No contact with the base of the dune is occurring, resulting in the following threshold:

$$R_{high}/D_{high} < D_{low}/D_{high} \tag{2.2}$$

The 'collision regime' starts when the wave run-up elevation surpasses the base of the dune. The upper limit of the collision regime threshold is the situation in which waves overtop the dune crest. In the 'collision regime' dune erosion starts to occur (Sallenger, 2000). This condition can be defined as:

$$R_{high}/D_{high} < 1. \tag{2.3}$$

When the relevant high elevation of swash starts to overtop the dune crest, the storm impact enters the 'overwash regime'. Barrier islands on the United States East Coast can easily be over washed as a result of typical winter storms. The 'inundation regime' indicates that a beach is entirely subaqueous. Extreme conditions are necessary for the 'inundation regime' to occur (Sallenger, 2000). The definitions for respectively the 'overwash regime' and the 'inundation regime' are given below:

$$R_{high}/D_{high} > 1 \text{ and } R_{low}/D_{high} < 1 \tag{2.4}$$
$$R_{high}/D_{high} > 1 \text{ and } R_{low}/D_{high} > 1 \tag{2.5}$$

The storm impact scale is frequently referred to in dune erosion research (e.g., Roelvink et al., 2009, McCall et al., 2010, Armaroli et al., 2013, Lindemer et al., 2010, Palmsten & Splinter, 2016). The classification of the storm regimes gives information about the driving mechanisms of morphological change. Most of the winter storms in the Netherlands relate only to the swash regime and collision regime (de Winter et al., 2015, Aagaard et al., 2005, Ruessink et al., 2019). Therefore, the erosional mechanisms in the swash and collision regime will be evaluated in more detail.

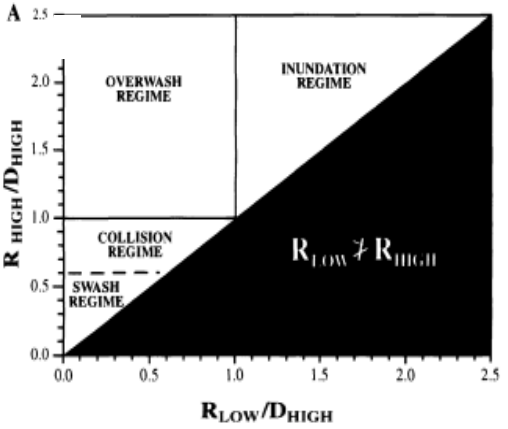

Figure 5: Thresholds for different impact regimes. Based on the ratio of vertical swash excursion and dune crest height (Sallenger, 2000).

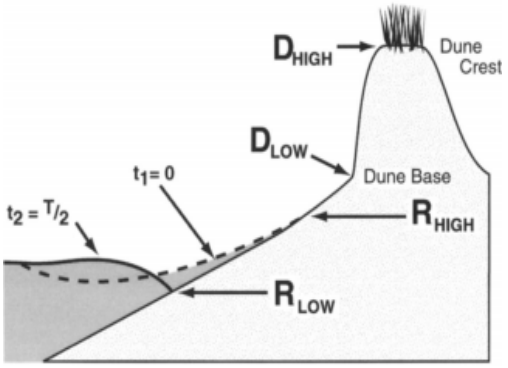

Figure 6: Schematic display of a beach according to Sallenger's (2000) storm impact scale With R representing the run-up. D_{low} and D_{high} respectively the dune foot and dune crest.

A persistent storm surge can, over time, flood the beach. At a certain point, run-up starts colliding with the dune foot. The impact of the storm moves into the collision regime. The waves start to undercut or remove sediment at the dune foot. When the water level increases even further, not only run-up acts as an erosional forcing, but short waves directly collide against the dune face as well.
With these higher storm surge levels, the breaking point of the short waves shifts landward. Hence, more wave energy reaches the dune, resulting in an increased wave force impact and therefore larger volumes of eroded sediment. Field and wave tank observations confirm this positive correlation between storm surge and erosional volume (Vellinga, 1982, van Gent et al., 2008).

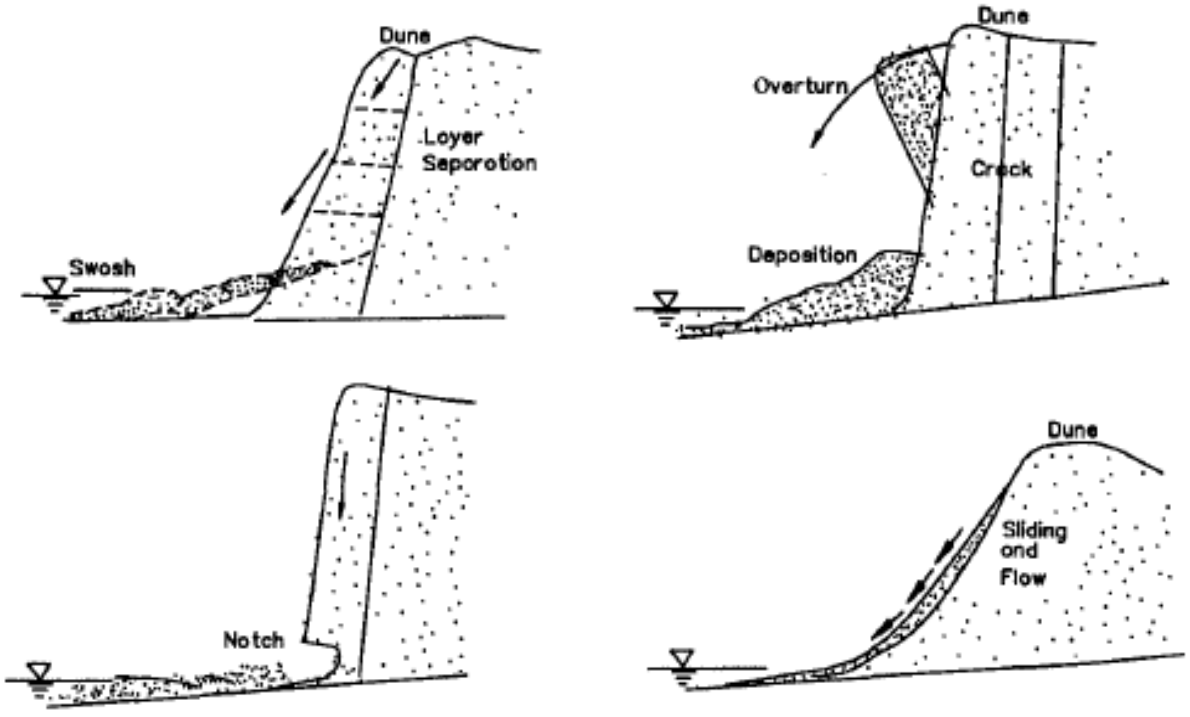

.

Figure 7: Conceptual images on erosional mechanisms. On the top left, layer separation and collapse due to wave impact is depicted. On the top right the separated layer overturns and collapses. On the bottom left, a notch is created by wave action, resulting in a slump of the overhang layer. The right-hand bottom image depicts the sliding and flowing on gentle slope dune faces. Figure by Nishi and Kraus (1996).

Nishi and Kraus (1996) distinguished three types of dune erosion in the collision regime, depending on dune slope and compaction of the sediment. When waves impact a nearly vertical dune face, a vertical fault separates the outer layer from the dune. This outer sediment layer detaches and will collapse or even overturn. This process is referred to as layer separation (Figure 7). When a dune face is nearly vertical and the sediment is well consolidated, the waves cut a notch in the base of the dune. This continues until the overhanging layer separates and collapses. This erosional sequence is defined as 'notching and slumping'.

Finally, if the dune sediment is hardly compacted and a gentle slope is present, thin layers of sediment slide down the dune front as the result of wave impact at the dune base. This 'sliding and flowing' mechanism can steepen the dune face over time, causing conditions for layer separation or notching and slumping (Figure 7) (Nishi & Kraus, 1996).

The described erosional mechanisms result in deposition of sediment lumps from the old dune face at the base of the new dune face, temporarily obstructing further wave impacts on the base of the new dune front. The lumps are eventually transported seawards, making way for the next erosional sequence (Erikson et al., 2007, van Gent et al., 2008). In XBeach, the erosional mechanisms in the collision regime are solved by a set of avalanching equations (Eq. 8.44 & 8.45), which use a parameterized critical slope.

If the slope is steeper than the critical slope, avalanching occurs. The critical slope is less steep for situations where sand wet, due to the assumption that saturated sand moves faster than dry sand (Roelvink et al. 2019).
Over time, this results in a landward migration of the dune front. This process will continue until the storm event stops or an equilibrium state is accomplished. Under milder, post-storm conditions the dunes start developing again (Arens, 1996).

During these erosional sequences swash and inner-surf processes are the main drivers for seaward sediment transport. Rip currents potentially act as a driver of offshore sediment transport in conditions where bathymetry is non-uniform in the longshore direction.
If the bathymetry is relatively uniform, breaking of waves can also result in a net seaward directed current ('undertow'). The magnitude of this undertow is related to the intensity of the breaking waves. As the breaking of waves becomes less intense in seaward direction, the velocity of the undertow decreases, and the current will eventually not be strong enough to transport the sand (Vellinga, 1982). Consequently, the sand settles, resulting in the accretion of the foreshore (Figure 8).
Whilst moving across this new beach profile, the breaking point of the waves shifts seaward, due to a decrease in water depth in seaward direction. The seaward migration of the breaking point leads to the reduction in wave force impact on the dune base, reducing the erosional volume. Continuous erosion of the dune and accretion of the shoreface will eventually lead to a decrease in dune erosion rate until an equilibrium situation reached (van Gent et al., 2008).

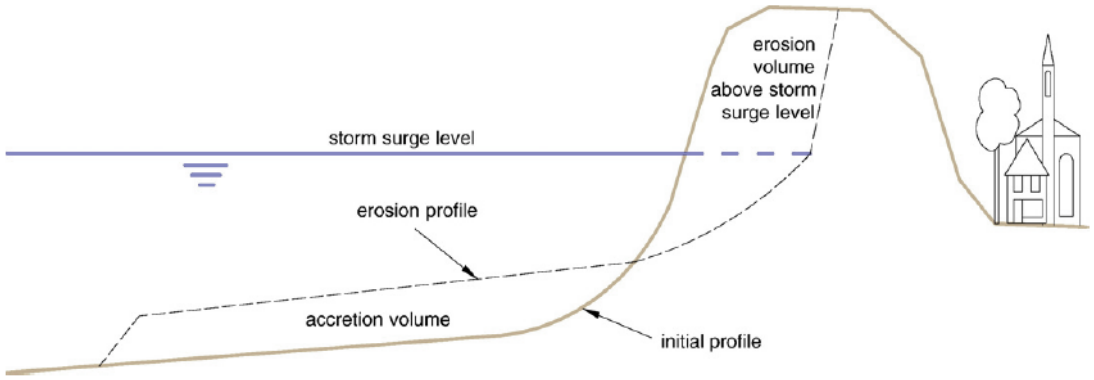

Figure 8: Pre- and post-storm profiles indicating the erosion of the dune caused by the storm surge and the accretion of the foreshore due to sediment deposition. Figure by van Gent et al. (2008).

2.2.3 Longshore variation

Studies on erosional mechanisms as described above, often assume a longshore uniform morphology (Vellinga, 1982, van Gent et al., 2008). In nature, this assumption is rarely met. Field observations suggest that storm conditions can lead to a longshore variation in dune erosion as a result of bathymetry or subaerial characteristics of the nearshore area. Thornton et al. (2007) and Castelle et al. (2015) both observed erosional hotspots at locations where megacusp embayments were present. For Thornton et al. (2007) the focus was on inner bar morphology, while Castelle et al. (2015) found similar results due to an outer bar coupling resulting in longshore variation in total water levels. At the location of the embayment the beach was relatively narrow (Figure 9: yellow arrows). During storm conditions swash reaches the dune foot at these locations. Erosion led to a landwards recession of the dune front. The eroded sediment was transported seaward by the rip current present in the embayment (Thornton et al., 2007).

Longshore currents can dampen this effect by fulfilling the sediment demand of the rip currents. Over time, the sediment transported by the longshore current increases the uniformity of the beach, resulting in a lower variability in longshore dune erosion (van Thiel De Vries et al., 2011). Van Thiel De Vries et al. (2011) state that the longshore variation in dune erosion predicted by XBeach is dominantly driven by gradients in the longshore component of sediment transport.

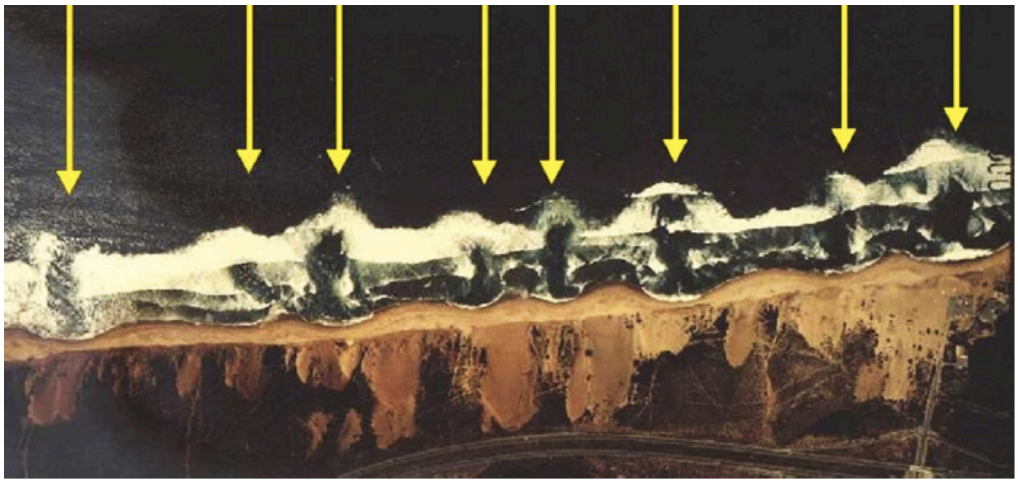

Figure 9: The yellow arrows indicate rip currents. In the rip current the waves do not break resulting in dark water. The locations of the rip currents coincide roughly with the embayment of megacusps and "hotspots" of erosion in the dune row. Figure by Thornton et al. (2007)

Other research suggests that in the absence of megacusps, longshore variability of bar patterns is not the main driver of dune erosion patterns (de Winter et al., 2015). De Winter et al. (2015) use numerical modelling to demonstrate that pre-storm dune topography is responsible for variation in erosional volume. Although bar patterns are hardly as distinct as the megacusps of Thornton et al. (2007) and Castelle et al. (2015), longshore variability in bathymetry was present. The bathymetry and intertidal area played a secondary role as driver of dune erosion variability in the initial stage of the storm. As the storm surge increases over the duration of the storm, the impact of the bathymetry decreased. The research of Splinter et al. (2018) confirms these findings. Using video data, the development of small rip channels was observed just after the peak of the storm. Analysing the location of the erosional hotpots, the rip channels cannot be interpreted as the main driver. A more dominant driver of variation in erosional volume is probably the dune toe topography. Locations with a lower dune toe are more likely to erode as a result of a rising total water level during storms. Also, areas with a steeper dune front are more prone to slumping and therefore erosion (de Winter et al., 2015).
Consequently, it can be stated that in the absence of distinct subtidal structures, longshore variation in dune erosion can be attributed to the amount of sediment available around the total water level.

2.3 Modelling dune erosion with XBeach

As field observations of hydrodynamic conditions or morphological changes are often hard to acquire and/or not abundantly present, numerical models proved to be important tools for understanding the processes that govern dune erosion. Numerical models focus on the prediction of morphological behaviour using a digital environment. In this environment, the boundary conditions for hydrodynamics and coastal morphology can be selected and systematically controlled. Subsequently, the model predicts the changes caused by these boundary conditions. As a result, a new morphology is created for the subtidal area and/or the beach of which the driving processes can be dissected.

Within the prediction of dune erosion, two different approaches in numerical modelling are observed (Larson et al., 2004). The equilibrium profile approach is based on the theory that a beach is in equilibrium with the hydrodynamic conditions. The eroded sediment volume from the dunes and upper beach is deposited on the foreshore (Figure 8). This creates a stable new beach profile. These models are usually more based on empirical data of beach evolution and less on physical processes (Kriebel & Dean, 1985).

In the other approach, dune erosion is estimated based on wave impact. Here, both nearshore hydrodynamic processes and empirical data are used to define a relationship between the impact of waves on dunes and the magnitude of erosion. These models are often local and assess on a single profile line scale (Overton et al., 1995, Nishi & Kraus, 1997).
Both approaches often assume a uniform recession of the dune front in the long-shore direction. This is based on general field observations after storm events (Nishi & Kraus, 1997).

The limitations in the long-shore dimension led to the development of XBeach, an open-source nearshore numerical model to evaluate storm impact on beach profiles (Roelvink et al., 2009). In XBeach the complex response of beach and dune profile to storm conditions is calculated based on physical processes. The horizontal, two-dimensional character of XBeach also makes it possible to study morphological behaviour considering longshore variable bathymetry and/or wave conditions (Roelvink et al., 2009).

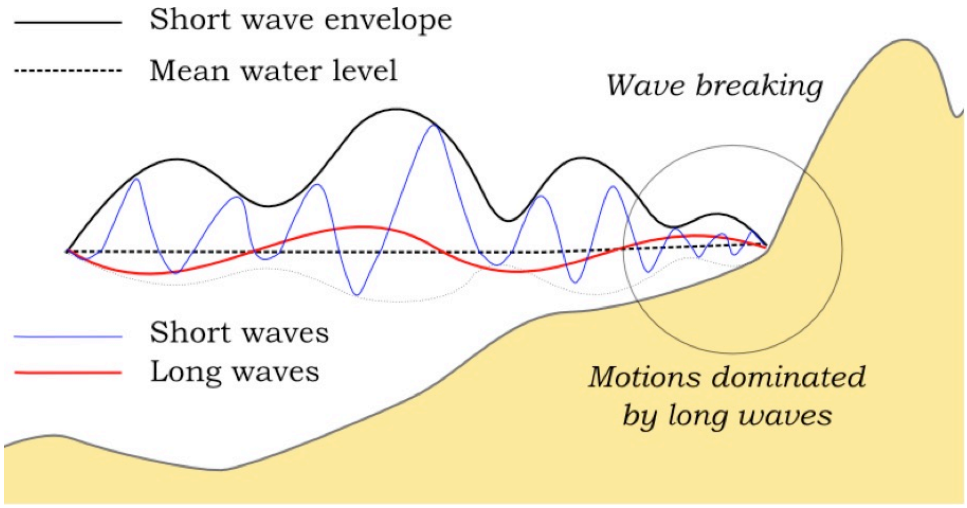

Figure 10: The solid black represents an envelope of the short-wave height variation. Based on the envelopes infra gravity waves can be calculated. High frequency waves dissipate towards the beach. The result is a domination of swash motions by low frequency waves. Figure by Hoonhout (2015).

2.3.1 XBeach modi

The original XBeach model was developed to resolve short-wave variations on group scale with the purpose of modelling the morphology of dissipative beaches. In this 'surfbeat' setting, the short waves are enveloped on a group scale (Figure 10) and parameters are averaged over depth, leading to a 2DH model. No individual short waves have to be resolved, which greatly reduces required computation time (Roelvink et al., 2009). A detailed description of the equations governing physical processes of the surfbeat-mode are present in appendix 8A.
A non-hydrostatic and a stationary mode were added later. The non-hydrostatic mode resolves the non-linear evolution of incoming wave fields on the timescale of individual waves, providing a more accurate simulation of the wave-current interaction. However, to simulate these detailed processes, a higher spatial resolution and smaller time steps are necessary, increasing the load on computational resources (Smit et al., 2010, Roelvink et al., 2018). The stationary mode neglects the wave group variations. This means that IG waves are not present in simulations. The stationary mode is therefore only useful under conditions where IG waves are hardly present due to small incident waves (Roelvink et al., 2018).

In figure 11 a flow diagram is presented in which the main components of the computational sequences of surfbeat are displayed, starting with the short-wave action balance, in which the wave action density over time and space is calculated. Then, a roller element is introduced. This accounts for the wall of foam, occurring when a wave breaks.
From these balance equations the interaction with the current velocities can be determined. The current velocity determines where stirred-up sediment is transported to. Based on the sediment transport, it is determined whether erosion or deposition takes place. In the final step the bed-level has to be updated. The new morphological conditions influence the wave energy closing the loop (Roelvink et al., 2009). In appendix A mathematical basis for the above-described loop will be evaluated in detail.

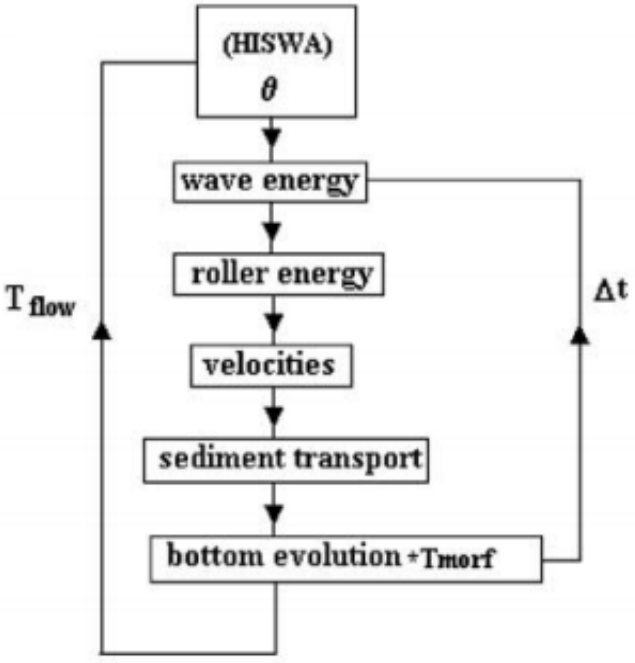

Figure 11: A flow diagram describing the computational steps of an XBeach morphological simulation. Figure by Reniers (2004).

Although, in general, the morphological simulations of dissipative beaches using the surfbeat mode are accurate, some adjustments to the model had to be made. Stockdon et al. (2014) dissected the run-up component of the total water level predictions of XBeach. In an analysis on the components of run-up (Section 2.1.2), a significant underprediction of incident-band swash heights was observed. This is the result of averaging the short waves in the surfbeat modus. The contribution of the IG waves to the run-up was underestimated as well. XBeach did, however, accurately predict the set-up but overestimated the mean water level (Palmsten & Splinter, 2016).

In 2018, XBeach was modified in order to fix these errors. In solving this problem, the focus was on correctly predicting the variability in short-wave height. This variation is responsible for creating the IG waves (Longuet-Higgins & Stewart, 1962) and can be expressed in the Groupiness Factor (Funke & Mansard, 1980):

$$GF = \frac{\sigma_{H^2}}{\overline{H^2}} \tag{2.6}$$

Where $\overline{H^2}$ represents the mean slowly varying wave height and σ the standard deviation of H^2. With increasing GF values, the groupiness increases resulting in an increase in IG energy. Research showed that the trends in groupiness, and therefore IG waves, are related to the grid size of the modelled coastal area and the directional spreading s. The groupiness grew in case of relatively smaller grid sizes, while the groupiness was dampened with larger grid sizes (Roelvink et al., 2018). The corrections based on Warming & Beam (1976) resulted in a negative relative GF for every grid size (Figure 12). This means that for every grid size, the groupiness dissipates towards the coast.

The second adjustment made was adding a ‘single-dir’ option next to the default ‘multi-dir’ setting. The wave energy in the initial ‘multi-dir’ framework is calculated in a three-dimensional space (x, y, θ). The ‘single-dir’ approach brings the wave-action equation (Eq. 8.1) and the roller balance equation (8.22) back to a two-dimensional problem. This is illustrated in equation 2.7 and 2.8. Mean wave directions $(\bar{\theta})$ are calculated, along which the short-wave energy propagates. The resulting wave action balance is as follows:

$$\frac{\partial A}{\partial t} + \frac{\partial C_g \cos\bar{\theta}\, A}{\partial x} + \frac{\partial C_g \cos\bar{\theta}\, A}{\partial y} = -\frac{D_w + D_f + D_c}{\sigma} \tag{2.7}$$

$$\frac{\partial S_r}{\partial t} + \frac{\partial c \cos\theta\, S_r}{\partial x} + \frac{\partial c \cos\theta\, S_r}{\partial y} = -D_r + D_w \tag{2.8}$$

The effect is less smoothening of wave groupiness in the longshore direction as can be seen in figure 11. Roelvink et al (2018) concluded that the implemented ‘single-dir’ option increased the accuracy of modelling high- and low-frequency wave height, long-shore currents and low-frequency spectra. As a result, the error in predicting the run-up decreased, compared to the initial surf-beat modus.

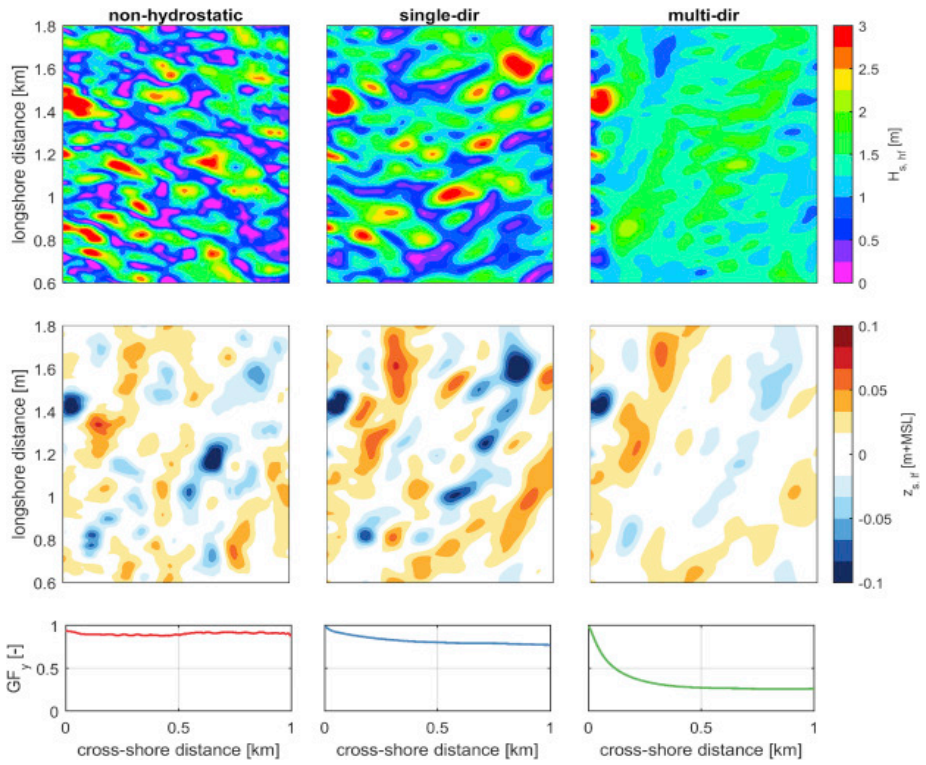

Figure 12: Top panels: the short-wave varying height for the non-hydrostatic mode (left column), the single-dir (middle column) and the multi-dir option (right column). Middle row: the sea surface elevation as a result of infragravity waves. Bottom panels: groupiness factor averaged in the long-shore direction. Directional spreading coefficient s=10. Figure by Roelvink et al.. 2018.

2.3.2 XBeach research

Since the development in 2009, a lot of research on dune erosion has been done using XBeach. To validate the model, the sensitivity of XBeach to variation in parameters and boundary conditions has to be tested. The first hindcasting of storm conditions was done on eight different sites throughout Europe. In general, the results show that XBeach overpredicted the erosion around the mean water line. The deposition of the sediment at the lower beach face was therefore also overpredicted. Regardless of this overprediction, XBeach showed good efficacy in predicting coastal response under storm conditions (Van Dongeren et al., 2009).
McCall et al. (2010) presented results on a simulation of hurricane Ivan and concluded that XBeach is sensitive for variation in sediment stirring parameter (Eq. 8.40). If no limitation on sediment transport was imposed, morphological change of the barrier island was predicted an order of magnitude larger than measured (McCall et al., 2010).
Small changes in hydraulic boundary conditions did not lead to significant morphological changes. This is also confirmed in an XBeach simulation of hurricane Katrina (Lindemer et al., 2010).

Splinter & Palmsten (2012) also studied the parameterization sensitivity, concluding that XBeach is not overly sensitive to changes in bathymetry. This is important because pre-storm bathymetry data, close to the actual storm event are rare. Significant over-estimation of upper beach erosion was observed. Splinter & Palmsten (2012) hypothesise that, in XBeach, dune erosion is dependent on an accurate prediction of the total water level (Section 2.1.1). If the total water level is overpredicted, the eroded sediment volume is over predicted as well. The model also proved to be sensitive to changes in the parameterization of the wave dissipation and wave skewness. The choice in wave dissipation modes can lead to large differences in error of estimated eroded volume (Splinter & Palmsten, 2012).

The influence of wave skewness (γ_{ua}) is mainly expressed in the direction of sediment transport. If γ_{ua} = 0 the transport of sediment is away from the nearshore. With γ_{ua} = 1 all sediment is transported onshore. The value for γ_{ua} can be calibrated and lies between 0 and 1 (Splinter & Palmsten, 2012). The sensitivity of dune erosion in the collision regime to wave skewness was also observed in a simulation of hurricane Sandy (De Vet et al., 2015). It can be concluded that the calibration of free parameters is important for the prediction on specific locations and under certain storm conditions (Callaghan et al., 2013).

De Winter et al. (2015) used XBeach to study dune erosion at Egmond aan Zee. Their results of a simulation of a 2012 winter storm, led to more detailed dune morphology related observations. XBeach overpredicted sediment erosion volume in an area where dune scarping was present and under predicted the erosion volume where slumping occurred. This could be due to the simplicity of the dune erosion calculation, which is based on the avalanching mechanism (Eq. 8.44 & 98.45). The stabilizing result of vegetation at the dune front is not present in erosion calculations. Armaroli et al. (2013) also observed this phenomenon and therefore suggest a more process-based dune erosion mechanism.

2.3.3 Research questions

In order to build bridges between field observations and XBeach results a thorough understanding of the processes responsible for the longshore variation in dune erosion in XBeach is necessary. In addition, with a new XBeach surfbeat mode available (Roelvink et al., 2018) changing the hydrodynamic environment of the model, new questions arise. With an Egmond aan Zee-inspired beach and the presence of a longshore varying outer bar, variation in dune erosion can be subjected to different hydrodynamic conditions. This leads to the following question describing the main focus of this research:

Main question:

Which processes drive longshore variability in dune erosion in numerical modelling using XBeach multi-dir and single-dir settings over crescentic sandbars?

To answer this question both single-dir and multi-dir method are used parallel to each other. First the impact of wave angle and wave height on the hydrodynamic conditions in the nearshore area is evaluated. Subsequently, the varying conditions and their impact on the longshore variability in dune erosion are researched. The correlation between the hydrodynamic conditions and the dune erosion can be reviewed and eventually, a comparison between both methods could increase the available knowledge of the processes driving longshore variation in dune erosion. The following set of sub questions define the steps necessary to attain the main goal of this research:

Sub questions:

What is the impact of different wave angles and wave heights over a longshore variable bathymetry on nearshore hydrodynamic processes?

What is the impact of different wave angles and wave height over a longshore variable bathymetry on dune erosion?

Are there correlations between the longshore variation in dune erosion and the hydrodynamic processes?

What are the differences in longshore variation in dune erosion and hydrodynamic conditions between the single-dir and multi-dir method?

3. Methodology

3.1 Model set-up

3.1.1 Study site

XBeach uses a grid-based application of the spatial dimensions in the coastal zone, in order to study the morphological behaviour. Every grid cell is linked to an x-coordinate in the cross-shore dimension and an y-coordinate in the longshore dimension. Depending on the type of parameter, the values correspond to the cell centres (bed level and water levels) or the cell interfaces (velocities and sediment transports).

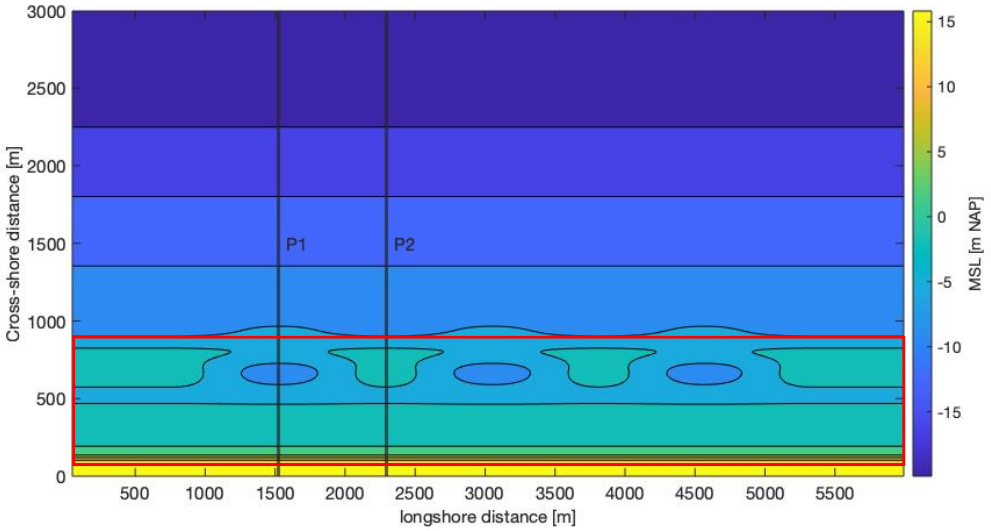

Figure 13: Full bathymetry dimensions. Lines P1 and P2 are represented by cross-shore profiles in figure 14. P1 is a cross-section of the beach at the location of a bay, while P2 covers the cross-shore dimension on a location with a horn. The area within the red box is used to evaluate the results in more detail.

In figure 13 the input bathymetry of the model is plotted. The bathymetry is based on the research of Neele (2019). The supratidal profile is of the JARKUS 2011 LiDAR dataset[1]. The beach and dune are longshore uniform in order to remove topography driven variation in dune erosion. In the subtidal area a two-bar system is present. The inner bar has a longshore uniform shape, while the outer bar has multiple large morphological features. The distance between two bays in the outer bar for a representative case at Egmond aan Zee is 1500 meters. The outer bar present in the bathymetry of Neele (2019) consisted of a single horn and two adjacent bays. A second horn and third bay are added to this bathymetry, to ensure that any emerging longshore variation in dune erosion would be visible. In this way, longshore morphological patterns can be linked to the responsible processes.
In figure 14 the two cross-shore profiles on location P1 and P2 are illustrated. The cross-sections profiles are different between 1000 and 500 metres cross-shore distance. The horn has a steeper seaward front, while the seaward slope of the outer bar at the location of the bay is less steep. The bay itself is under still water conditions roughly 7.3 meters deep, while the horn is about 0.8 meters below NAP. The size of the grid cells varies in both the longshore and cross-shore dimension. The cross-shore variation of grid size is relatively low and differs from 13 meters at the seaward boundary to 8 meters in the surf zone. A large part of longshore dimension consists of a grid size of 10 metres. At the boundaries the grid size increases to 50 meters.

[1] https://publicwiki.deltares.nl/display/OET/Dataset+documentation+JarKus

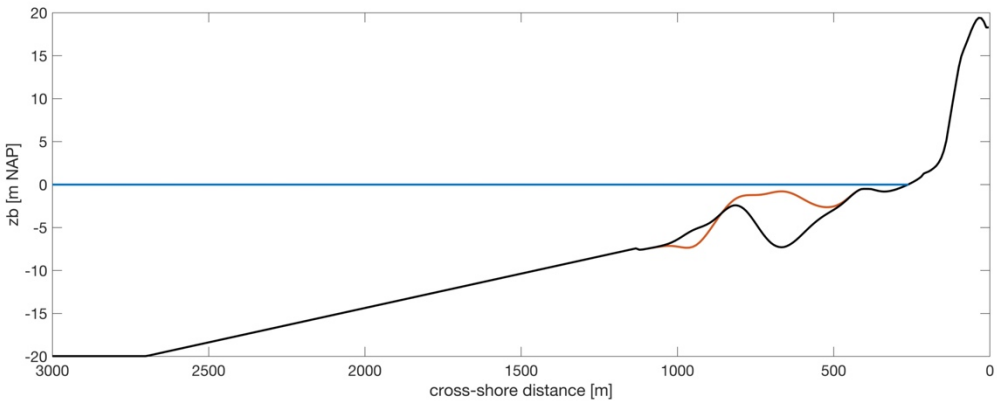

Figure 14: Cross-section of the coastal profile. The black line is the profile at location P1 (Figure 13). The orange line represents section P2. The blue line is the water level at still water conditions.

3.1.2 XBeach settings

XBeach offers a wide variety of adjustable settings in order to calibrate the simulations for the specific research goals. Because IG waves are an important driver of swash oscillations and therefore dune erosion, this research uses the surfbeat mode. This leads to a reduction in computation time that can be used for modelling larger longshore dimensions. In table 1, the most significant settings are listed. For settings not mentioned below, default values have been applied.
The surfbeat simulations in this research all have cyclic boundary conditions (*cyclic = 1*). This indicates that the lateral boundaries of the study area are modelled as if they are connected. Waves, currents and sediment leaving the study area at one lateral boundary, enter the study area at the other lateral boundary, preventing the occurrence of shadow zones. In order to focus on hydrodynamic conditions, sediment transport is excluded in some phases. Therefore, the parameter 'sedtrans' was set to either zero or one.
The method used for short-wave dissipation by breaking (*break*) is 'roelvink2'. This refers to equation 9.13, where short-wave dissipation is proportional to the ratio of significant wave height and water depth. Two free parameters that proved to be of significant importance to the calibration of XBeach, are 'gamma' and 'n' (e.g., Splinter et al., (2011), Splinter and Palmsten, (2012), Callaghan et al., (2013)). 'gamma' (γ) is the breaker index in equation 9.16 and n refers to the power in wave probability equation 9.14. For both, default values where used based on the research of de Winter et al. (2015), in which beach and storm state are similar to this research.

Name	Value
cyclic	1
sedtrans	1 (SN)
	0 (SF)
wavemodel	surfbeat
morfac	2
morstat	1800 (s)
zs0	4 (m)
dryslp	1
wetslp	0.3
break	roelvink2
gamma	0.55 [-]
n	10
wbctype	jonstable

Table 1: General settings used in the simulations. The dry and wet slope are only relevant when sediment transport is on. In this case 'morfstat' is the time at which the morphology starts to change.

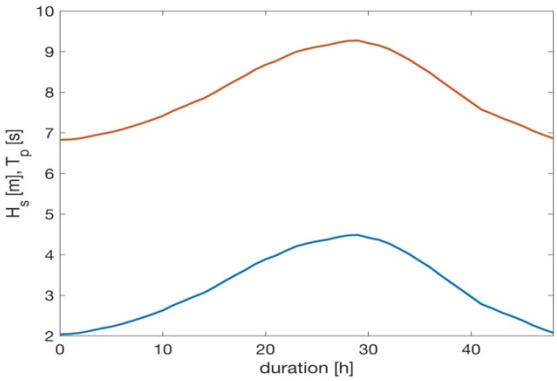

Figure 15: Wave conditions during storm of 5-7 December 2013. The blue line represents the significant short high frequency wave height (H_s). The red line indicates the peak period (T_p) during the storm.

3.1.3 Hydrodynamic boundary conditions

Hydrodynamic boundary conditions are determined based on storm conditions at Egmond aan Zee. A constant storm surge is set of 4 metres (zs0). This is relatively high and places the simulation directly in the collision regime. This excludes the storm surge as a variable and the direct impact on the dune front of other hydrodynamic conditions can be determined.
Wave conditions were either defined as 'constant' or 'variable'. This refers to values of significant wave height (H_s) and the peak period (T_p) in the high frequency waveband. The constant H_s and T_p are based on historic data of eight storms that occurred in the period 2013-2020. H_s and T_p are measured using a wave buoy at location 'Ijmuiden Munitiestortplaats', southwest of Egmond aan Zee. The storms descriptions and the quantitative data are both provided by Rijkswaterstaat[23]. The constant H_s is calculated as the overall mean short-wave height of the storms and has a value of 3.29 meters (Table 3). T_p is computed based on the following equation:

$$T_p = T_{m02} * 1.33 \quad (3.1)$$

In constant wave conditions T_p is 8.2 seconds (Table 3). In simulations where H_s and T_p varied over time, smoothed storm data from the period 5-7 December 2013, also known as the "Sinterklaas storm", was used (Figure 14). Boths simulations with constant hydrodynamic conditions and time-varying hydrodynamic conditions have the same duration.
Table 2 is an example of a single row of values for JONSWAP parameters. H_s and T_p are filled in respectively, in column one and two. 'mainang' represents the angle of the incoming waves, values used in this research are substantiated in section 4.1.3. 'gammajsp' is the peak enhancement factor as presented by Hasselman et al. (1973), 's' is the directional spreading coefficient. The value for s determines the spreading of wave energy in different directions. Default values for s and gammajsp are used throughout this research. The 'duration' of a specific JONSWAP wave spectrum was 3600 seconds (one hour), where the sum of the column 'duration' was equal to length of the simulated storm.

H_s (m)	T_p (s)	mainang (°)	gammajsp	s	duration (s)
3.29	8.2	0	3.3	10	3600

Table 2: Example of table with parameters for JONSWAP spectrum. 'mainang' is here specified using Cartesian coordinates.

Start date	$\overline{H_s}$ (m)	$\overline{T_p}$ (s)
05-12-2013	3.49	8.63
21-10-2014	3.22	8.01
09-01-2015	3.36	7.90
13-01-2017	3.11	8.22
29-10-2017	2.89	8.40
03-01-2018	2.91	7.41
08-01-2019	3.53	8.81
09-02-2020	3.78	8.15
Total mean	3.29	8.2

Table 3: Data from eight different storms form the period 2013- 2020. The starting dates of the storms are displayed in the leftmost column. The $\overline{H_s}$ and $\overline{T_p}$ of each individual storm are indicated as well as the mean values over the whole dataset. The data is provided by Rijkswatersaat[23].

[2] https://waterberichtgeving.rws.nl/water-en-weer/verwachtingen-water/water-en-weerverwachtingen-waternoordzee/stormvloedrapportages/stormvloedverslagen
[3] https://waterinfo.rws.nl/#!/nav/index/

The directions from which the waves originate, or the wave angle, are specified in table 1 using Cartesian coordinates. This means that a 0° wave angle coincides with the x-axis of the bathymetry, which is perpendicular to the coastline. The wave angle increases in the clockwise direction. Meaning waves propagating from right to left (Figure 12) have an incoming wave angle of 90° and waves propagating from the left have an angle of -90°.
To determine the impact of variations in wave angle different wave angle set-ups are present in this research. A reference run of a constant 0° is the starting point of the research. This is followed by simulations with a time-constant wave angle. For each of these phases the wave angle varies from -45° to 45° degrees with an interval of 5°. These results can be compared to the 0° phases and can be used as reference to simulations where the wave angles shift over time.
In some phases (table 4), a time-varying wave angle implemented, with a constant change in wave angle over time. The arrows in table 4 (→) indicate in which direction the waves angle is rotating during the simulation. The direction of incoming waves moves from -45° to 45°. This is a simplification of the wave angle behaviour during the December 2013 storm. In the simulation, the change in θ over time is constant, while during the real-life storm, variation in the gradient of θ was observed. A constant θ-gradient excludes variation in the θ-gradient as a driver for characteristics of the physical processes in the nearshore area.

3.2 Approach

In table 4 a schematic view of the simulations necessary for the research is presented. Each phase has its own code based on the applied boundary conditions. The research starts with runs where sediment transport is excluded from the physical processes in order to gather information about the distribution of IG wave energy and short-wave energy in the longshore dimension and the resulting currents. These phases are indicated by the presence of 'SF' in their phase-name.
Every set of wave characteristics is simulated in a run with the multi-dir method (M) and a phase with the single-dir method (S) (Section 2.3.1 & 9.1). For both methods, variations in wave angle are simulated. Reference simulations are run under a 0º wave angle, indicated by 'a'. The observations of the reference run can be compared to every 5º interval of the time-constant wave angles (b) and eventually to a time-varying wave angle (c) explained in section 3.1.3.
In phases indicated with a 'C' the wave height and wave period are constant over time, otherwise the wave height and wave period are time-varying (Figure 14) and indicated by a 'V'.
For the simulations where sediment transport is added to the active physical processes (SN), a slightly different approach is taken. A boundary conditions for the wave angle is added, where the wave angle is a constant 45º during the whole duration of the storm (48 hours). This is indicated by a 'd' and acts as an extra step in understanding the difference in physical processes due to variations in wave angle.
This leads to a set of 20 phases, each with its own code name. For example, for the phase 'SFScC' the sediment transport is excluded in the physical processes (SF), the single-dir method is used (S), the wave angle is time-varying from -45º to 45º and the significant wave height and peak period are constant (C).

Sediment transport	-dir	Wave angle (θ)		Wave height and period	Phase-name
Off (SF)	Multi (M)	0	(a)	Constant (C)	SFMaC
		45, -40…40, 45.	(b)		SFMbC
		-45 → 45	(c)		SFMcC
		0		Variable (V)	SFMaV
		-45 → 45			SFMcV
	Single (S)	0		Constant	SFSaC
		45, -40…40, 45.			SFSbC
		-45 → 45			SFScC
		0		Variable	SFSaV
		-45 → 45			SFScV
On (SN)	Multi	0		Constant	SNMaC
		45, -40…40, 45			SNMbC
		-45 → 45			SNMcC
		45	(d)		SNMdC
		0		Variable	SNMaV
		-45 → 45			SNMcV
	Single	0		Constant	SNSaC
		45, -40…40, 45			SNSbC
		-45 → 45			SNScC
		45			SNSdC
		0		Variable	SNSaV
		-45 → 45			SNScV

Table 4: Schematic overview of all the simulations. The type of propagation of directional-spread waves(-dir) is indicated for every phase. The wave height and peak period conditions are indicated as either constant, with a value of respectively 3.29 metres and 8.2 seconds, or variable (Figure 15).

3.3 Evaluation of results

In order to determine the impact of the bathymetry on the longshore variation of dune erosion, First the hydrodynamic processes in the nearshore area will be evaluated. For every set of conditions, a general overview of the mean high- and low frequency energy distribution and the mean currents is given. As IG waves can play a large role in the run-up, they are evaluated in more detail at the dune foot (Figure 13, y = 0 to y = 150). If the differences in a comparison of the IG height at the dune foot are too large, results will be normalized by subtracting the mean of the specific dataset. The mean short-wave height, set-up, longshore current and mean current are evaluated over the cross-shore profiles of both the embayments as the horns. These four components are also dissected averaged over the beach (144 to 176 metres cross-shore distance) in the longshore dimension. Some of the relevant figures are moved to appendix 8B. Some hydrodynamic data is averaged over the beach between cross-shore distance = 145 and 180 m (Figure 16) in order to understand the hydrodynamic processes in the final approach towards the dune foot.

The dune erosion over time as the result of storm impact was calculated as the dune front volume. The dune front at the start of the simulations is defined in figure 16 and contains a total volume of 647.27 m^3 per longshore metre. Variation in changes of mean dune front volume over time can be compared with the hydrodynamic conditions. The difference in magnitude of erosion and longshore positions between the single-dir and multi-dir method are evaluated as well. The magnitude of the sediment transport will be dissected in a cross-shore and longshore component and compared to multiple hydrodynamic parameters.

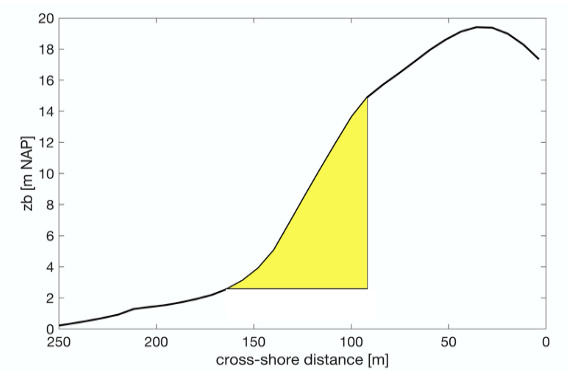

Figure 16: The yellow section of the dune is defined as the 'dune front'. The volume of the dune front for every longshore meter is the reference point for erosion.

4. Results

4.1 Wave angle effect

4.1.1 *Reference case: SFMaC*

High frequency waves

Under conditions where the incoming waves approach the shore under a 0° angle, a clear influence of the bathymetry can be observed. In general, the surf-zone can be defined as saturated, the high frequency energy has all been dissipated at the shoreward boundary.

In figure 17, the behaviour of the significant high frequency wave height ($\overline{H_{s,hf}}$) in the nearshore are depicted. At the seaward side of the outer bar, $\overline{H_{s,hf}}$ is longshore uniform. As the waves pass over the outer bar, differences start to develop (Figure 18a). At the location of the horns $\overline{H_{s,hf}}$ decreases in the shoreward direction but starts to increase again at 450 metre cross-shore distance. The bays show a more gradual decline in $\overline{H_{s,hf}}$ over the outer bar and towards the inner bar at 430 metre cross-shore distance (just shoreward off the -1-metre contour line). Notice that just seaward of the inner bar the $\overline{H_{s,hf}}$ is slightly higher at the horns than at the bays. This persists after the waves have passed the inner bar, where $\overline{H_{s,hf}}$ is still slightly higher at the longshore locations of the horns.

Where the outer bar is uniform, x = 0-500 metres and x = 5500-6000 metres, a different cross-shore trend in $\overline{H_{s,hf}}$ is observed than at the bays and horns. When the waves pass over the outer bar, their energy dissipates. There is a small increase in $\overline{H_{s,hf}}$ when approaching the inner bar after which it decreases shoreward.

The cross-shore variation in short wave energy led to cross-shore differences in set-up as well (Figure 18b). Over the seaward face of the outer bar, set-down is occurring at the bay as well as the horn. As the $\overline{H_{s,hf}}$ decreases less over the bay a relatively small set-up is observed, while the horn still experiences set-down. Towards the inner bar $\overline{H_{s,hf}}$ increases for both locations, resulting in a comparable set-down, although at the longshore location of the horn a larger increase in $\overline{H_{s,hf}}$ is observed. In the approach of the beach $\overline{H_{s,hf}}$ decreases for both locations, leading to a significant set-up.

In figure 18e the $\overline{H_{s,hf}}$ and mean set-up of the beach in the longshore direction depicts a variation conform the outer bar bathymetry. Over the beach, $\overline{H_{s,hf}}$ is relatively high on locations with horns, the larger decrease in $\overline{H_{s,hf}}$ in the approach of the dune foot, leads to a significantly larger set-up than longshore locations with embayments in the outer bar. Locations where the outer bar is uniform are characterized by $\overline{H_{s,hf}}$ and mean set-up values, which are roughly in between values of horns and bays.

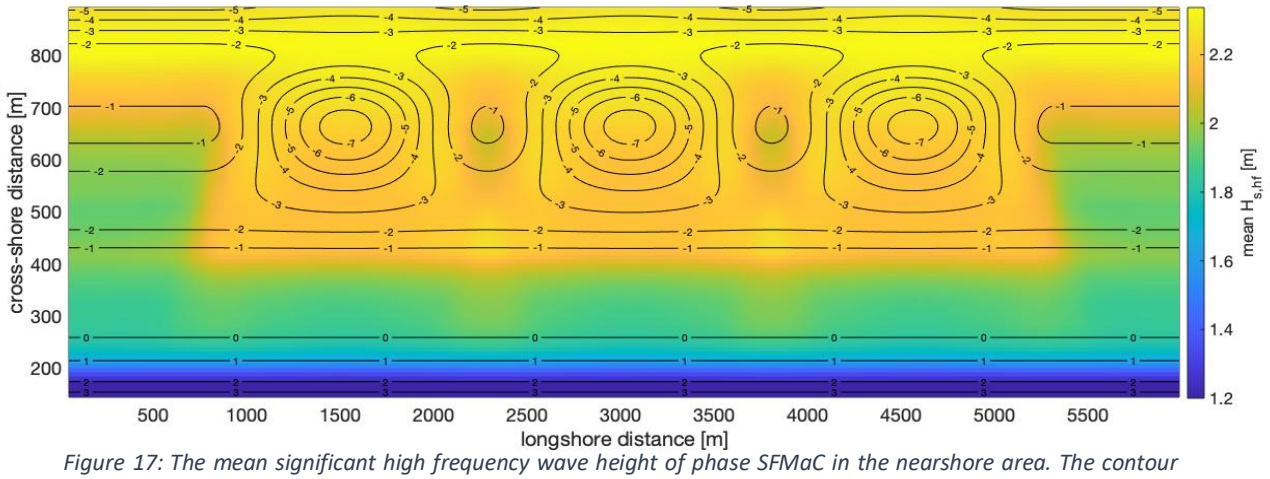

Figure 17: The mean significant high frequency wave height of phase SFMaC in the nearshore area. The contour lines represent the bed levels in metres NAP. The $\overline{H_{s,hf}}$ eventually becomes zero at the dune foot.

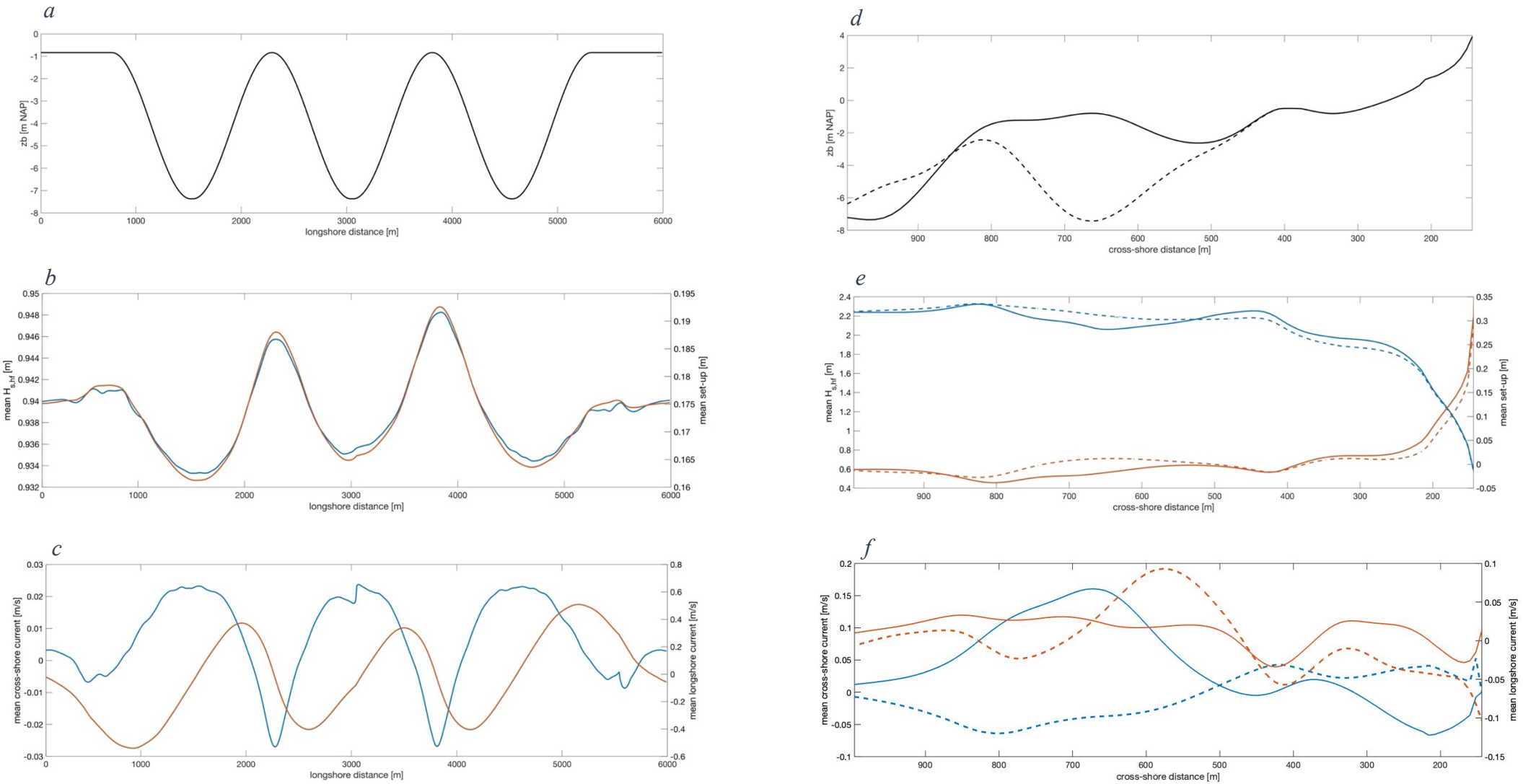

Figure 18: Figure 18a displays the longshore profile of the outer bar in metres NAP. In figure 18b the mean significant short-wave height (blue) is plotted averaged over the beach of phase SFMaC, On the right-hand x-axis the mean set-up is plotted in orange. Figure 18c displays both the cross-shore (blue) and longshore (orange) components of the mean current averaged over the beach. Figure 18d displays the cross-shore profile of a horn (solid) and an embayment (striped) in metres NAP. In figure 18e the mean significant short-wave height (blue) is plotted for the horn profile (solid) and the embayment profile (striped) of phase SFMaC. On the right-hand x-axis the mean set-up is plotted in orange. Figure 18f displays both the cross-shore (blue) and longshore (orange) components of the mean current.

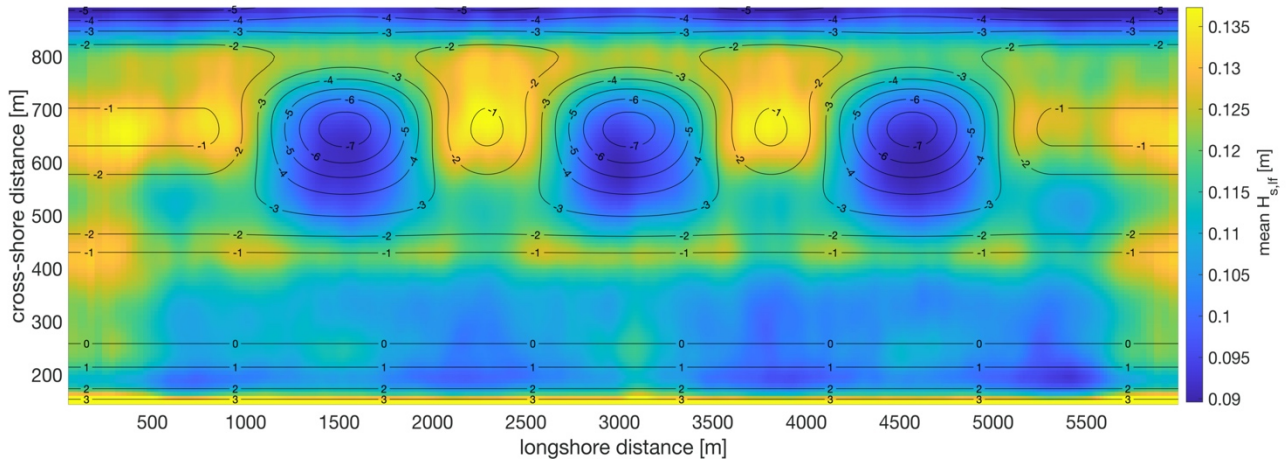

Figure 19: The mean significant IG wave height of phase SFMaC in the nearshore area. The contour lines represent the bed levels in metres NAP. A significant increase of mean IG height is visible at the dune foot. This is depicted in more detail in figure 20.

Low frequency waves

Figure 19 presents the mean IG wave height ($\overline{H_{s,lf}}$) in the nearshore area. On the outer bar the horn features experience an increase towards 13 centimetres in $\overline{H_{s,lf}}$ after which values decrease towards the shore. The embayments endure the opposite. On the outer bar, the $\overline{H_{s,lf}}$ first increases on the seaward side of the bar and then decrease over the bays. Towards the inner bar the mean IG wave height increases again, reaches larger heights than the longshore locations of the horns. Noteworthy is that the largest $\overline{H_{s,lf}}$ at the inner bar are at the longshore locations in between the horns and the bays, 11 to12 centimetres.
Locations where the outer bar is uniform, show the overall largest $\overline{H_{s,lf}}$ values in the longshore direction. The mean IG wave height increases over the outer bar, after which it declines and subsequently increases again towards the inner bar.

Towards the dune of the foot, the $\overline{H_{s,lf}}$ becomes significantly higher over the whole longshore dimension and reaches values up to 0.22 m, almost double of the surf zone values.
The constant conditions of phase 1 result in patterns at the foot of the dune which, in general, do not coincide with the outer bar morphology. Figure 20 shows that the dominant peaks in $H_{s,lf}$ are concentrated in the middle and on the longshore boundaries. The peak in the middle is at the same longshore position as the middle embayment of the outer bar. The peaks at the boundaries coincide with locations where the longshore grid size increases, and the outer bar is uniform. There are, however, lower values visible at the locations of the horns and also some small increases in IG wave height on the locations of the outer two bays.

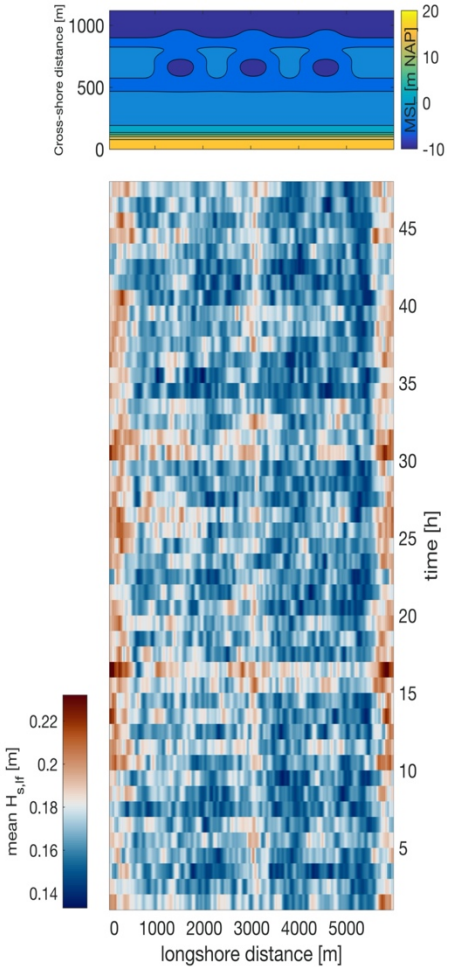

Figure 20: The upper panel displays the bathymetry with the location of the horns and bays. The bottom panel show the significant IG wave height at the dune foot in the longshore dimension over time.

Mean current

The combined mean cross-shore and longshore components of the current, lead to cell-circulation patterns, depicted in figure 21. Rip currents are visible over the bays, fed by the strong longshore currents of the trough between inner and outer bar. Another series of cells is present between the beach and inner bar (250 to 450 m cross-shore). The beach is characterized by a diverging current at bay locations and a seaward directed mean current occurs at horn positions.

The mean current is dissected in a cross-shore and longshore component, visible in detail in figure 18c and 18f. The differences between mean currents of locations with bay and horn, become immediately clear over the seaward face of the outer bar. The horn experiences an increasingly strong, shore-oriented mean cross-shore current over the outer bar. At the shoreward side of the horn, the current immediately declines in strength and the cross-shore component of the current becomes slightly offshore. Over the inner bar, the mean cross-shore current is oriented shoreward. Towards the beach, the cross-shore current becomes seaward again, reaching its largest velocity over the beach ridge (210 m cross-shore distance).

Along the cross-shore profile of a bay, opposite observations in cross-shore currents are visible (Figure 18d). A seaward oriented flow is visible over the bay, which becomes shoreward over the trough between the inner and outer bar. A decrease in this shoreward current occurs over the inner bar, followed by a slight increase in the approach of the beach.

For the mean longshore component of the current, large differences between bay and horn occur at the shoreward face of the outer bar, where the bays experience a stronger longshore current. Over the beach the mean longshore component of the horn is relatively close to 0 m/s, while an increase in current magnitude is observed at the location of the bay.

Averaged over the cross-shore distance of the beach, the mean cross-shore current is shore-oriented at the position of the embayments, while at the horns the mean cross-shore current is offshore directed. The mean longshore current on the beach is 0 m/s at the positions of both bay and horn. On the boundaries of horn and bay, the mean longshore current is strongest.

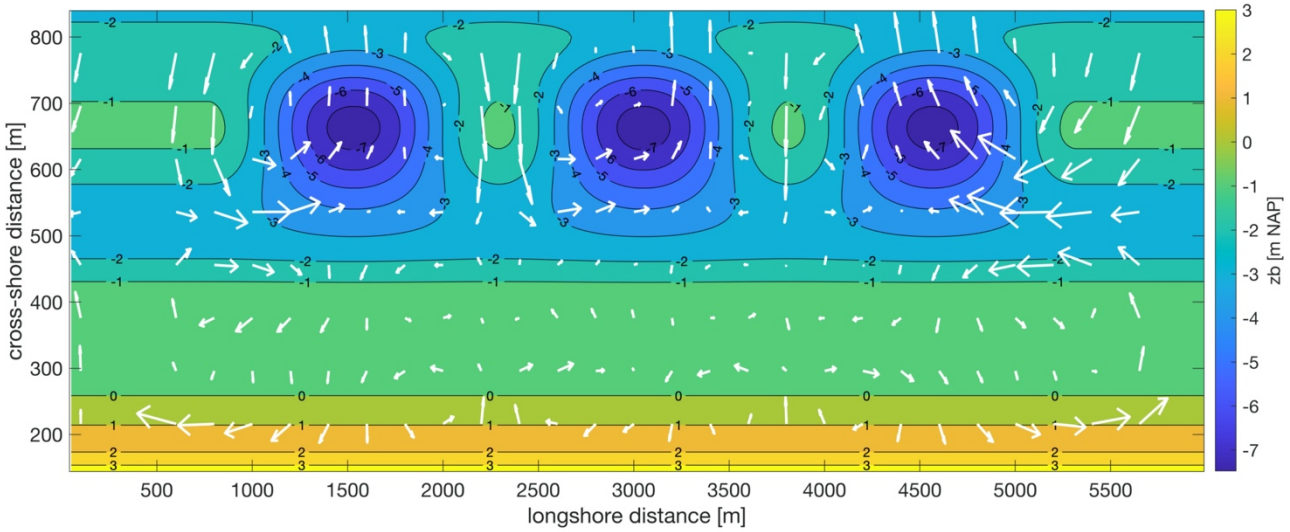

Figure 21: The mean current of phase SFMaC is indicated by the white arrows. The size of the arrow is an indication for the magnitude of the current. Cell circulations can be observed, with rip currents located at the bays.

4.1.2 *SFMcC, constant 45 °*

High frequency waves

With a wave angle of 45°, results are significantly different than in section 4.1.1. Under 45° wave conditions the $\overline{H_{s,hf}}$ moves over the seaward face of the outer bar with a value 10-30 centimetres lower than under 0° conditions (Figure 18e). Over the trough between the outer and inner bar, a 20 centimetre higher $\overline{H_{s,hf}}$ is observed over the cross-shore profile of a horn than in the case of a bay. This coincides with a 5-centimetre lower set-down over the horn (Figure 23e). After passing the inner bar, $\overline{H_{s,hf}}$ decreases towards zero at the dune foot, resulting in an increase in set-up to 30 centimetres (Figure 23e). This is 5 centimetres less than the 0° wave conditions.

Averaged over the beach, relatively high values of $\overline{H_{s,hf}}$ over the longshore dimension are observed slightly right of the horn positions in the direction of wave propagation. Peaks are also visible at 800 and 5200 metres longshore distance. Low values of $\overline{H_{s,hf}}$ and set-up are observed slightly right of the bay positions. The maximum differences between in these longshore locations is 3 centimetres (Figure 22b).

From the $\overline{H_{s,hf}}$ depicted in figure 22, the relation with bathymetry can be distinguished over the whole nearshore area. Moving over the outer bar the $\overline{H_{s,hf}}$ increases under a 45° on locations with a bay. This phenomenon does not occur over the centre of the bays, but towards the right of the centre. The increasing $\overline{H_{s,hf}}$ even moves over the shoreward face of the horns. When this pattern approaches the inner bar (450 m cross-shore) the energy starts to dissipate. It seems that between 450 and 250 m cross-shore distance the 45° angle disappears and the locations with a higher $\overline{H_{s,hf}}$ lose their energy under shore normal conditions (x = 2500, 4000 and 5500 m longshore distance).

Shadow zones occur on the shoreward face of the outer bar on the left-hand side of the bays. If these shadow zones are followed in a 45° line, a small increase is observed towards the inner bar, after which the energy is dissipated towards the dune foot.

At the right-hand uniform outer bar and its boundary with the adjacent bay, another interesting feature can be seen. While on the uniform bar the waves gradually lose their energy moving across the outer bar, at 1000 m longshore a persistently high $\overline{H_{s,hf}}$ is visible. Here, the waves approach the shore under a smaller angle than the other bay features at 2500, 4000 and 5500 m longshore distance have a lower $\overline{H_{s,hf}}$, relative to the bay features.

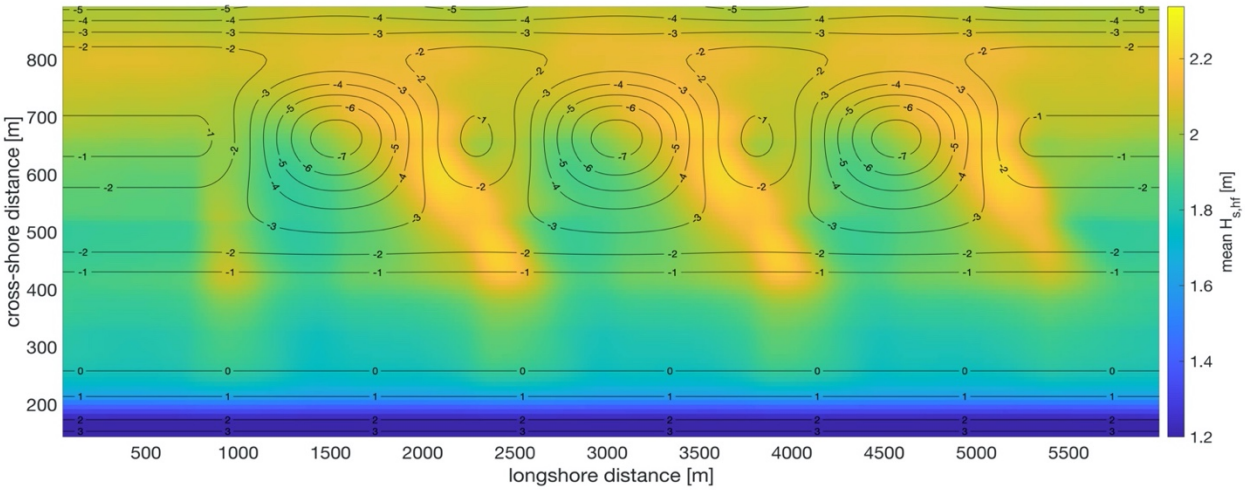

Figure 22: The mean significant high frequency wave height of phase SFMbC in the nearshore area. The angle of the incoming waves is -45°. The contour lines represent the bed levels in metres NAP. The $\overline{H_{s,hf}}$ eventually becomes zero at the dune foot.

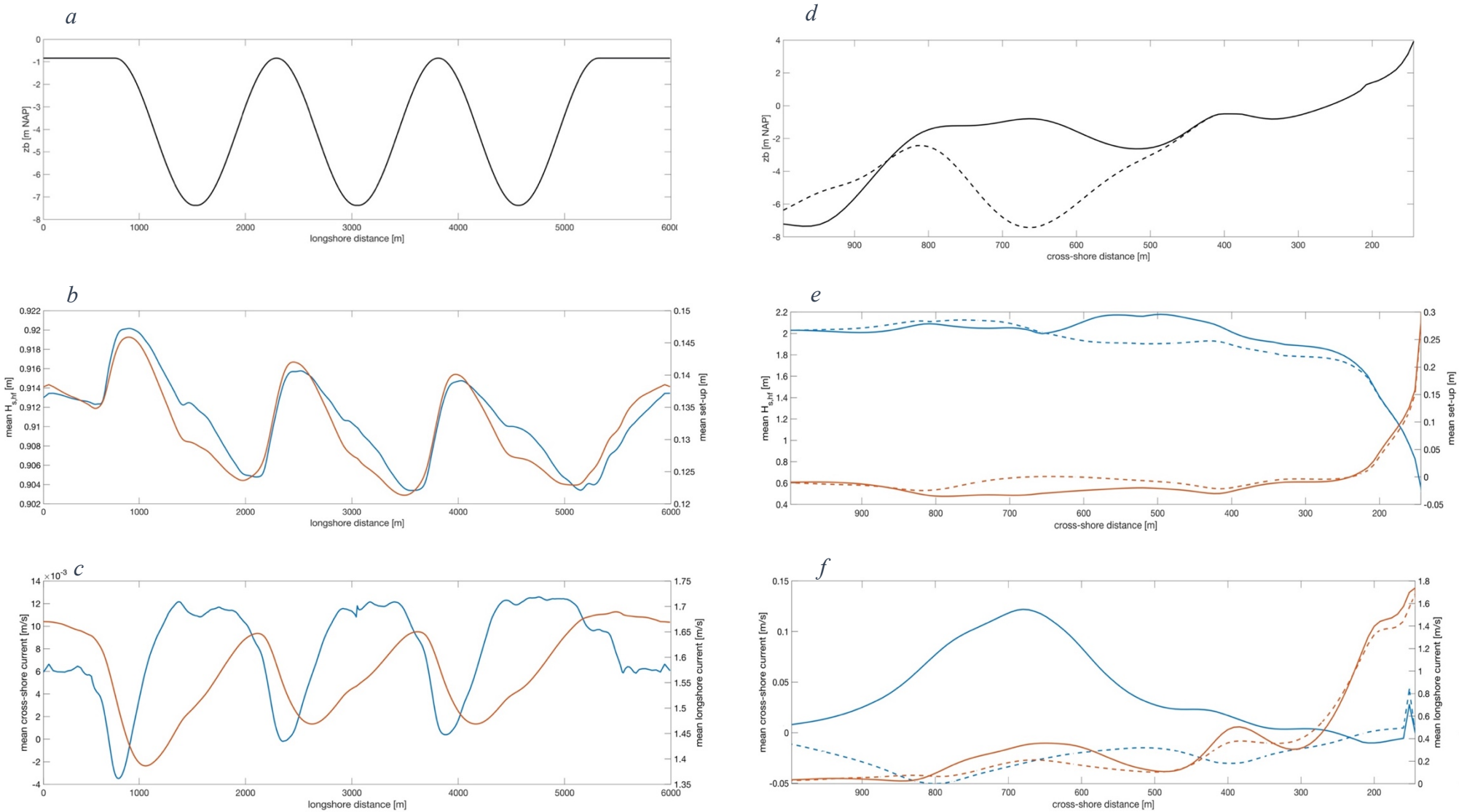

Figure 23: Figure 23a displays the longshore profile of the outer bar in metres NAP. In figure 23b the mean significant short-wave height (blue) is plotted averaged over the beach of phase SFMaC, On the right-hand x-axis the mean set-up is plotted in orange. Figure 23c displays both the cross-shore (blue) and longshore (orange) components of the mean current averaged over the beach. Figure 23d displays the cross-shore profile of a horn (solid) and an embayment (striped) in metres NAP. In figure 23e the mean significant short-wave height (blue) is plotted for the horn profile (solid) and the embayment profile (striped) of phase SFMaC. On the right-hand x-axis the mean set-up is plotted in orange. Figure 23f displays both the cross-shore (blue) and longshore (orange) components of the mean current.

Low frequency waves

The $\overline{H_{s,lf}}$ under 45° conditions show major differences compared to the 0° results (Figure 19). The $\overline{H_{s,lf}}$ increases over the seaward face of the outer bar (Figure 24). These features, however, occur in a gradient of magnitudes in the longshore dimension. On the longshore location of the bays, the bay at x = 1500 n has the lowest $\overline{H_{s,lf}}$ over the seaward face as well as the shoreward face of the outer bar. Approaching the inner bar, $\overline{H_{s,lf}}$ increases again over a broad longshore area, positioned slightly to the left of the bays. The embayment at x = 4500 m endures the highest $\overline{H_{s,lf}}$ in the approach of the shore (y = 450 to 200 m).

As the IG waves move over the horns of the outer bar, the mean height increases roughly 3 to 4 cm. The horn at x = 3800 m has a higher $\overline{H_{s,lf}}$ then the horn at x = 2300 m. Interestingly, the right most uniform outer bar, experiences the largest values of the longshore dimension. On the left-hand uniform outer bar, a significantly smaller increase over the outer bar is observed at the edge of the study area, with differences up to 4 cm.

After the waves have passed the horns, a relatively narrow area with a decrease in $\overline{H_{s,lf}}$ is visible at x = 1000, 2500 and 4000 m. These features are oriented almost perpendicular to the shoreline. Longshore variation is also present in these features, with the location of the left horn enduring the lowest values of $\overline{H_{s,lf}}$ with the approach of the shore.

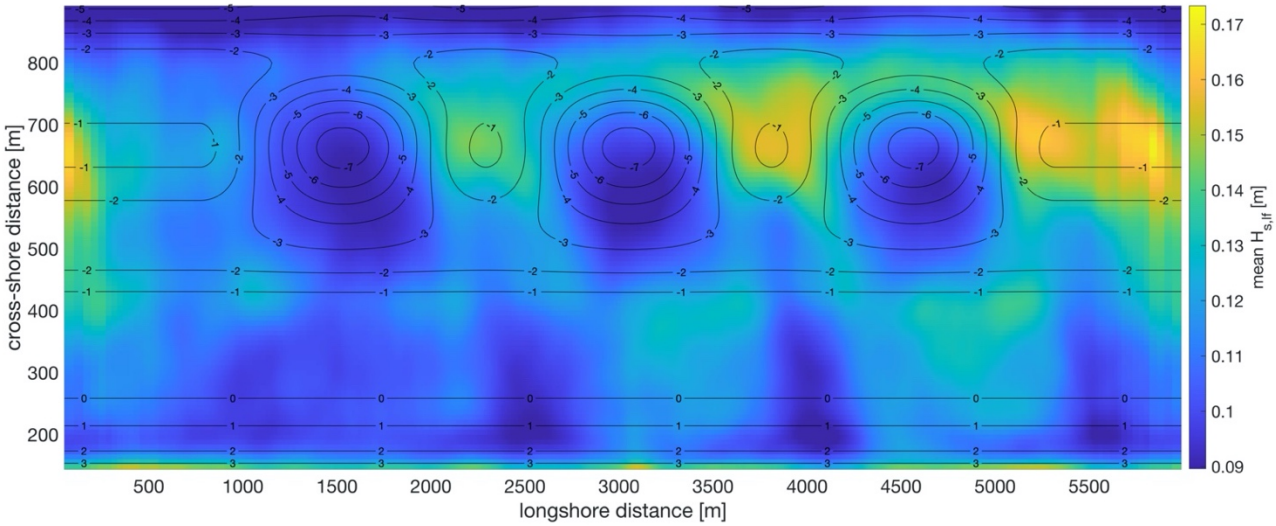

Figure 24: The mean significant IG wave height of phase SFMbC in the nearshore area. The contour lines represent the bed levels in metres NAP. A significant increase of mean IG height is visible at the dune foot. This is depicted in more detail in figure 26a.

Mean current

The cell circulation present in section 4.1.1 is significantly less dominant under a 45° wave angle (Figure 25). Over the outer bar profile, the cross-shore component of the mean current is shore-oriented and subsequently decreases to zero in the approach of the beach. On the beach a small increase in shoreward directed mean current velocity is observed (Figure 23f). The longshore component of the mean current has significantly larger mean velocities. An increase in longshore mean current velocity is observed over the outer bar, with the largest increase at the horn. At this location, mean longshore current velocity reaches values of 0.4 m/s. This is also visible over the inner bar (Figure 23f). Towards the beach, a steep increase in mean longshore current is observed reaching values over 1.6 m/s, while under a 0° wave angle the mean longshore current reaches a maximum of -1 m/s at this location.
Averaged over the beach, the mean cross-shore currents have a relatively low velocity, with a maximum value of 0.012 m/s and a minimum of -0.003 m/s (Figure 23c). Still, variation is observed over the longshore dimension. Longshore locations left of peaks in set-up endure the lowest onshore currents. At x = 5200 m, even a small offshore directed current is observed. Overall, the cross-shore current over the beach is an order of magnitude smaller than under a 0° wave angle. The longshore component reaches a maximum velocity of 1.7 m/s. The lowest mean longshore currents are observed on locations slightly left of the bay positions, with values varying between 1.4 and 1.5 m/s at x = 1050, 2550, 4050. Stronger currents are observed right of the horn positions, with velocities of 1.65 m/s.

Due to a strong longshore mean current at the foot of the dune, hardly any remains of the cell circulation are visible on the beach (Figure 25). Between the inner bar and the beach (y = 450-250), the left-oriented flow increasingly starts to meander in the seaward direction. In this area, longshore locations with bays endure a slightly seaward oriented current, while the horns experience the opposite.
Over the outer bar the remains of a cell circulations are strongest. Over two outer bays the strongest rip currents are visible, with a magnitude of roughly 0.1 m/s in the seaward direction. In these cases, the flow originates from the left-hand uniform bar and the right-hand horn. The overall result of the 45° is a meandering longshore oriented current, without distinctive cell circulation patterns.

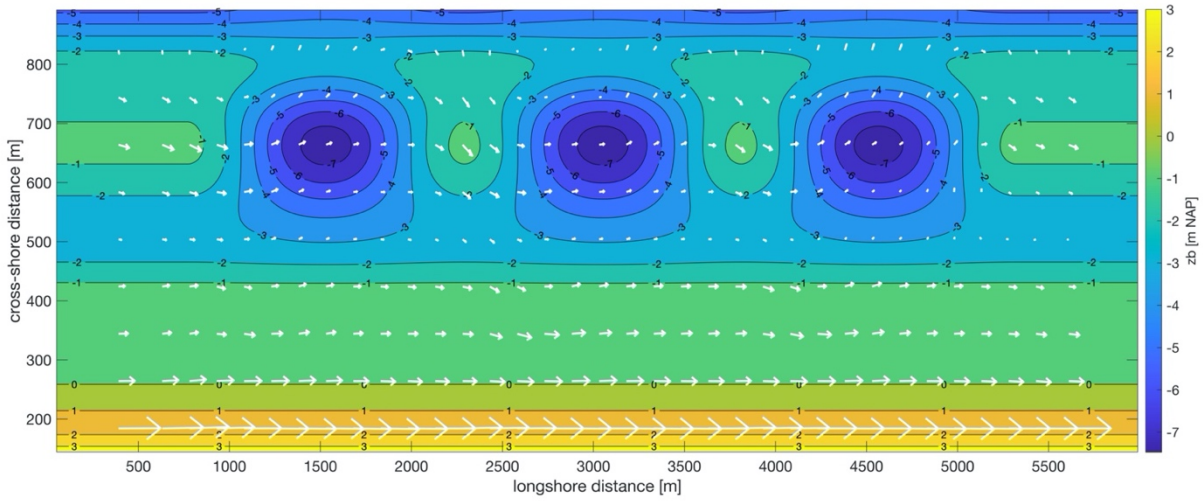

Figure 25: The mean current of the -45 °interval of phase SFMbC. The size of the arrow is an indication for the magnitude of the current. The system is dominated by longshore currents, although some remains of cell circulation patterns are still visible.

4.1.3 *SFMbC & SFMcC, varying wave angles*

In figure 26 the IG wave height at the foot of the dune is depicted for both the 5° time-constant wave angles and the time-varying 45° wave angle. Figure 26a shows that for every 5° interval, a longshore variation in $\overline{H_{s,lf}}$ can be observed at the foot of the dune.
The variation in $\overline{H_{s,lf}}$ due to differences in wave angle results in a sequence of crests and troughs in the longshore dimension at the foot of the dune. The crests have higher values of $\overline{H_{s,lf}}$, with maximum values of 19 cm, and the troughs have lower values of $\overline{H_{s,lf}}$ (13 cm, figure 26a). In general, smaller incoming wave angles, especially -10° to 10° , display a less distinctive the crest-trough pattern. Still, high values of $\overline{H_{s,lf}}$ can be observed at longshore positions where a bay is present in the outer bar, while lower values occur where horns are the dominant feature. For these wave angle intervals, $\overline{H_{s,lf}}$ values of 19-20 cm are also observed at the longshore boundaries of the model. Under larger wave angles s more distinctive longshore distribution of $\overline{H_{s,lf}}$ and a larger difference between crest and trough is visible. The position of crests and troughs is slightly shifted, relative to the position of the bays and horns of the outer bar. At -45°, the waves enter the model from the left, a shift in the pattern of $\overline{H_{s,lf}}$ to the right is observed. Under 45° the opposite occurs, incoming waves from the right, shift the pattern slightly to the left. The leeward crest and troughs consist of the highest values of $\overline{H_{s,lf}}$.
Considering figure 26b, the longshore patterns in $\overline{H_{s,lf}}$ are comparable to the mean results of the 5° interval simulations. The longshore crests and troughs of $\overline{H_{s,lf}}$ coincide with the bathymetry of the outer bar and their positions shifts slightly conform the variation in wave angle. The leeward $\overline{H_{s,lf}}$ crest (at x = 5000 m when θ < -20° and x = 1000 m when θ > 20°) has, compared to the other crests, the highest values of $\overline{H_{s,lf}}$, up to 19 cm. Between -20° to 20° an increase in wave height at the longshore boundaries is visible. This corresponds to location with relatively large longshore grid size and a uniform outer bar. The crest-trough sequences become less distinct for this wave angle interval.

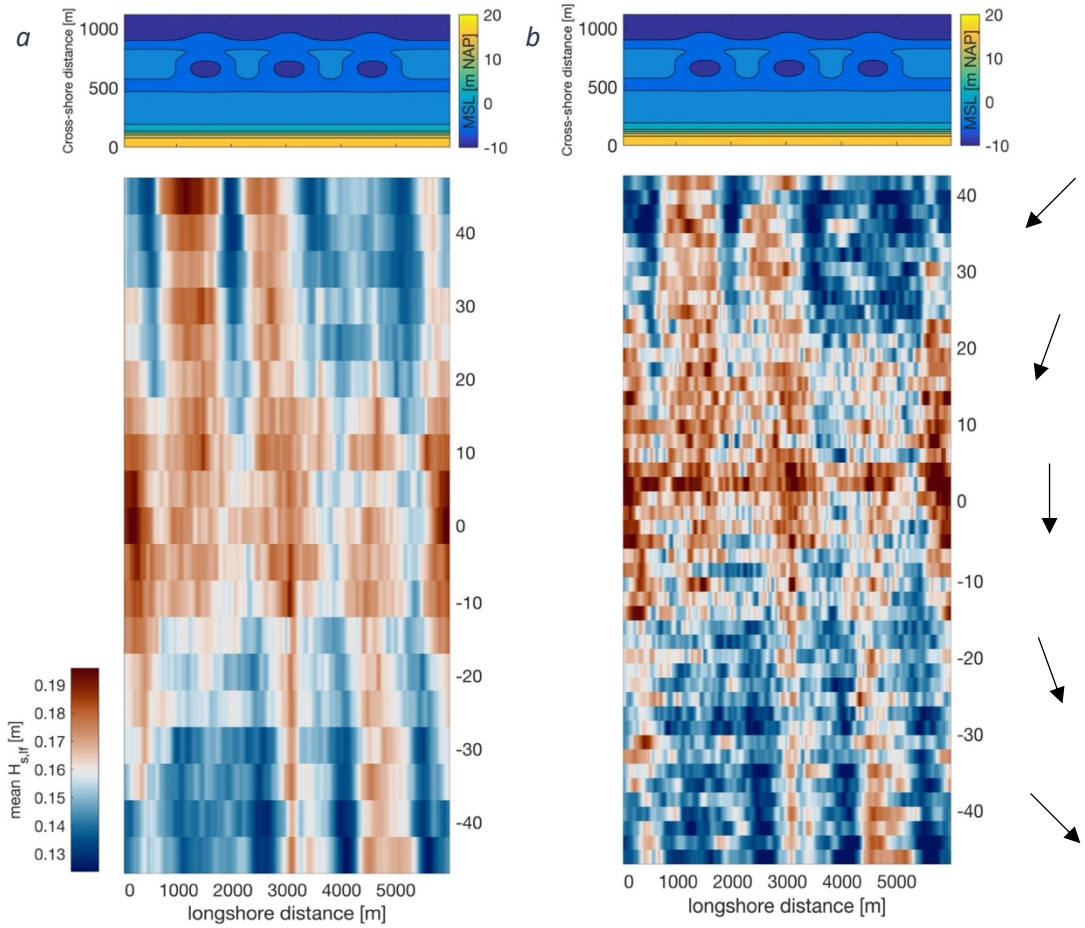

Figure 26: The upper panel in both 26a and 26b displays the bathymetry with the location of the horns and bays. The bottom panels show the mean significant IG wave height at the dune foot, indicated by a colour scale. Figure 26a represents the $\overline{H_{s,lf}}$ over every 5 °interval, while figure 26b displays the $\overline{H_{s,lf}}$ under slowly continuously changing wave angle, indicated by the black arrows.

4.2 Wave height effect

4.2.1 *SFMaV, low versus high $H_{s,hf}$*

High frequency waves
With a varying short-wave height over time and a constant wave angle of 0°, the distribution of wave energy in the nearshore area changes. For the period where the incoming $H_{s,hf}$ is lower than 3 metres, the $\overline{H_{s,hf}}$ hardly varies between horn and bay profiles over the seaward face of the outer bar (Figure 27e). It is over the centre of the outer bar that the values of $\overline{H_{s,hf}}$ start to differ. The largest difference between the horn profile and the bay profile is observed at x = 400 m and reaches a value of 25 cm (Figure 27e). Shoreward of the inner bar an increasing decline towards 0 m is observed over the beach and eventually the dune foot.
Cross-shore difference in set-up between the bay and horn profile are particularly present over the outer bar and the beach. Over the outer bar, the bay profile experiences 2 cm less set-down, while on the beach the horn profile endures a 2 cm higher set-up.
Averaged over the beach, longshore profiles of $\overline{H_{s,hf}}$ and set-up show the same pattern as described in section 4.1.1 (Figure 18b). In both cases high values are observe on positions with horns, while relatively low values are observed at bay positions (Figure 27b). The difference between outer bar features leads to a difference of 1-2 cm for both $\overline{H_{s,hf}}$ and set-up.
For the period of the simulation where $H_{s,hf}$ is higher than 4 metres, $\overline{H_{s,hf}}$ decreases over the outer bar (Figure 27e). The horn profile experiences a larger decrease, coinciding with a relatively low set-up. Toward the inner bar the horn profile endures an 18 cm larger increase in $\overline{H_{s,hf}}$ than the bay profile. The final approach towards the beach is characterized by an increasing decline towards 0 m in $\overline{H_{s,hf}}$, with the horn profile a 5 cm higher in $\overline{H_{s,hf}}$, than the bay profile. The longshore profiles of the beach indicate that the highest values of set-up and $\overline{H_{s,hf}}$ are observed at horn positions, while the longshore minima are located at bay positions (Figure 27b). Compared to the low $H_{s,hf}$ conditions, a 20 cm larger $\overline{H_{s,hf}}$ is observed averaged over the beach.
In figure 28a & 28d an overview of the spatial distribution of $\overline{H_{s,hf}}$ is given. The mean short wave energy distribution over the bathymetry is significantly different under low $H_{s,hf}$ conditions. While a $H_{s,hf}$ higher than 4 metres result in a distribution similar to section 4.1.1, but with more energy dissipation in the shoreward direction. At the inner bar a 70 cm decline in $\overline{H_{s,hf}}$ occurred, while in section 4.1.1. this is only 20 cm.

Low frequency waves
The distribution of the mean IG wave height in the nearshore area under low and high short-wave conditions are presented in, relatively, figure 28b and 28e. The $\overline{H_{s,lf}}$ averaged over a period with a low short-wave height, leads to overall lower values in the range of 5 to 9 cm. A lot of similarities are present with the IG distribution of section 4.1.1 (Figure 19). The $\overline{H_{s,lf}}$ increases over the seaward face of the outer bar. This persists over the horns. On the shoreward face of the horn, the $\overline{H_{s,lf}}$ decreases slightly followed by a small increase of 1 cm towards the inner bar y = 450 m. The $\overline{H_{s,lf}}$ over the bays is significantly lower. Towards the inner bar the IG wave energy rises gradually. Interestingly, between the zero and 1 metre NAP contour line, an increase of $\overline{H_{s,lf}}$ is observed at the locations of the bays (x = 1500 m, 3000 m and 4500 m). These heights are similar to the $\overline{H_{s,lf}}$ at the longshore locations of the uniform bars (x = 250 m and x = 5500 m).
When the results are averaged over a period with a significant short-wave height higher than 4 metres, the distribution becomes more distorted (Figure 28e). The $\overline{H_{s,lf}}$ has an overall larger magnitude ranging between 12 to 19 cm. At the seaward face of the outer bar the highest values of $\overline{H_{s,lf}}$ are observed along the whole longshore dimension (16-19 cm). When passing over the bays, the $\overline{H_{s,lf}}$ decreases towards 14 cm, until a rise in to 16 cm at inner bar occurs. Higher values seem to persist from x = 450 m to 200 m on the longshore boundary positions of the bays and horns.

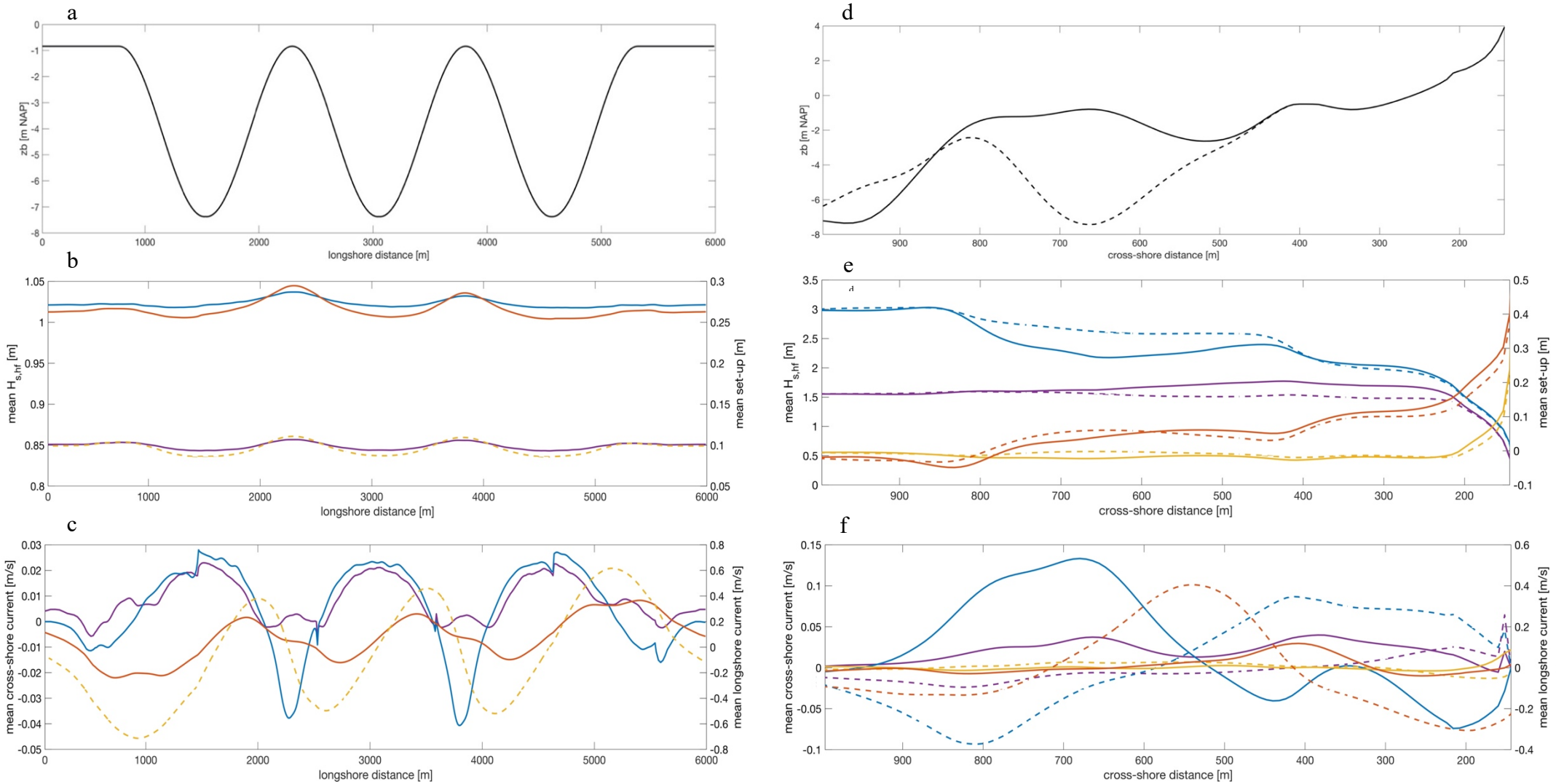

Figure 27: Figure 27a displays the longshore profile of the outer bar in metres NAP. In figure 27b the mean significant short-wave height (purple for $H_{s,hf}$ < 3 m and blue for $H_{s,hf}$ > 4 m) is plotted averaged over the beach of phase SFMaV, On the right-hand x-axis the mean set-up is plotted in orange and in yellow, dotted for respectively $H_{s,hf}$ < 3 m and $H_{s,hf}$ > 4 m. Figure 27c displays both the cross-shore (purple for $H_{s,hf}$ < 3 m and blue for $H_{s,hf}$ > 4 m) and longshore (yellow, dotted for $H_{s,hf}$ < 3 m and orange for $H_{s,hf}$ > 4 m) components of the mean current averaged over the beach. Figure 27d displays the cross-shore profile of a horn (solid) and an embayment (striped) in metres NAP. In figure 27e the mean significant short-wave height (purple and blue) is plotted for the horn profile (solid) and the embayment profile (dotted) of phase SFMaV. On the right-hand x-axis the mean set-up is plotted in yellow and orange. Figure 27f displays both the cross-shore and longshore components of the mean current.

Over the horns high $\overline{H_{s,lf}}$ seems to persist, compared to the bays, but in the approach of the inner bar and the 0 metres contour line, it gradually decreases. The uniform outer bars are characterized by high values on the seaward face, after which the $\overline{H_{s,lf}}$ decreases (but not as fast as over the bays). From y = 450 to 250 m the uniform outer bars have relatively high values (16-17 cm). At the 1 metre contour line the same values as the bay locations are observed. Approaching the dune foot, an increase toward 23 cm is observed, which is presented in more detail in figure 29.

Mean currents

Averaged over period with a low $H_{s,hf}$, both cross-shore and longshore currents are in the same order of magnitude. The cross-shore component of the mean current under a $H_{s,hf}$ lower than 4 metres is different from the reference case. Over the outer bar of the horn profile, x = 700, the shoreward oriented current is 0.1 m/s slower and over the inner bar at x = 400, the current is 0.04 m/s faster (Figure 18f and 27f). The bay profile of low $H_{s,hf}$ conditions has an offshore directed current of a lower magnitude of 0.03 m/s. The longshore component of the mean current is in general an order of magnitude smaller than the reference case.

Over the period with a $H_{s,hf}$ higher than 4 metres, similar cross-shore currents are observed to section 4.1.1. Compared to section 4.1.1 the behaviour of the cross-shore component of the mean current is similar. There are some differences in magnitude over the outer bar at x = 700. The horn profile of the reference case has a 0.02 m/s stronger onshore current. While the offshore current of the bay profile is 0.03 m/s stronger in the case of a higher $H_{s,hf}$. However, the longshore component of the mean current under high $H_{s,hf}$ shows some differences with section 4.1.1. Over the trough the bay profile endures a longshore mean current of 0.4 m/s. In the approach of the beach the current changes direction, eventually reaching a maximum of 0.3 m/s at x = 200 m. The horn profile experiences its strongest currents over the inner bar at x = 400 m. Averaged over the beach (x = 50), this results in a mean offshore directed current at horn position. The longshore position of the bays is characterized by an onshore orientation of the cross-shore current component.

The peak velocities of the longshore current component are 90° out of phase with the peaks in $\overline{H_{s,lf}}$, set-up and cross-shore shore currents (Figure 27c), which is also comparable to section 4.1.1.

In the overview of the currents under low wave energy conditions (Figure 28c) the circulation cells are less distinct than patterns in section 4.1.1. Over the beach, locations with a horn (x = 2300 and 3800 m) in the outer bar are significantly different under low energy as well. In figure 21 and 28f a strong offshore current is present over the beach at y = 200, while in figure 28c the current over the horn profile is onshore directed until its final approach of the dune foot.

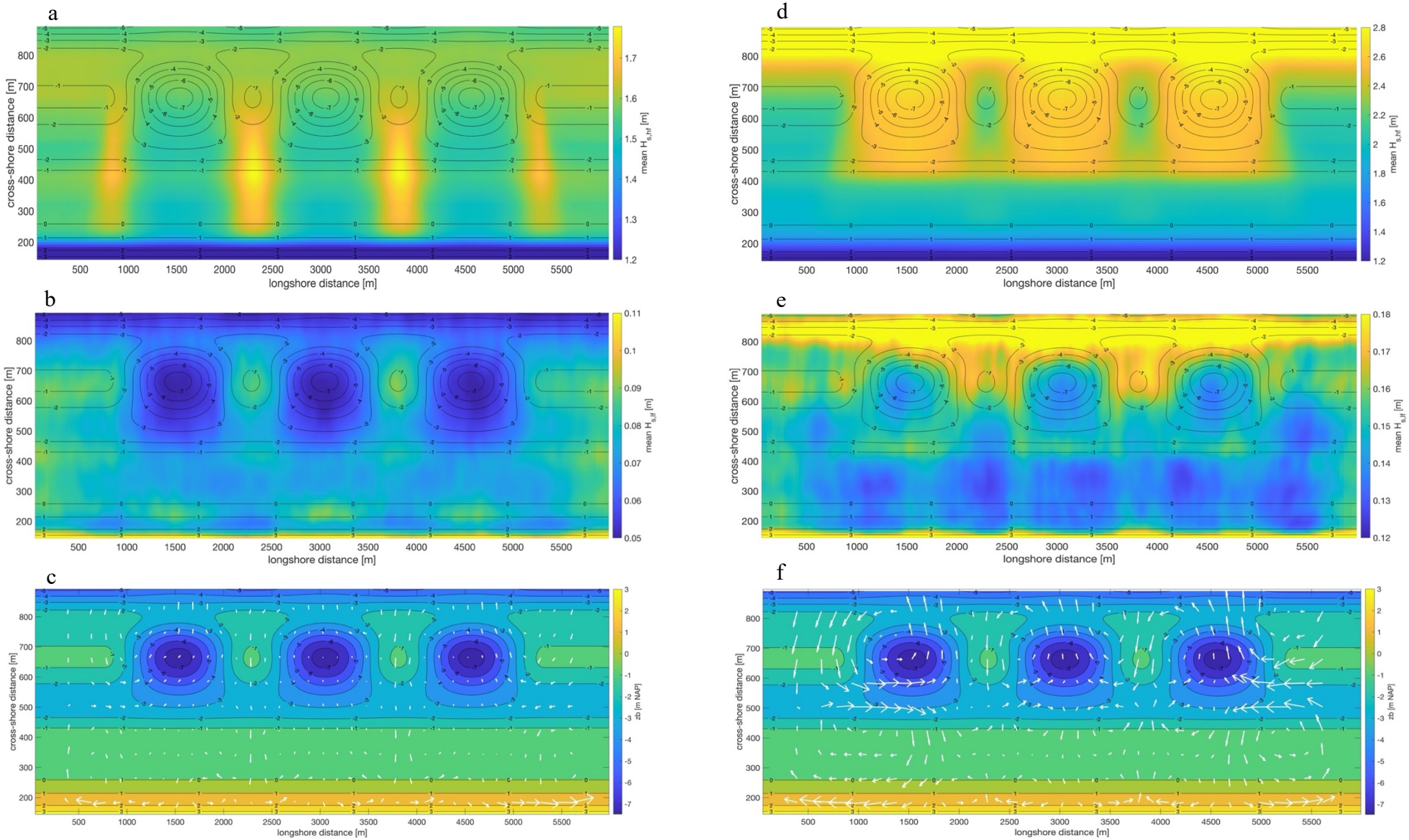

Figure 28: Figure 28a displays the mean significant high frequency wave height of phase SFMaV in the nearshore area. These results are averaged over the period where $H_{s,hf}$ is lower than 3 metres. The contour lines represent the bed levels in metres NAP. The $\overline{H_{s,hf}}$ eventually becomes zero at the dune foot. In figure 28d the mean high frequency wave height is plotted for phase SFMaV with a $H_{s,hf}$ higher than 4 metres. Figures 28b and 28e display the mean significant low frequency wave height of phase SFMaV in the nearshore area for respectively a $H_{s,hf}$ < 3 m and $H_{s,hf}$ > 4 m. Figures 28c and 28f indicate the mean current in the nearshore area. The size of the white arrows indicates the magnitude of the mean current.

4.2.2 *SFMcV, low versus high* $H_{s,hf}$

In this section the results of a time-varying $H_{s,hf}$ for both a time-constant and time varying wave angle. When normalized IG results with a constant 0° wave angle are compared to the normalized results with a time-varying wave angle (Figure 29) there are some similarities. Under the time-varying wave angle conditions, the crest-trough pattern also starts to form after the start of the simulation. The longshore position of the crests and troughs is slightly to the left of the outer bar features. Around 15 hours into the storm and under small wave angles, the pattern starts to disappear and the $H_{s,lf}$ crests at the longshore boundaries start to form. Some leftover patches of the crests at the locations of the bays are still present. After 35 hours and a H_s of 3.1 metre the pattern starts to form again. There are differences in the longshore $H_{s,lf}$ distribution compared with the first half of the storm. The crests have higher values, and the troughs are deeper in the post-peak conditions. In the second half, the difference between the crests at the moment in time is quite significant as well, with the leftmost as the highest and the rightmost as the lowest crest. For the mean short-wave energy and the mean current spatial distribution, it is assumed that similar results occur. With the physical processes in the nearshore area resulting in a state in between the -45° results of section 4.1.2 and the 0° results of section 4.1.1. In short, a lower $H_{s,hf}$ leads to a clearer pattern in the mean longshore IG wave height distribution, while a larger $H_{s,hf}$ results in a disturbed distribution.

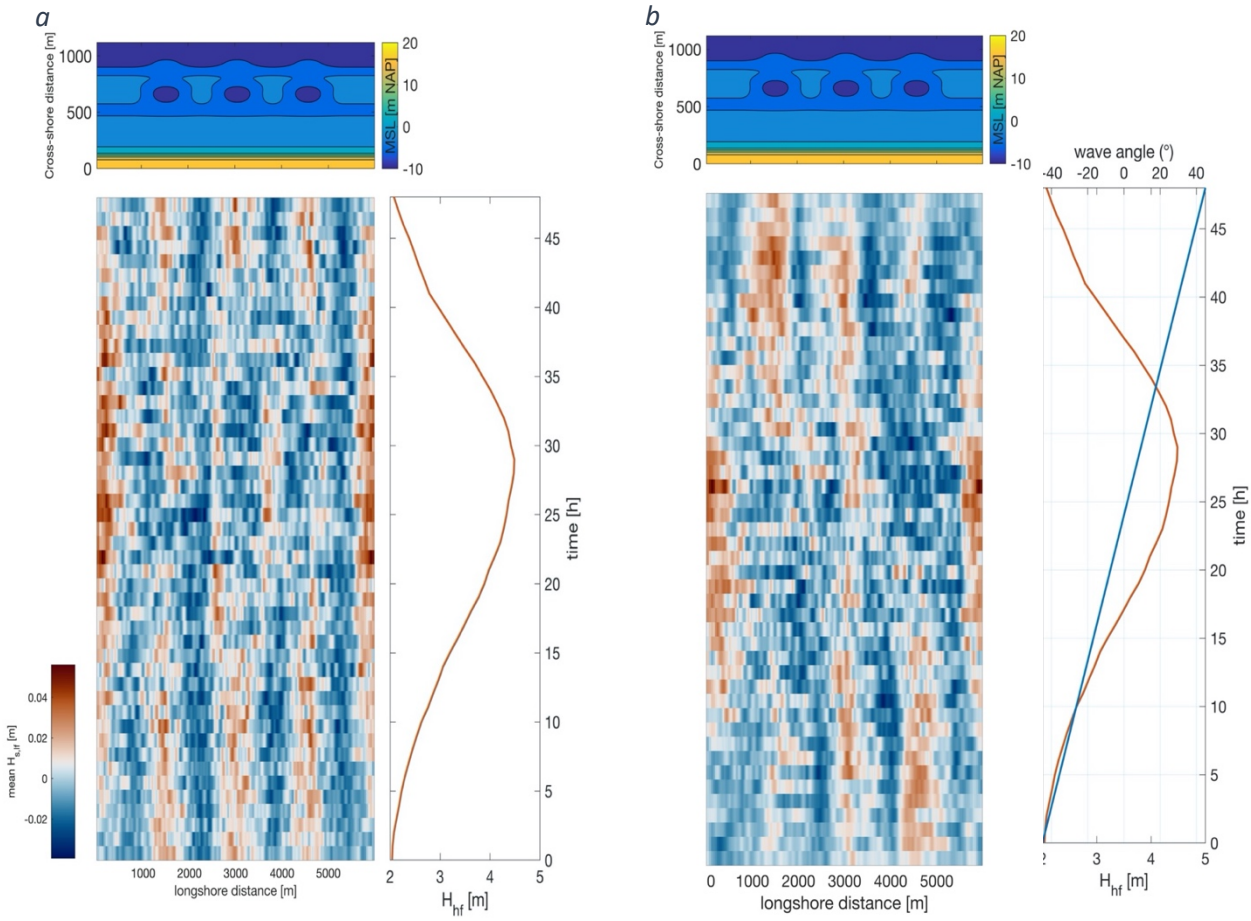

Figure 29: The upper panels display the bathymetry with the location of the horns and bays. The bottom panels show the normalized mean significant IG wave height over time at the dune foot in the longshore direction. The panel on the right displays the change in incoming significant wave height over time for 29a. Figure 29b also includes the change in wave angle over time.

4.3 Single-dir effect

4.3.1 *Reference case: SFSaC*

High frequency waves
When the single-dir option is applied under a constant 0° wave angle, differences in $\overline{H_{s,lf}}$ compared to the multi-dir method become visible. In figure 30a the $\overline{H_{s,hf}}$ is uniform over the seaward face of the outer bar. Over the horn profile, a decrease of $\overline{H_{s,hf}}$ is observed (Appendix 8B.2.2, Figure 62b), which is results in a 15 cm lower $\overline{H_{s,hf}}$ over the trough (x = 650 m) than the multi-dir results of. At x = 300 m, the difference in $\overline{H_{s,lf}}$ between the horn and bay profile using the single-dir method is double the difference of the multi-dir method.
Averaged over the beach, the longshore distribution of $\overline{H_{s,hf}}$ resembles the multi-dir results, with high values on horn positions and low values on bay positions (Appendix 8B.3.1, Figure 64b). Additionally, two extra peaks are present on the positions where the uniform outer bar meets the embayments (x = 800 and 5200 m). Remarkably, single-dir data is characterized by small variations in the longshore dimension. The longshore variation in set-up coincides with $\overline{H_{s,hf}}$, but show fewer small variations. Set-up values of the single-dir have a 3 cm larger range between minimum and maximum values in the longshore dimension, compared to the multi-dir results. In general, energy is dissipated faster in the nearshore area under single-dir results. The response of $\overline{H_{s,hf}}$ and set-up to the bathymetry are similar to the multi-dir results, only the peaks are, respectively, 2 and 1.5 cm higher for the single-dir method.

Low frequency waves
The behaviour of the IG wave energy in the nearshore are similar for both methods. In single-dir mode overall larger values of $\overline{H_{s,lf}}$ are observed than in the multi-dir method, with up to 10 cm higher values in the near-shore are using the single-dir method (Figure 30b) and 20 cm higher values at dune foot.
Compared to the results of *SFMaC, the* crest-trough pattern is more distinct in the spatial distribution of $\overline{H_{s,lf}}$ (Figure 18 and 30b), as well as in the longshore distribution at the foot of the dune (Appendix 8B.1, Figure 60).

Mean currents
The currents in the nearshore area (Figure 30c) as a result of the single-dir calculations are relatively similar to the multi-dir results in section 4.1.1. Cell circulation patterns are dominant, with seaward oriented rip currents in the bays. Some differences in current orientation between the two methods occur at the rightmost rip current (x = 5000, y = 650). Single-dir has a slightly stronger offshore current. While at the foot of the dune the longshore currents at the boundaries of the outer bays and the uniform outer bars seem slightly stronger under multi-dir calculations (Figure 30c, x = 500 and x = 5500).
Averaged over the beach the cross-shore component of the mean current is characterized by small variations over the whole longshore dimension (Appendix 8B.2.2, Figure 62c).

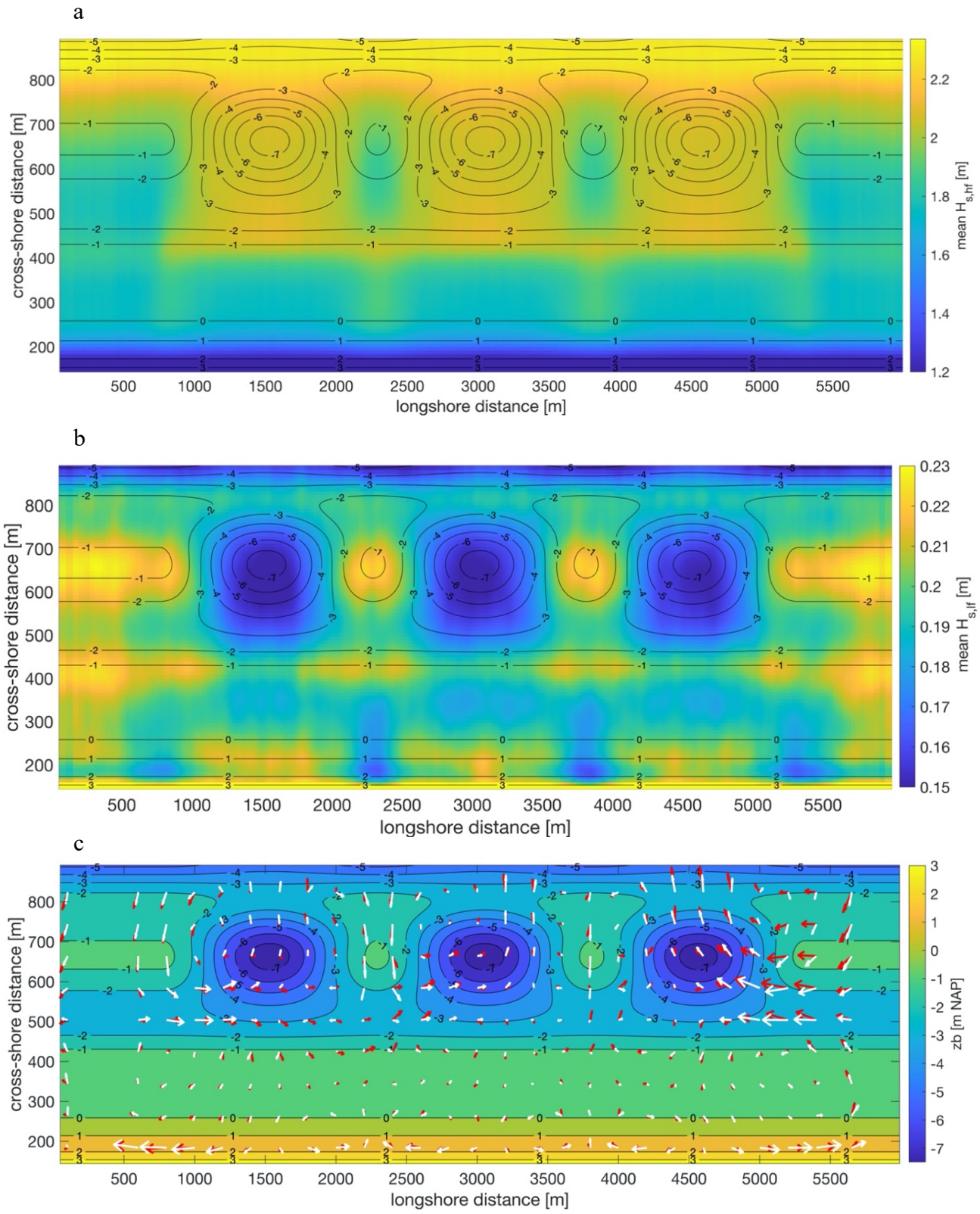

Figure 30: Figure 30a displays the mean significant high frequency wave height of phase SFSaC in the nearshore area. contour lines represent the bed levels in metres NAP. The $\overline{H_{s,hf}}$ eventually becomes zero at the dune foot. Figure 30b displays the mean significant low frequency wave height of phase SFSaC in the nearshore area. Figure 30c indicates the mean current in the nearshore area of SFSaC and SFMaC. The size of the arrows indicates the magnitude of the mean current. The white arrows represent SFMaC, while the red arrows are indicative for the SFSaC mean current.

4.3.2 *SFScC, constant 45 °*

High frequency waves

Under conditions with a constant wave angle of -45°, the high frequency wave energy is distributed over the outer bar under an angle as well. Similar to the multi-dir results (Section 4.1.2) the $\overline{H_{s,hf}}$ is uniform over the seaward face of the outer bar (Figure 37).

Averaged over the beach, the range of variation in $\overline{H_{s,hf}}$ is 3 cm larger and the maximum set-up is 1.5 cm higher for the single-dir results. The location of maxima for both set-up and $\overline{H_{s,hf}}$ are located leftward of the bay positions, while three minima are observed to the right of the bay positions (Appendix 8B.2.3, Figure 64b).

Low frequency waves

Under -45° wave conditions, more low frequency energy seems to be present in the nearshore area using the single-dir method. Values in figure 32b range between 20 and 40 cm, while the results of SFMcC vary between 9 and 17 cm. Apart from the magnitude, the distribution of IG energy in the nearshore area is almost similar in both methods. Between y = 0 and 400 m, broad areas with a relatively high $\overline{H_{s,lf}}$ are visible, centred at x = 1750, 3250 and 4750 m. Although these features are also present in section 4.1.1, the presence of this phenomenon using the single-dir method seems to be more distinct. In figure 31, a large range in extreme values, mentioned above, is also visible in the crest-trough pattern for the 5° intervals. Similar to SFMcC, high values of $\overline{H_{s,lf}}$ occur at the position of bays, while relatively low values are observed at the longshore position of horns. The pattern shifts to the right when the wave angle becomes increasingly negative and a shift to the left occurs under an increasingly positive wave angle. There is significantly less noise on the -10° to 10° interval and the increase in $\overline{H_{s,lf}}$ at the longshore boundaries is less intense compared to the multi-dir results. Similar results are observed under a continuous change in wave angle over time (Appendix 8B.1.3, Figure 60).

The $\overline{H_{s,lf}}$ at the foot of the dune for every 5° interval and both methods are compared in figure 33. It immediately becomes clear that the single-dir method results in overall higher values of $\overline{H_{s,lf}}$. For single-dir results, $\overline{H_{s,lf}}$ is highest under large wave angles and decreases when the angles decrease. For the multi-dir results the opposite trend is visible. At 0° the $\overline{H_{s,lf}}$ is highest and it decreases towards larger angles. The variation of $\overline{H_{s,lf}}$ is also smaller under 0° wave angles. While the minimum values stay roughly the same under every condition for the single-dir results, maximum values increase drastically towards larger wave angles. Values up to 42 centimetres are observed, more than double the maximum values of phase SFMcC.

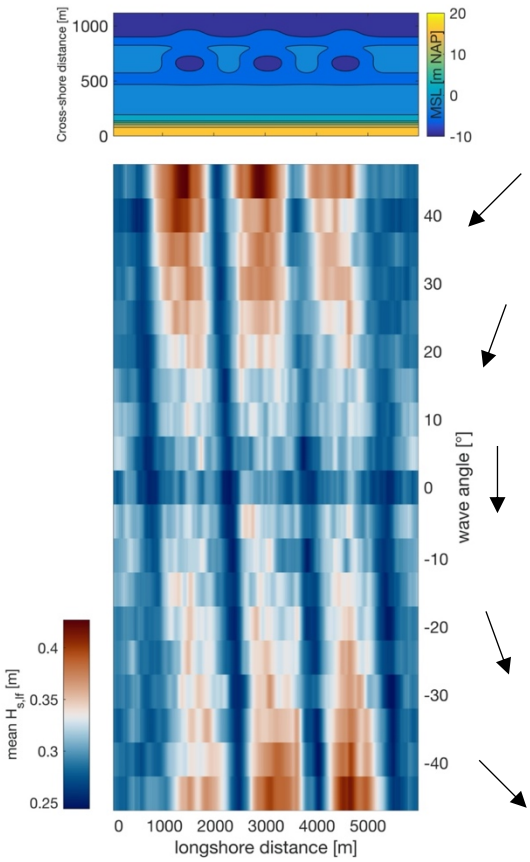

Figure 31: The upper panel figure 31 displays the bathymetry with the location of the horns and bays. The bottom panel shows the mean significant IG wave height at the dune foot, indicated by a colour scale for every 5 ° wave angle interval.

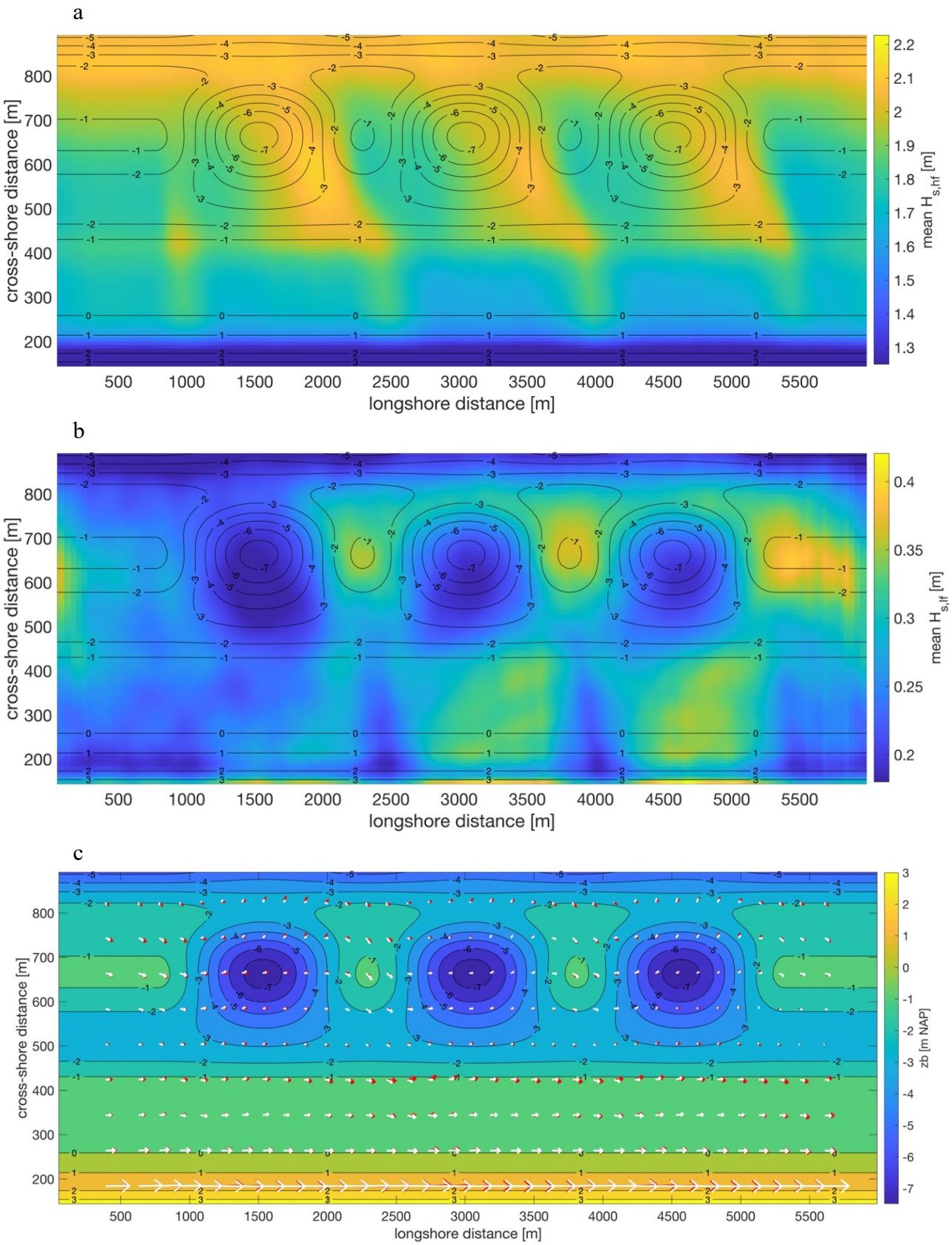

Figure 32: Figure 32a displays the mean significant high frequency wave height of the -45° interval of phase SFMbC in the nearshore area. The contour lines represent the bed levels in metres NAP. The $\overline{H_{s,hf}}$ eventually becomes zero at the dune foot. Figure 32b displays the mean significant low frequency wave height of phase SFSbC in the nearshore area. Figure 32c indicates the mean current in the nearshore area of SFSbC and SFMbC. The size of the arrows indicates the magnitude of the mean current. The white arrows represent SFMbC, while the red arrows are indicative for the SFSbC mean current.

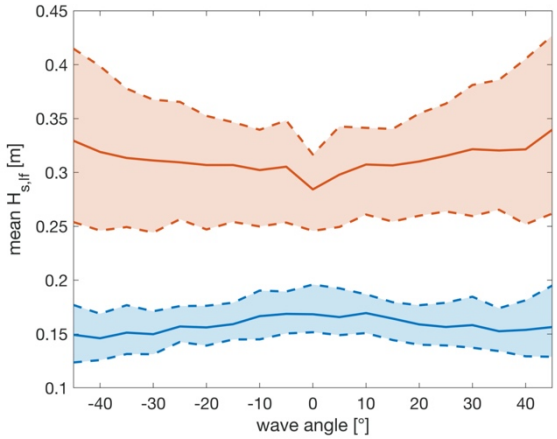

Figure 33: The difference between multi-dir and single-dir longshore statistics for 5° wave angle intervals. Blue and orange represent respectively, the multi-dir and single-dir methods. The solid lines are the mean IG wave heights in the longshore direction at the foot of the dune. The dashed lines indicate the minimum and maximum values.

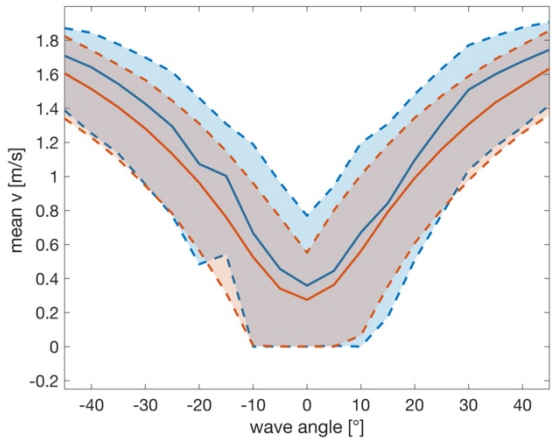

Figure 34: Longshore current at the foot of the dune for multi-dir (blue) and single-dir (orange) methods. The maximum and minimum values are indicated by the dashed lines, while the solid line represents the mean longshore currents. With negative wave angles the longshore current is generally directed towards the north, while for positive angles, a southernly directed current is occurring.

Mean currents

In general, the pattern of the currents in the nearshore are similar for both methods. The current in the nearshore area under -45° conditions, is dominated by a longshore flow (Figure 32c). At the dune foot, the current has a velocity of roughly 1.5 m/s, comparable to the multi-dir results. Averaged over the beach no significant differences in velocity or longshore variation in the mean current are present. The cross-shore component of the mean current is negligible. While the strongest longshore mean current occurs at x = 2200 m and x = 4800 m (Appendix 8B.3.2, Figure 64c).

The rip currents are 0.02 m/s stronger under single-dir conditions. The mean longshore and cross-shore component of the mean current are stronger over the inner bar for the single-dir conditions (Appendix 8B.2.3, Figure 62c). The horn profile in particular has a 0.3 m/s stronger current.

At the foot of the dune, the current for every 5° interval according to the single-dir method (Figure 40) experiences the same trend as the multi-dir current. Both results show an increase in mean longshore current for an increasing wave angle. The single-dir mean current velocities are slightly lower. The current velocity at large wave angles have a value of 1.6 meters per second, which is 0.1 meter slower than the multi-dir at that angle.

4.3.3 *SFSaV & SFScV, low versus high* $H_{s,hf}$

Figure 37 shows that 0° conditions lead to the immediate appearance of the crest-trough pattern at the dune foot after the start of the storm. In the single-dir results, the crests are broader, and the troughs are narrower than in the multi-dir mode. The crest-trough pattern also persists longer than the multi-dir results in the first half of the storm. After 17 hours and a $H_{s,hf}$ of 4.2 metre, the pattern starts to fall apart. In the 20-to-35-hour interval the $\overline{H_{s,lf}}$ increases at the longshore boundaries. The minimum values at the location of the horns start to disappear, but some parts of the crests are still visible. After the peak in $H_{s,hf}$ a high level of longshore variation is still present. The crest-trough pattern for the same values of $H_{s,hf}$ at the end of the storm is not as distinct as the pattern prior to the peak in $H_{s,hf}$.
In figure 37b, under a varying wave angle, a longshore crest-trough pattern also observed immediately after the start of the storm. Its position is slightly to the right of the outer bar morphology, conform the incoming wave angle. The rightmost crest has the highest $\overline{H_{s,lf}}$. After 17 hours, at a significant wave height of 3.9 metres (higher than $H_{s,hf}$ of phase 1 to 4), the crest-trough pattern starts to dissociate and an increase in IG wave height is visible at the longshore boundaries. In the second half of the storm, the crest-trough pattern starts to appear again and although the significant wave height reaches the same values as at the start of the storm, the IG wave height in the crests is higher, while the troughs show lower IG wave heights. Although overall higher $\overline{H_{s,lf}}$ values are observed at the dune foot using the single-dir method, the same response to variation in incoming $H_{s,hf}$ is visible compared to the multi-dir results. It can be assumed that the same processes in the nearshore area are present, as described in section 4.2.
With a time-constant and time-varying $H_{s,hf}$ as well as a time-varying wave angle, the single-dir results show a similar trend as the multi-dir results (Figure 35 & 36). Still, the single-dir method results in significantly higher values of $\overline{H_{s,lf}}$ at the dune foot. For a constant wave angle of 0° the peak in $\overline{H_{s,lf}}$ is roughly 2 hours delayed compared to the peak in incoming $H_{s,hf}$. The variation for the highest values increases as the short-wave height reaches values over 3.8 metres. When the wave angle varies over time the short-wave and IG wave peaks are more in phase (Figure 36) and an increased range in $\overline{H_{s,lf}}$ is observed under larger wave angles. The opposite is true for the multi-dir results: under shore normal wave conditions, the difference between maximum and minimum values is large, while for larger angles this range is slightly smaller.

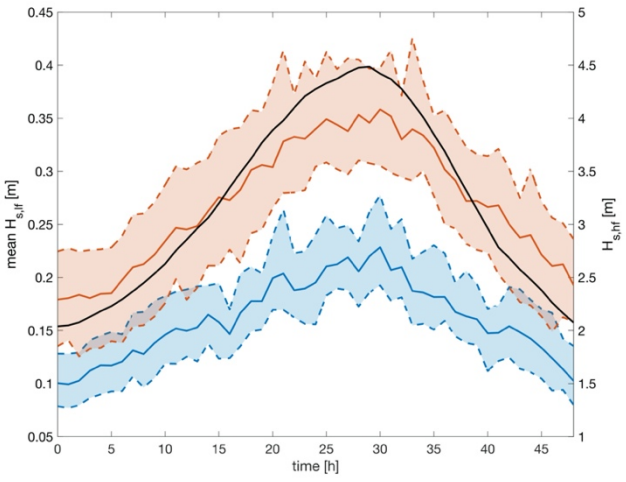

Figure 35: On the left-hand y-axis the $\overline{H_{s,lf}}$ at the dune foot of the multi-dir and single-dir method under 0° wave angle is projected. Blue and orange represent respectively the multi-dir and single-dir methods. The solid, coloured lines are the mean IG wave heights in the longshore direction at the foot of the dune. The dashed lines indicate the minimum and maximum values. The solid black line is the incoming significant wave height as listed in the JONSWAP table, with the corresponding values on the right-hand y-axis.

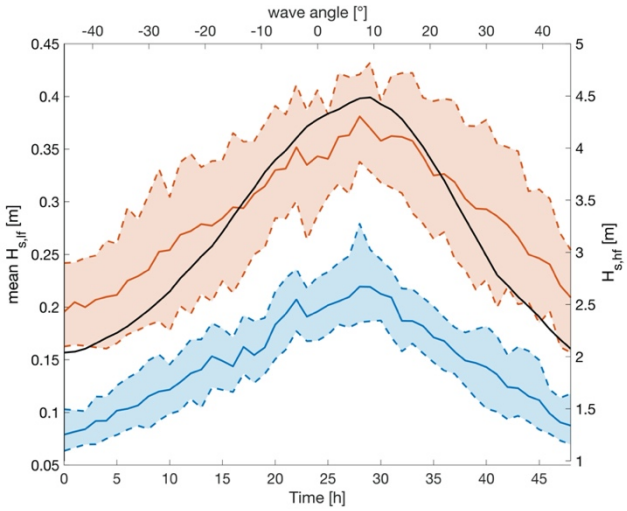

Figure 36: On the left-hand y-axis the $\overline{H_{s,lf}}$ at the dune foot of the multi-dir and single-dir method under a varying wave angle is projected. Blue and orange represent respectively the multi-dir and single-dir methods. The solid, coloured lines are the mean IG wave heights in the longshore direction at the foot of the dune. The dashed lines indicate the minimum and maximum values. The solid black line is the significant wave height as listed in the JONSWAP table, with the corresponding values on the right-hand y-axis. The upper x-axis defines the incoming wave angle.

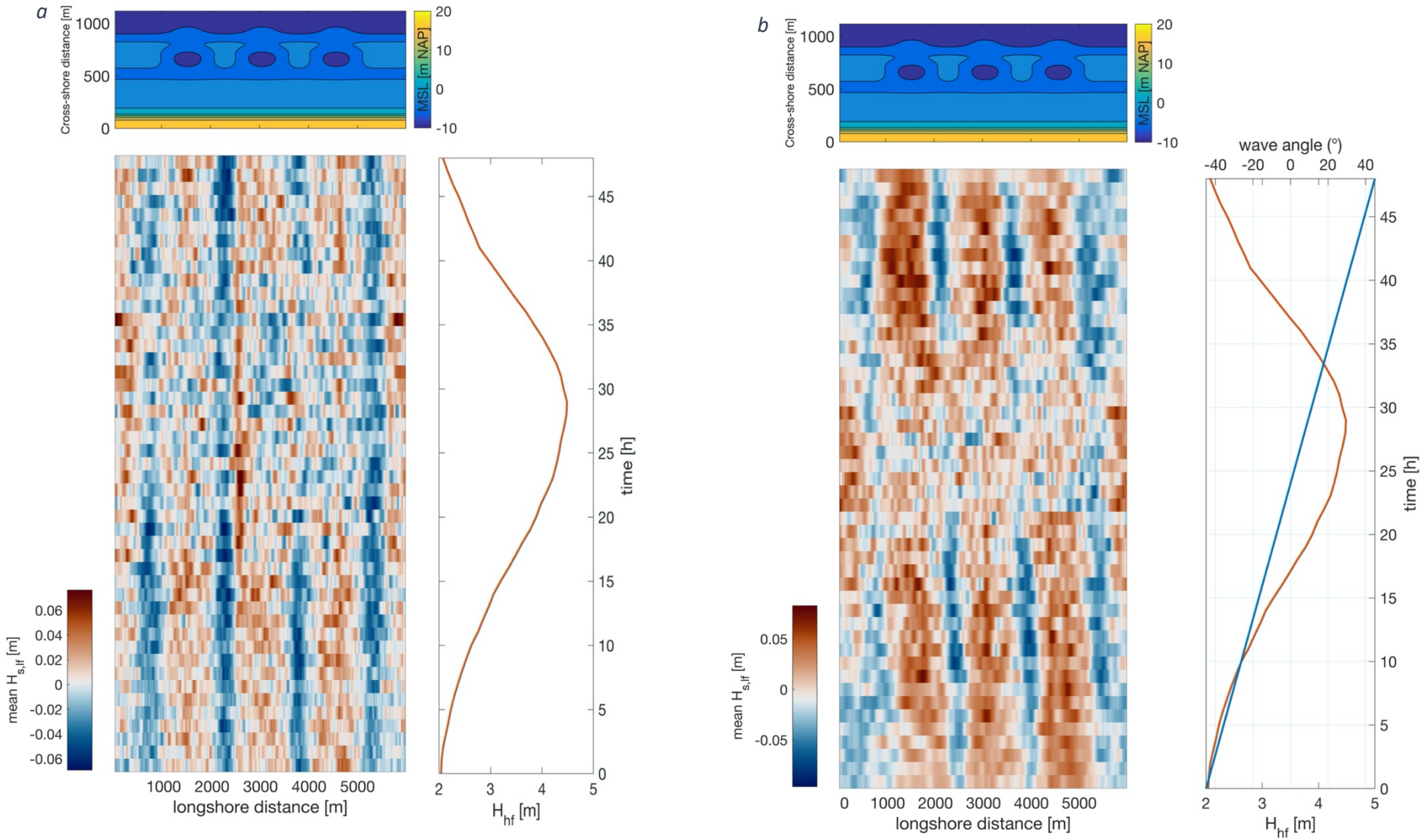

Figure 37: The upper panel in both 37a and 37b displays the bathymetry with the location of the horns and bays. The bottom panels show the normalized significant IG wave height over time, indicated by a colour scale, at the dune foot in the longshore direction. Figure 37a displays the mean significant IG wave height at the dune foot under a 0° wave angle (SFMaV), while in figure 37b the wave angle shifts over time (SFMcV). The panel to the right of both figures, indicates the change in incoming $H_{s,hf}$ over time and in figure 37b also displays the change in wave angle over time (blue line).

4.4 Sediment transport and dune erosion

4.4.1 *reference cases SNMaC & SNMdC*

In this section, the sediment transport is included in the simulations. First, dune erosion under time-constant wave conditions with an incoming angle of 0º and 45º are evaluated as reference cases. Next wave angle is changed to a time-varying parameter and eventually the T_p and H_s will vary over time as well. In section 4.4.1-4.4.3 the multi-dir results are evaluated, while in section 4.4.4-4.4.5 the single-dir results are analysed.
With a constant significant short-wave height and an angle of 0º, the dune front volume decreases quite rapidly after the start of the simulation (Figure 38a). Over time the erosion rate decreases and as the total volume of the dune front declines. Longshore variation in dune erosion is hardly present at the start of the simulation (0-5 hours) but increases over time. The difference in mean eroded volume between locations where erosion reaches a maximum and locations with a minimum amount of erosion reaches a value 5 m^3 per longshore metre (Figure 41).
In figure 38a an overall decline in dune front volume is observed. A variation of the crest-trough pattern seems to occur in phase SNMaC as well. Less loss of mean sediment volume occurs at the longshore locations of the horns, while at the locations of the bays more erosion is observed. The differences in extreme values as depicted in figure 31 are also visible in figure 38. Towards the end some longshore locations have larger volumes left than others. Finally, the dune opposite of the middle bay undergoes less erosion than the right-hand and the left-hand bay.

Under a constant wave angle of 45º, the erosion increases drastically (Figure 38b). After 7 hours of erosion the longshore variation in mean dune front volume starts to become more distinct. Multiple erosion features are visible. An alinement with the bathymetric characteristics of the outer bar is hard to distinguish.
After 22 hours avalanching starts to occur at three locations (Figure 38b, dotted line). These locations are slightly to the right of the horn positions and at the left-hand uniform outer bar. These erosional events are followed by an increase in mean dune front volume to the right of the avalanche locations. The dune front volume increases most at the location of the uniform left-hand outer bar. After 30 hours no more avalanching effects take place. Although three locations with a higher dune front volume seem to persist, the longshore distribution of dune front volume is moving towards a more uniform state. At the end of the simulation, the mean volume of the dune front is 590 m^3 per longshore meter. The impact of a 45º wave angle compared to 0º conditions is significantly larger, with 32 m^3 more loss of mean dune front volume per longshore metre.

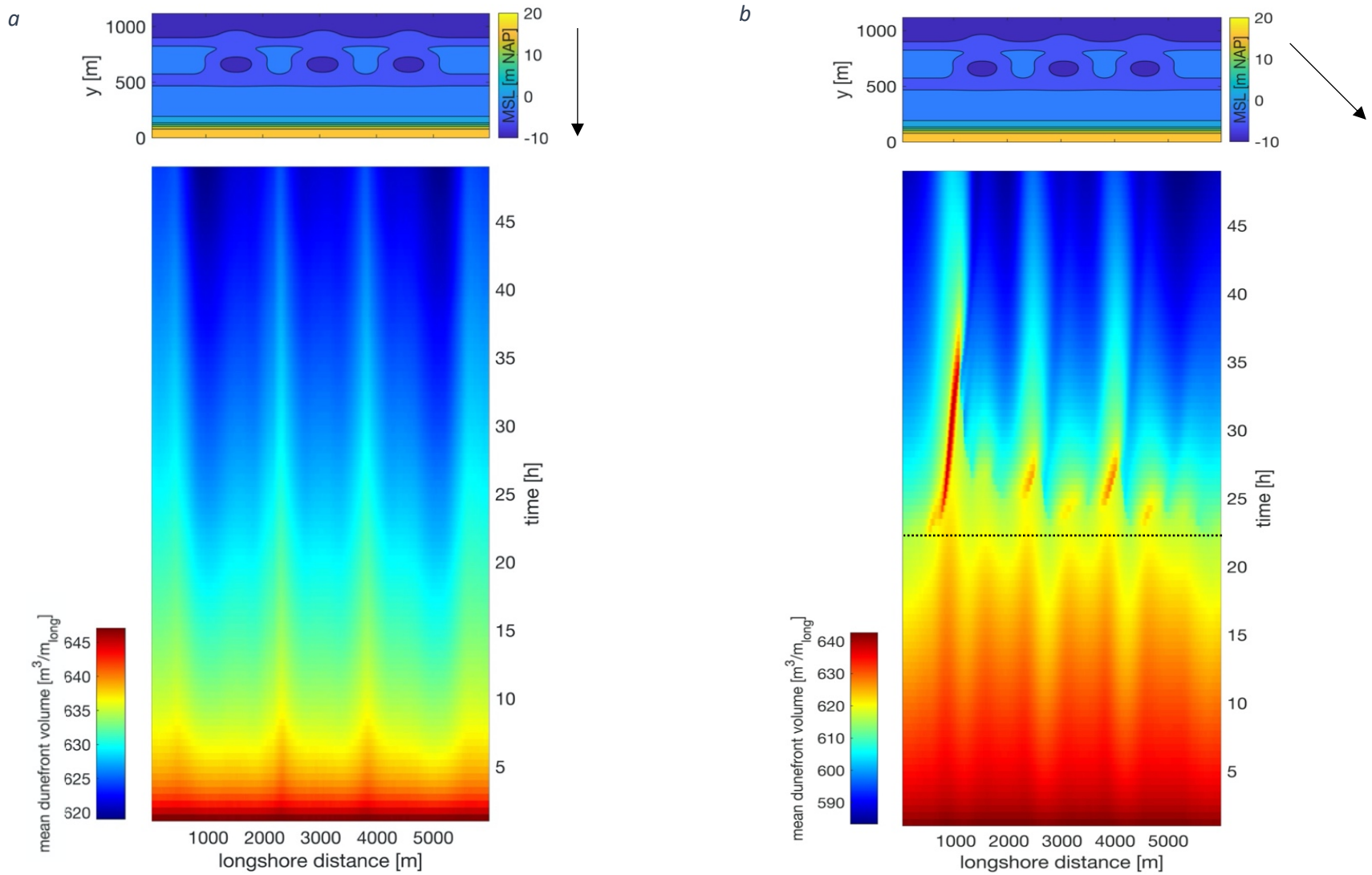

Figure 38: The upper panels in figure 38a and 38b display the bathymetry with the location of the horns and bays for respectively SNMaC and SNMdC. The arrows indicate the incoming wave angles. The bottom panels show the volume of the dune front per longshore meter over time. The dotted line in figure 38b indicates the start of an avalanching sequence. Note: the colour-scales in figure 38a and 38b are different.

4.4.2 *Wave angle effect*

SNMbC

For every 5° interval the longshore component of the mean sediment transport at the dune foot during 5 hours of constant conditions is depicted in figure 39a. As the wave angle moves through the 0° point the longshore direction of the transport changes. Under negative angles $\overline{q_{long}}$ is directed to the right, while for a positive wave angle, $\overline{q_{long}}$ is directed to the left of figure 39a. The mean longshore sediment transport is largest under large wave angles. It decreases strongly towards smaller angles, with the lowest volumes of longshore erosion being observed around 0°. Under a -45° wave angle, the lowest longshore sediment transport is observed at positions left of the bays. High mean longshore sediment transport is observed at location slightly left of the horns and on positions where the outer bar is uniform. When the waves arrive from the opposite direction (45°), the positions of maxima and minima change. The lowest values are observed to the right of the bay positions, while high values of $\overline{q_{long}}$ are now observed at the right of the horns and on positions where the outer bar is uniform.

The mean cross-shore component of sediment transport ($\overline{q_{cross}}$) is an order of magnitude smaller than $\overline{q_{long}}$ at the dune foot (Figure 39b). As negative values in figure 39b indicate an offshore oriented sediment transport, it becomes clear that small wave angles lead to smaller (less negative) offshore directed sediment transport. At 0°, the lowest $\overline{q_{cross}}$ is observed at the positions of bays, while the largest occur at positions where the outer bar has a horn. Locations where the outer bar is uniform are roughly in between bay and horn values. With increasing wave angle, the position of minima and maxima shift. For -45° low values of $\overline{q_{cross}}$ are observed slightly left of bay positions, while for a 45° wave angle minima are observed slightly right of the bay positions. Maximum values occur at positions where the outer bar consist of a horn or is uniform.

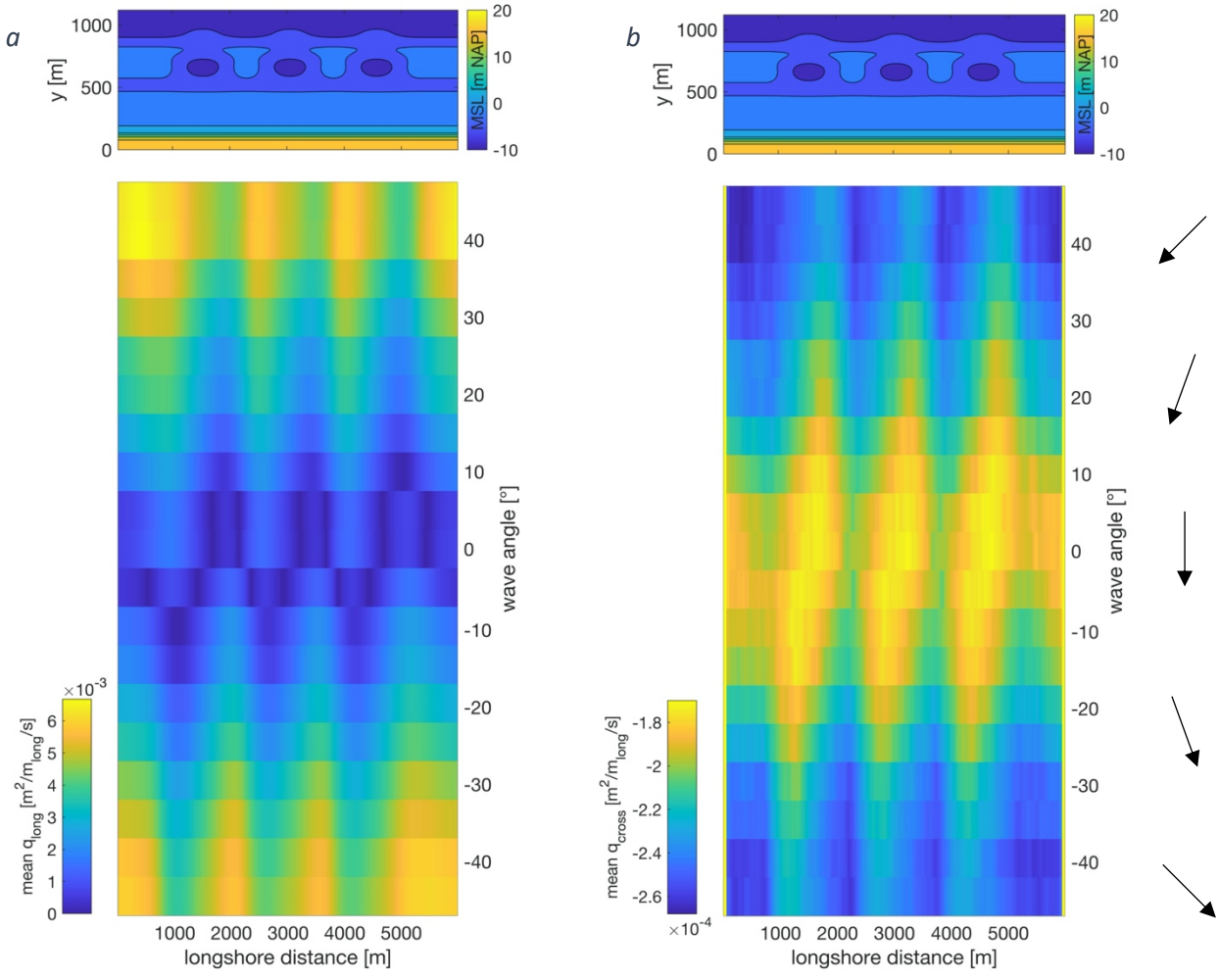

Figure 39: The upper panel in both 39a and 39b displays the bathymetry with the location of the horns and bays. Figure 39a shows the mean longshore sediment transport per metre per second in the longshore dimension at 5° intervals. Figure 39b represents the cross-shore component of sediment transport for every 5° interval.

SNMcC

Figure 40 shows that as a result of a time-varying wave angle, the total mean erosion increases. Where in section 4.4.1 the mean volume of the dune front at the end of the simulation is 621.8 m^3 per longshore metre, the volume left due to the variation in wave angles is 601.4 m^3. For the first 30 hours the eroded volume diminishingly decreases.

In figure 40 the locations with the most erosion in the first half of the storm are slightly to the right of the outer bar bays. The locations of the left-hand uniform bar and the horns experience less erosion, with the former having the least loss of volume. After 22 hours, under a 0° wave angle (Figure 40, bottom dotted line), the start of an erosional hotspot as a result of slumping becomes visible at the location of the right-hand bay. This is even better visible in an animation[4] of the bed levels over time. At 33 hours and a wave angle of 17° (Figure 40, middle dotted line) another, narrower hotspot starts to develop at the location of the left-hand bay. 42 hours into the storm an overall decrease in volume occurs without slumping (Figure 40, top dotted line). This coincides with a large wave angle and a strong decrease in longshore variability of the mean dune front volume.

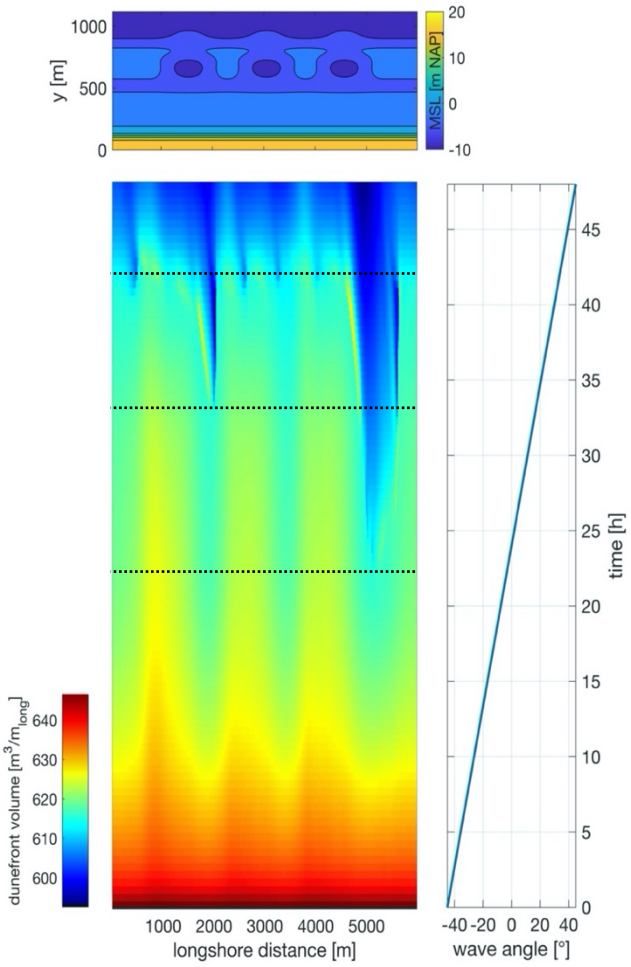

Figure 40: The upper panel displays the bathymetry with the location of the horns and bays. The bottom panel show the volume of the mean dune front per longshore metre over time for phase SNMcC. The right-hand panel indicates the change in incoming wave angle over time. The dotted lines refer to specific phenomena described in the text.

[4] https://youtu.be/ZOtnsZq64WI

4.4.3 *Wave height effect*

SNMaV

In figure 43a it can be observed that, when a time-varying significant wave height is added to the storm conditions, not only the erosion in the first 15 hours occurs at a slower rate, but also a less distinct crest-trough pattern is observed. At 20 to 25 hours into the storm, the erosion starts to set in on the locations of the right-hand side, the left-hand side and the middle bay (in this order). Less erosion occurs at the locations of the two horns (x = 2300 and 3800 m) and the uniform parts of the outer bar (x = 1000 and 5000 m). The latter experiences even less erosion than the former. At the end of the storm, the dune front at the right-hand bay has the largest loss of volume, followed by the left-hand bay.
Overall, a smaller decrease in dune front volume is present in the first 30 hours of the simulation, compared with the results under a time-constant wave height (Figure 41). After 30 hours the erosion seems to accelerate slightly as H_s increases. The end result is a similar mean dune volume of 622 m^3/m. The difference between maximum and minimum erosion values increases over time. The largest difference is therefore 6.23 m^3/m at the end of the storm.

SNMcV

In this section the storm conditions vary in wave angle, H_s and T_p. The longshore distribution of dune front volume (Figure 43b) shows that after less than 7 hours an increasing longshore variability is present. Subsequently, this variability hardly increases, but the mean dune volume still decreases. After 35 hours, large avalanching events occur at x = 5500, 4200, 2500 and 800 m. At the leeward side of the incoming wave angle, these locations endure sudden sedimentation.
As in phase SNMaV, the first 27 hours of the storm a diminishing decrease in mean dune front volume is visible (Figure 42). Under time-varying wave height the decrease diminishes stronger.
Subsequently, the erosion slowly starts to increase again after the peak in H_{rms}. After 30 hours the minimum value decreases drastically, followed by an increase in maximum value after 35 hours. In the last ten hours of the storm, the maximum and the minimum value decrease slowly. At the end of the storm a mean dune front volume of 610 m^3/m is left. This is 9 m^3/m less mean dune erosion than under a time-constant wave height. With a time-varying wave height the difference between the minimum and maximum value is 9 m^3/m more than under a time-constant wave height. Therefore, it can be assumed that at the end of the storm more longshore variability is observed in the case of a time-varying wave height.

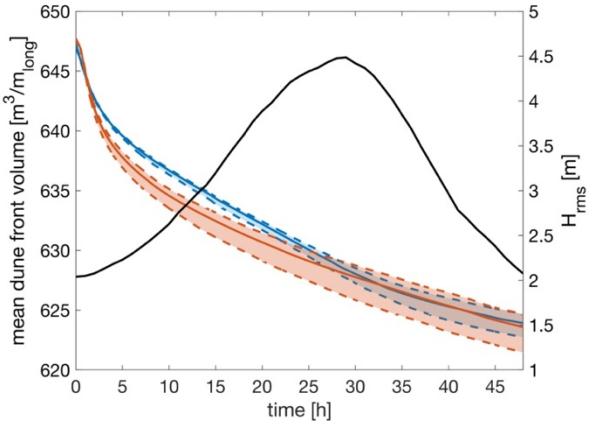

Figure 41: Mean volume of the dune front over time per longshore metre. Blue and orange represent respectively a time-varying H_{rms} (SNMaV) and a time-constant H_{rms} (SNMaC). The solid, coloured lines are the mean dune front volumes per longshore metre. The dashed lines indicate the minimum and maximum values.

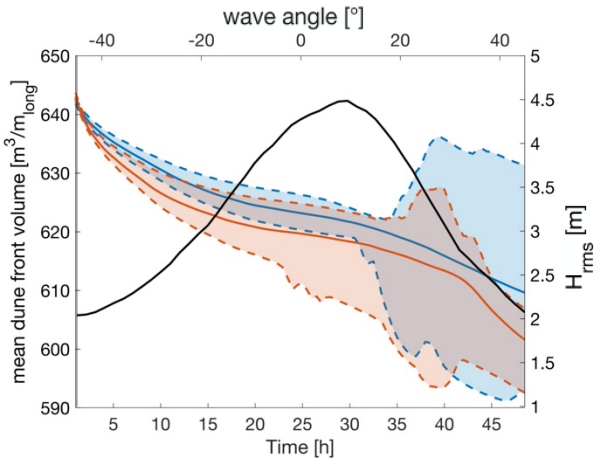

Figure 42: Mean volume of the dune front over time per longshore metre. Blue and orange represent respectively a time-varying H_{rms} (SNMcV) and a time-constant H_{rms} (SNMcC). The solid, coloured lines are the mean dune front volumes per longshore metre. The dashed lines indicate the minimum and maximum values. The upper x-axis indicates the wave angle over time.

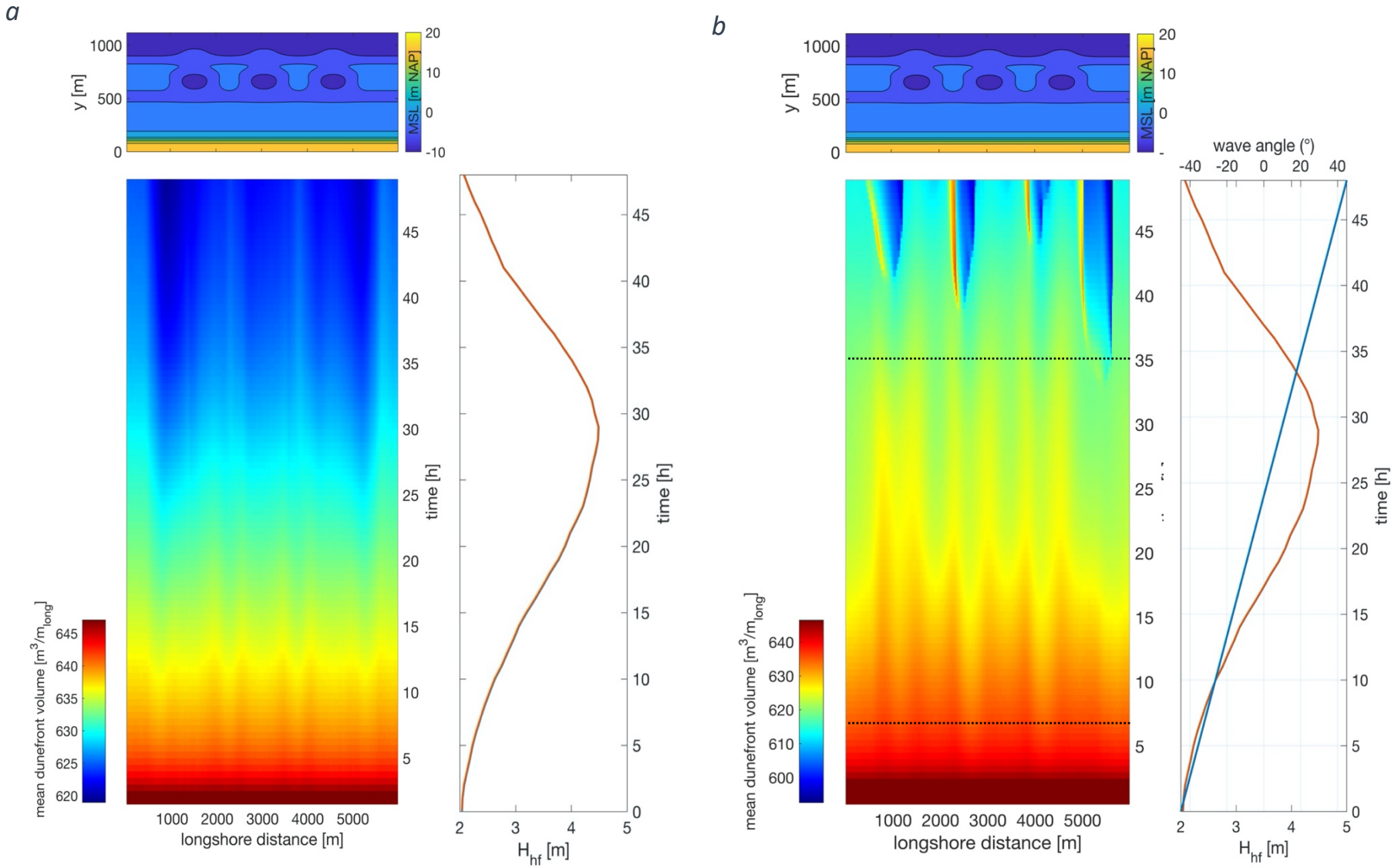

Figure 43: The upper panel in both 43a and 43b displays the bathymetry with the location of the horns and bays. The bottom panels show the mean volume of the dune front per longshore metre over time for respectively phase SNMaV and SNMcV. *The right-hand panel in figure 43a displays the H_s. The right-hand panel in figure 43b includes the wave angle. Dotted lines indicate specific moments in time described in the text.*

4.5 Single-dir effect on sediment transport

4.5.1 *reference cases*

SNSaC

Under constant 0° conditions, the single-dir calculations of phase SNSaC also show a declining volume of the dune front (Figure 44). There is no significant difference between the mean dune front volume of the single-dir and multi-dir method. The results at the end of the storm are therefor, in terms of dune front volume, comparable.

In figure 66 (Appendix 8B.4.1), the situation seems less similar. For the single-dir method, the locations with less erosion consist, of two features. These two locations do coincide with the horns of the outer bar. Where the outer bar is uniform, less erosion is observed as well. The locations with relatively large erosion correspond to the bays in the outer bar, with even more erosion at locations of the left-hand and right-hand bay. In a bed level animation[5], it becomes clear that the longshore variability in mean dune volume is low.

SNSdC

In figure 46, the distribution of the mean dune front volume over time is depicted, under a constant 45° wave angle. The results are significantly different compared with the 0° conditions. After 10 hours (figure 46, bottom dotted line) longshore variation increases, with locations of low erosion at the bay positions[6]. To the left of these positions, the largest erosion occurs. After 18 hours avalanching occurs at multiple locations, followed by an increase in dune front volume to the right of these locations. After 30 hours the variation starts to decrease (Figure 45). At the end of the storm, less loss in dune front volume is observed at the bay positions, while the horns and the rightmost uniform bar have endured more loss of sediment.

From the comparison of the results of both methods in figure 45, it becomes clear that the avalanching occurs 4 hours earlier using the single-dir method. The difference between maximum and minimum values during the avalanching seems 6 m^3/m larger, so does the decrease in mean dune front volume. At the end of the simulation the difference in mean dune front volume is relatively small. The single-dir method has 2 m^3/m more loss than the multi-dir option.

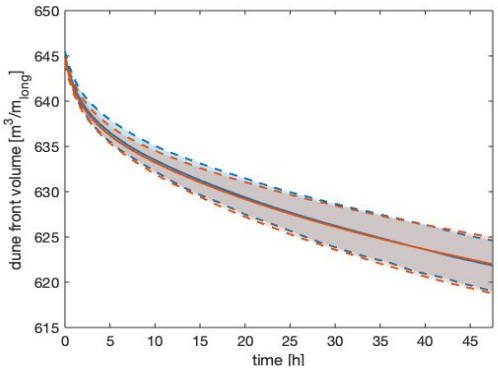

Figure 44: Volume of the mean dune front over time per longshore metre under a 0° wave angle. Blue and orange represent respectively the multi-dir and single-dir methods. The solid, coloured lines are the mean dune front volumes averaged over the longshore dimension. The dashed lines indicate the minimum and maximum values.

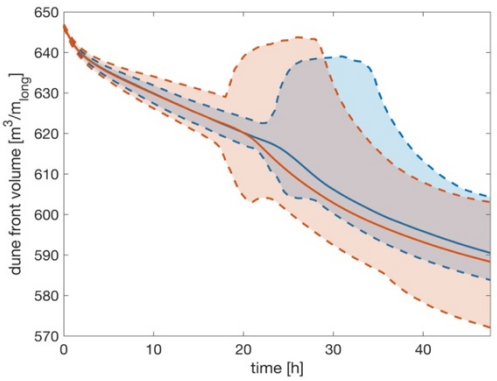

Figure 45: Volume of the mean dune front over time per longshore metre under a 45° wave angle. Blue and orange represent respectively the multi-dir and single-dir methods. The solid, coloured lines are the mean dune front volumes averaged over the longshore dimension. The dashed lines indicate the minimum and maximum values.

[5] https://youtu.be/PqLnE6ZnG6E
[6] https://youtu.be/0Ha7qNb6em8

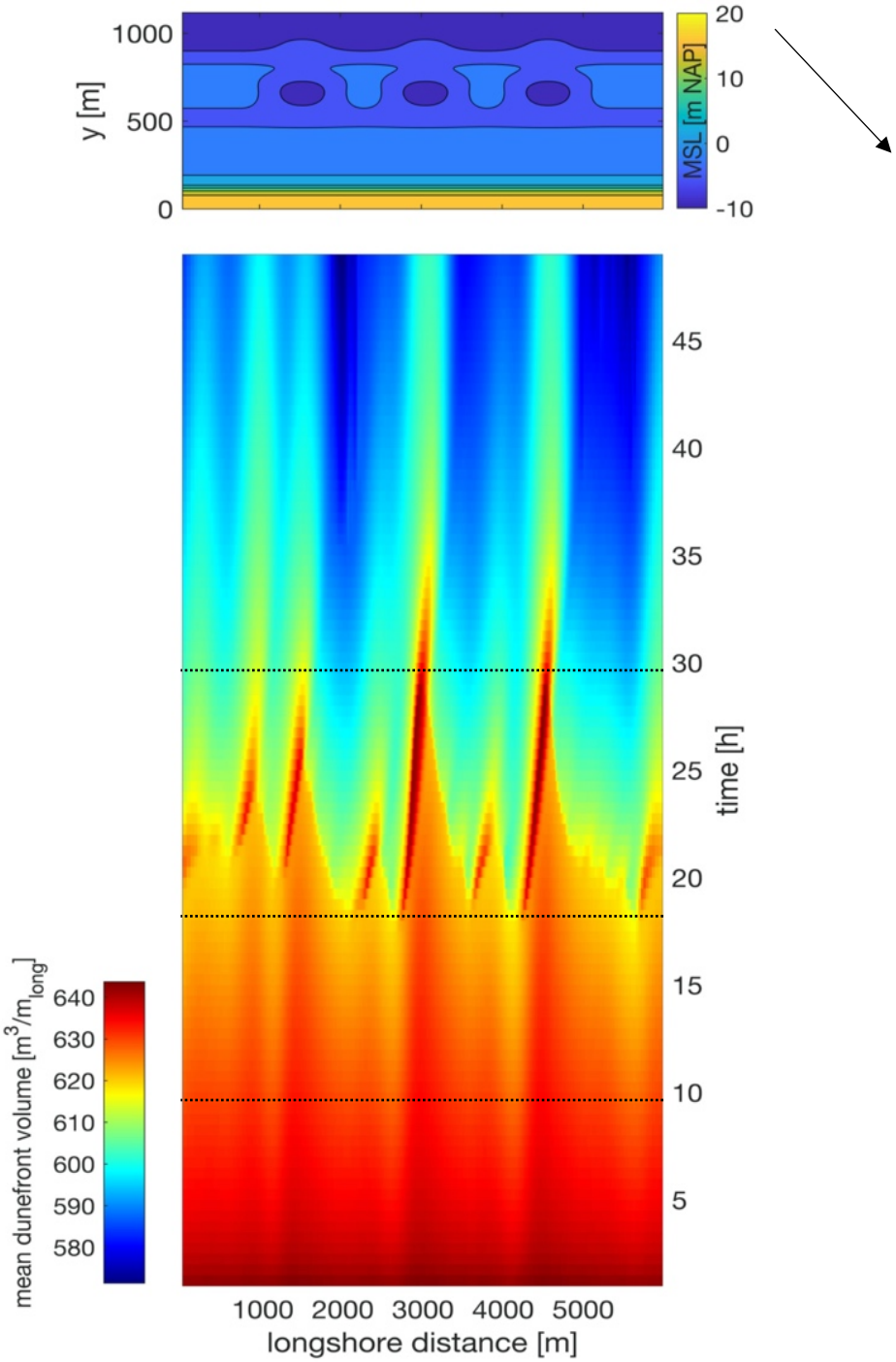

Figure 46: The upper panels in figure 46 display the bathymetry with the location of the horns and bays. The bottom panels show the mean volume of the dune front per longshore meter over time. In figure 46 the wave angle is a constant -45°.

4.5.2 *Wave angle effect*

SNSbC

The longshore distribution of the mean sediment transport using the single-dir method (Appendix 8B.4.2, Figure 67), is comparable to the multi-dir results strongest longshore mean sediment transport is observed at locations with a horn and a uniform outer bar. Relatively low mean sediment transport is observed on bay positions.

Under relatively short storm conditions, the multi-dir and single-dir results are not very different. The mean eroded sediment volume of phase SNSbC is overall a bit larger than SNMbC. At -45° and 45° the eroded volume is only 0.34 and 0.41 m^3 more, while at 0° the difference is only 0.14 m^3 (Figure 48).

In the results of the longshore current (Figure 48), the resemblances between phase SNMbC and SNSbC are clearly visible. The differences, however, are opposite compared to what we see in the eroded sediment volume. The $\bar{v}$ is lower for each wave angle under single-dir conditions. For the interval -5° to 5° the single-dir current decreases more than the multi-dir current, eventually reaching only 0.25 meters per second. The difference between extreme values increases from 0.31 and 0.4 meters per second at -45° and 45°, towards 0.55 m/s at 0°. Most of the values of the single-dir v fall within the range of the multi-dir results, with a small exception around 30° and -30° angles

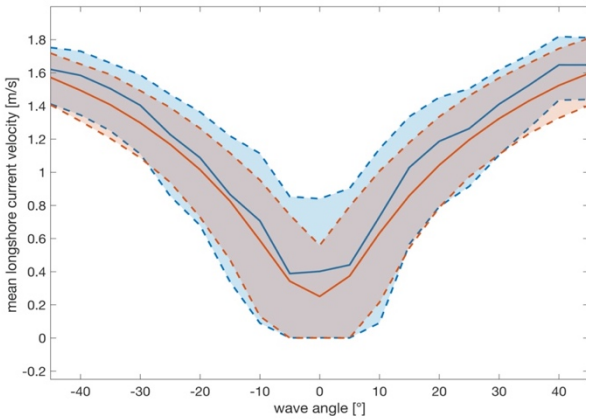

Figure 47: Longshore mean current velocity for every 5° interval. Blue and orange represent respectively the multi-dir and single-dir methods. The solid, coloured lines are the mean longshore current velocities. The dashed lines indicate the minimum and maximum values. Note that these values are absolute. This means that in the transition from a negative to positive wave angle, the longshore current changes direction.

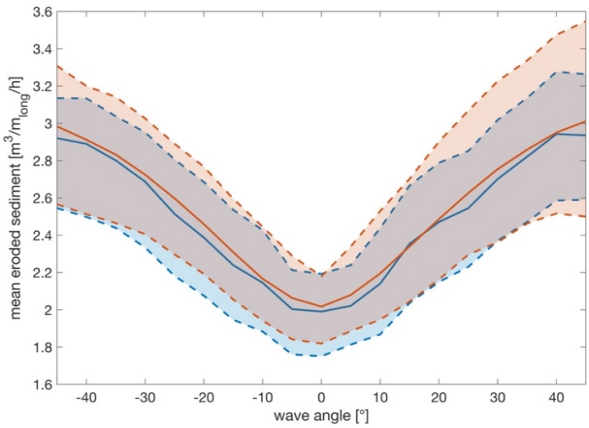

Figure 48: Longshore statistics of mean eroded sediment volume per longshore meter for every 5° interval. Blue and orange represent respectively the multi-dir (SNMbC) and single-dir methods (SNSbC). The solid, coloured lines are the mean volumes of sediment erosion per longshore metre. The dashed lines indicate the minimum and maximum values

SNScC

In figure 49 the mean dune volume for time-varying wave angle is plotted. It becomes clear that less erosion develops to the right of the outer bar horns and the left-hand uniform outer bar. Secondary longshore locations with low erosion are visible on the left and middle horn locations. The first large erosion feature after 15 hours, appears at the left-hand bay and is superseded shortly on the locations of the other bays. At the end of the storm most sediment has been eroded at the left-hand bay. Although the wave angle moved from -45° to 45°, the erosional hotspots still are positioned to the left of the bays. At the end of the storm even some secondary erosion features occur.

Between 15 and 30 hours avalanching occurs, resulting in a small strip with an increase in dune front volume on the right-hand side of the secondary low erosion features. These small strips are also visible on the left-hand side of the primary low erosion features at x = 3100 and 4600 m during the 30 to 40 hours' time interval. This coincides with a stronger longshore mean sediment transport.

From the animation it becomes clear that the eroded sediment from the dune front is redistributed in the longshore direction as the wave angles becomes larger, leading to relatively uniform bed levels. This is also visible in figure 48, where at the end of the storm the difference between minimum and maximum values decreases drastically.
The mean dune front volume using the single-dir method results in comparable values as the multi-dir method in the first 18 hours (Figure 48). From this point in time the multi-dir mean erosion rate decreases, compared to the single-dir erosion rate. This results in a relatively continuous decline in dune front volume for the single-dir case. At the end of the storm the mean dune front volume of phase SNScC is lower than in phase SNMcC, indicating an overall higher mean erosion of 4.15 m^3/m. The minimum dune front volume shows a diminishing decrease over the first 15 hours, after which a steep decrease occurs. This erosion event is visible in the animation[7] of bed levels during the storm and occurs significantly earlier than under multi-dir conditions. After 17 hours the mean maximum dune front volume increases, indicating sedimentation. The maximum dune volume increases even further after 28 hours at a 10° wave angle, until it steeply decreases after 38 hours. After 29 hours the minimum dune front volume decreases even further until at 35-hour sedimentation takes place, leading to an increase in the minimum values, followed by a decrease until the end of the storm.

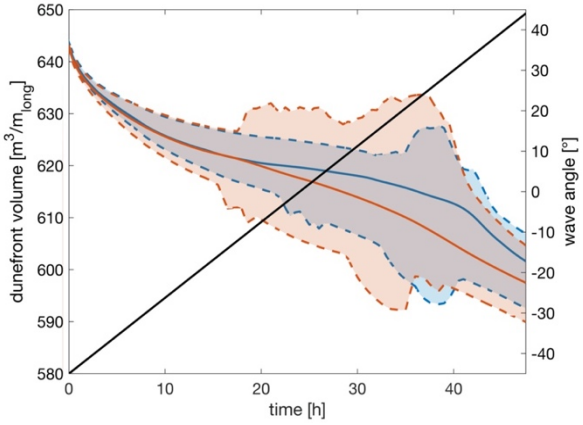

Figure 48: Volume of the dune front over time per longshore metre. Blue and orange represent respectively the multi-dir and single-dir methods. The solid, coloured lines are the mean dune front volumes averaged over the longshore dimension. The dashed lines indicate the minimum and maximum values. The black solid line

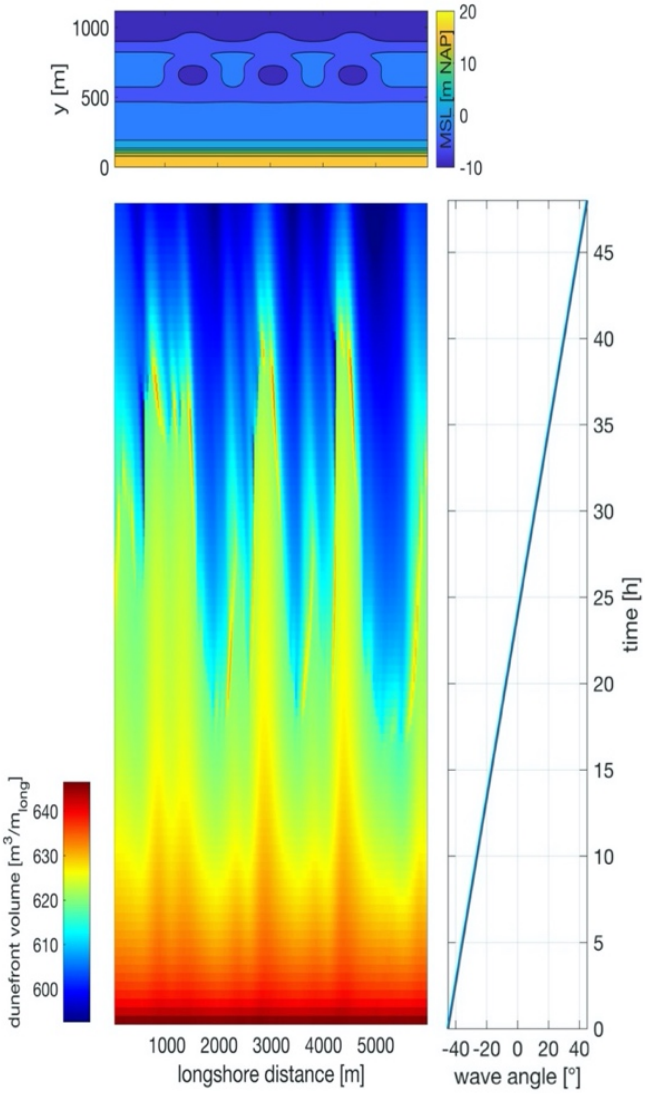

Figure 49: The upper panel displays the bathymetry with the location of the horns and bays. The bottom panels show the volume of the mean dune front per longshore meter over time. The right-hand panel indicates the angle of the incoming waves over time.

[7] https://youtu.be/ypY-_XA76u4

4.5.3 *Wave height effect*

SNSaV

Similar to the comparisons under 0° wave conditions of phase SNMaC and SNMaV, the results of the longshore statistics using the multi-dir or single-dir method hardly deviate when H_{rms} changes over time (Figure 50). There are some small differences in extreme values, but these seem insignificant. In figure 68 (Appendix 8B.4.3) the longshore variation in dune front volume is different from the multi-dir results. Secondary features similar to those described in 4.5.1 are present in the single-dir results, while the multi-dir results show a crest-trough pattern with only primary features conform the outer bar. After 5 hours it becomes clear that there is more erosion at the locations of the outer bar bays. At the outer bar horns, two features with low erosion rates for every horn are visible. For a uniform outer bar less erosion is observed as well, persisting longer than the features at the horns. The two outer bays endure more erosion compared to the inner bay, with the left-hand bay losing the most volume. In short, the difference in mean dune erosion between time-constant and time-varying wave height using the single-dir method is nihil.

SNScV

In the longshore distribution of dune front volume over time, locations to the right of the horns (x = 3000 and 4500 m) and uniform outer bar show relatively low magnitudes of erosion (Figure 52). The left-hand boundary and the locations to the right of the bays (x = 2100 and 3100 m) experience relatively more erosion. Between 25 and 35 hours these areas of high erosion, endure even more loss of dune front volume. Subsequently, sedimentation takes place after 30 hours (Figure 52, dotted line), resulting in the persistence of three crests towards the end of the storm.

Averaged over the longshore dimension the mean dune front volume of the single-dir method runs parallel to the multi-dur results (Figure 51). The dune front volume of phase SNScV is slightly lower, and the extreme values diverge more. After 23 hours, shortly before the peak of the storm, a stronger declination in dune front volume is observed for the single-dir method, which lasts until the end of the storm.

The end result is a mean dune front volume of 599 m^3/m. The minimum dune front volume experiences an increase in erosion rate at 22 hours and a 5° wave angle. With some minor variations this continues in the second half of the storm. An increase in maximum values is also present and starts after 27 hours. A steep decrease of the maximum value occurs at the end of the storm. The erosion events seem to occur significantly earlier in time in the single-dir results compared to the multi-dir method (Figure 51).

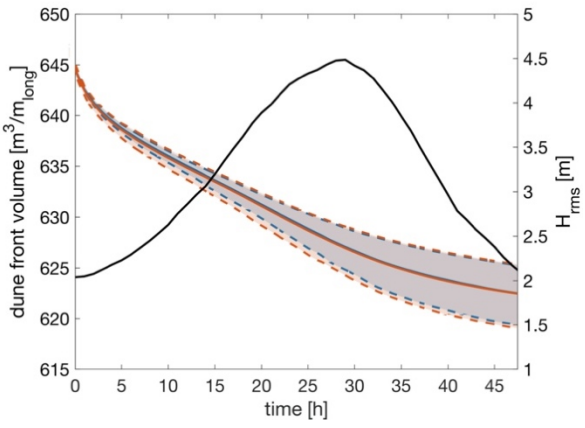

Figure 50: Mean volume of the dune front over time per longshore metre. Blue and orange represent respectively the multi-dir and single-dir methods. The solid, coloured lines are the mean dune front volumes averaged over the longshore dimension. The dashed lines indicate the minimum and maximum values. The black solid line is the incoming H_{rms} over time.

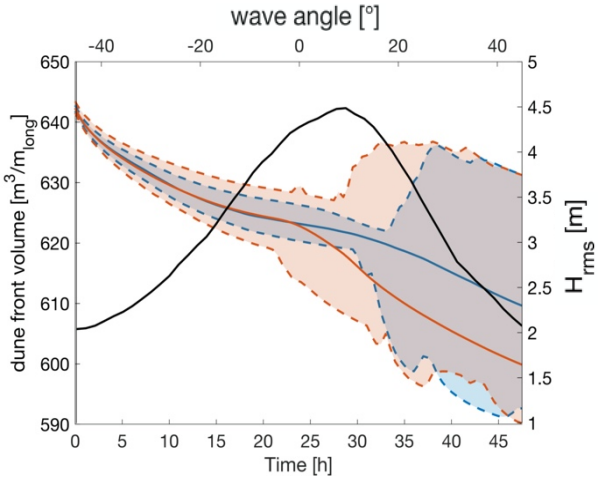

Figure 51: Mean volume of the dune front over time per longshore metre. Blue and orange represent respectively the multi-dir and single-dir methods. The solid, coloured lines are the mean dune front volumes averaged over the longshore dimension. The dashed lines indicate the minimum and maximum values. The black solid line is the incoming H_{rms} over time. The upper x-axis represents the boundary condition of the incoming wave field.

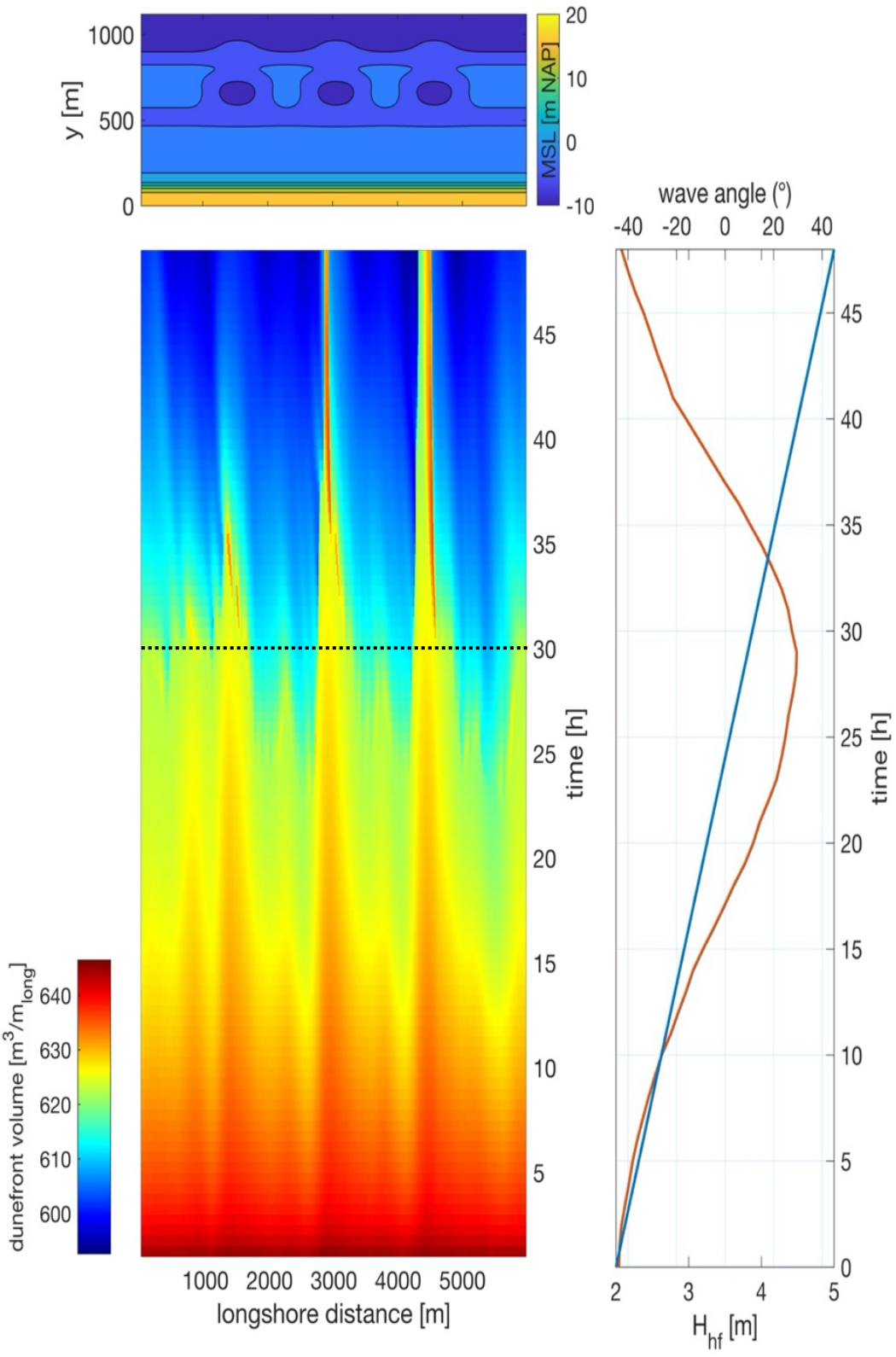

Figure 52: The upper panel in figure 52 displays the bathymetry with the location of the horns and bays for SNScV. The bottom panels show the mean volume of the dune front per longshore metre over time. The right-hand panel in displays the H_{rms} and the wave angle.

4.5.4 Overview

In table 5 an overview of the sediment dune front volumes at the end of the simulations is listed. Under wave conditions where the wave angle is 0º, the end results of the two methods do not seem to differ much in sheer volume. The longshore distribution using the single-dir option leads to more longshore variable dune erosion, but the absolute difference of the extreme values as a result of the methods and the variation in H_{rms} is not larger than 1 m^3/m.
When considering a larger wave angle, the dissimilarities between the methods becomes clear. The end results of the single-dir method show a substantial 11 m^3/m more eroded dune front volume than the multi-dir method under a varying wave angle. For a constant wave angle of -45º the difference of the mean dune front volume is relatively small, but the variation between extreme values is relatively large.
The contrast between the maximum and minimum values is similar under a constant H_{rms} for both methods. When variation in H_{rms} is added, the single-dir dune front volume has 3 m^3/m less difference between its minimum and maximum values. The position of erosional hotspots is comparable in both methods.
Under a 0º positions with an increased loss in mean dune front volume are present at the locations of bays. Under varying wave angle, the location of the maximum loss of dune front volume shifts slightly to the left, while less sediment is eroded on longshore positions left of the horns and where the outer bar is uniform. Avalanching events occur earlier using the single-dir method, this becomes clear under larger wave angles where erosion in the collision regime is enough to initiate the avalanching. The position of avalanching does not differ significantly between the single-dir and multi-dir method.

		0º		**-45º to 45º**			**-45º**		
		Mean	**Max-Min**	**Mean**	**Max-Min**	**T_{start} avalanche**	**Mean**	**Max-Min**	**T_{start} avalanche**
Multi-dir	**Constant H_s**	622	5.58	601	14.33	24 h	590	20.44	22 h
	Varying H_s	622	6.23	610	34	46 h	X	X	X
Single-dir	**Constant H_s**	619	6.19	590	14.71	16 h	588	31.46	19 h
	Varying H_s	622	6.53	599	31	24 h	X	C	X

Table 5: The dune front volumes in cubic metres per longshore metre left after the storm simulations. It includes the total volumes as well as the difference between the minimum and maximum dune front volumes. The start time of avalanching events is given in hours. No simulations for a time-varying H_s and a constant wave angle of -45º are explored. Therefore, they are marked with an 'X'.

5. Discussion

5.1 Hydrodynamic conditions

5.1.1 Summary

Under 0° conditions the impact of the crescentic bars on the hydrodynamic conditions in the nearshore area is similar to the rhythmic bar and beach state described by Wright et al. (1984). Rip currents occur at the embayments in the outer bar and circulation patterns are observed over the inner bar and the beach (Section 4.1.1). Due to depth induced breaking, $\overline{H_{s,hf}}$ patterns follow the bathymetry and become zero at the dune foot. The $\overline{H_{s,lf}}$ increases over the beach, but no longshore pattern conform the outer bar morphology is observed at the dune foot. As a result of a time-constant -45° wave angle, a crest-trough pattern in longshore distribution of $\overline{H_{s,lf}}$ occurs at dune foot. The mean currents change from a cell-circulation pattern under 0° to a longshore dominated current with meandering over the outer bar. With a time-varying wave angle it becomes clear that with a smaller wave angle the crest-trough pattern at the dune foot disappears.
With a time-varying H_s and T_p (Section 4.2) the dissipation of $\overline{H_{s,hf}}$ energy due to breaking changes, but still moves to zero towards the dune foot. Remarkedly, the crest-trough pattern in $\overline{H_{s,lf}}$ at the dune foot is present under a H_s below 3.1 m, while for larger H_s values the pattern disappears. Under a 0° wave angle the magnitude of the mean currents change conform the time-varying H_s. The circulation cells are different depending on the H_s, under low conditions the beach is characterized by an onshore mean current at horn positions (x = 2300 and 3800 m), while for higher values of H_s the mean current is offshore directed. Considering the constant storm surge of 4 m, it is noticeable that the outer bar morphology still has a large impact on the hydrodynamic processes in the near-shore area.
Applying the single-dir method (Section 4.3), the $\overline{H_{s,hf}}$ is up to 0.4 m lower in the nearshore area (Figure 53), while the $\overline{H_{s,lf}}$ is higher as implied by the XBeach adjustments of Roelvink et al. (2018). The largest difference is the between the single-dir and multi-dir method is the $H_{s,lf}$ at the dune foot. The single-dir method is double the height compared to the multi-dir method. A larger difference between maximum and minimum values leads to a more distinct longshore crest-trough pattern. As $\overline{H_{s,lf}}$ variations can have a large impact on the wetted area at the dune foot a more detailed analysis is presented below.
The longshore mean current is roughly 0.1 m/s stronger under multi-dir conditions (Figure 34).

5.1.2 IG spatial distribution

Although an in-depth analysis of the behaviour of IG waves over a variable bathymetry is outside the scope of this research, some interesting phenomena can be observed in animations[8] of the incoming IG wave fields using the single-dir method. The results have shown (Section 4.3.1) that under a 0° wave angle, a longshore IG crest-through distribution occurs at the dune foot. Although it is does not become entirely clear in the animation, a focussing of IG energy over the outer bar could be the cause of a higher IG mean wave height at positions where there is a bay in the outer bar. Under a 45° wave angle a lot of interference can be observed in the animations between incoming and reflected IG energy is observed.

[8] https://youtu.be/QpQ2M5fgCKE
https://youtu.be/4xYfqjIx5_Y

A detailed analysis in the research of Reniers et al. (2006) showed that a coupling between an edge wave field and a periodic rip channel beach can occur. Due to the near-normal incidence of the sea-swell waves in this research, this coupling was weak and the longshore variability in IG wave energy therefor low. The coupling could possibly lead to the higher mean IG height as observed in section 4.3 and more longshore variability in IG energy when the angle of incidence increases. Some IG waves are almost shore parallel after reflection. Together with a possible focussing of IG energy over the outer bar, this could lead to an increase of high values at the foot of the dune. A spectrum analysis could be the key to understand the observed IG energy distributions. This way an investigation into the contribution of the edge wave-bathymetry coupling using XBeach could help explain the longshore variability of IG wave height at the dune foot.

5.1.3 IG Wave Height

As Stockdon et al. (2014) and Palmsten & Splinter (2016) indicated, the original multi-dir XBeach underestimated the contribution of IG wave energy in the set-up. The consideration of a mean wave direction in the single-dir, instead of the total sum of wave energy from different directional bins, should result in a larger groupiness (Eq. 2.6) and therefor larger IG wave height. Figures 31 and 38 indicate that over different wave angles and H_s, single-dir is significantly larger at the dune foot, compared to the multi-dir results. The overview in figure 53 shows, as intended by Roelvink et al. (2018), an increase in IG significant wave height over the cross-shore dimension. When these results are compared to the validation by Roelvink et al. (2018) with the DELILAH field experiments, the differences between single-dir and multi-dir at the shoreward boundary of the former are significantly larger. The $\overline{H_{s,hf}}$ distribution experiences a relatively large difference between the two methods. This is possibly due to the different hydrodynamic boundary conditions or the difference in bathymetry. The difference between the single-dir and multi-dir IG significant wave height is also magnified by using the '*Roelvink93*' breaker formulation.

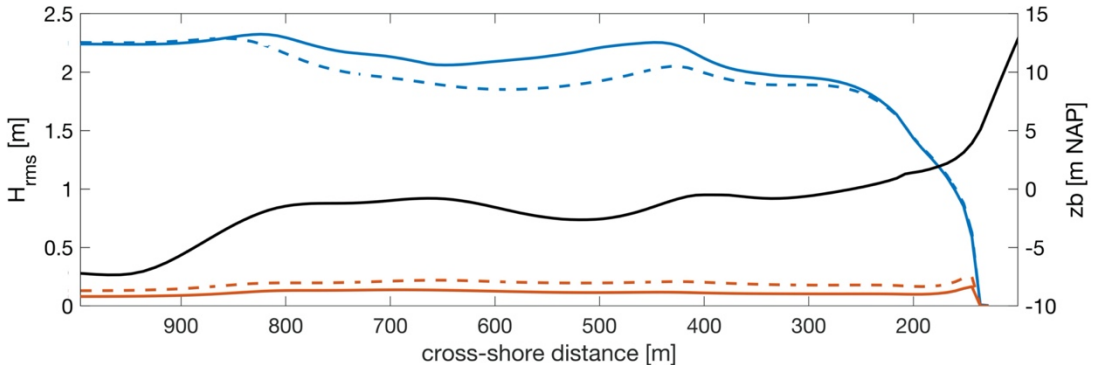

Figure 53: The blue lines indicate the $\overline{H_{s,hf}}$ with the dotted line being the single-dir method and the solid line represents the multi-dir method. The orange solid and dotted lines are the $\overline{H_{s,lf}}$ values of, respectively, the multi-dir and single-dir methods over the cross-shore horn profile. The bed level (black) is in metres NAP.

5.2 Dune erosion

5.2.1 Erosion under 0°

In XBeach, the morphology can be updated by calculating the sediment transport (Eq. 8.41 & 8.42). The sediment transport is based on the advection diffusion equation (Eq. 8.38), where currents and sediment concentrations are important parameters. The bed can also be updated using the avalanching equations (Eq. 8.44 & 8.45). When the slope of the dune front is too steep, the slope collapses and the bed level is updated until its slope is below critical levels. Under a 0° wave angle, no large erosional events were present for both the multi-dir and the single-dir method. In figure 54 the maximum slope of the phase *SNMaC* and *SNSaC* results can be observed at the dune front (Figure 16, indicated in yellow). Over time the slope steepens but stays below the critical wet slope of 0.3. The storm is finished before slumping and avalanches occur at the dune front.

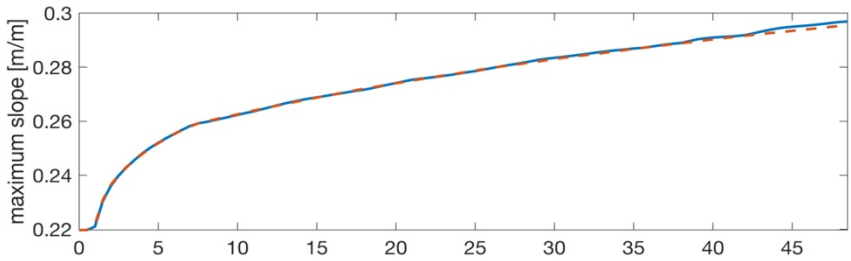

Figure 54: The mean maximum slope over time for both the multi-dir (blue solid) and single-dir (orange; striped) method. The wave angle is 0°. Over time, the mean maximum slope increases but does not reach the wet slope value of 0.3.

Considering the absence of avalanching, the bed is updated using the set of sediment transport equation, which are driven by currents, advection and diffusion. In section 4.4.1 and 4.5.1 differences in the longshore variation of mean dune front volume are observed. In figure 55a mean dune front volume at the end of the storm is plotted. The single-dir mode results in two peaks at the positions of the horns, while the multi-dir mode results in one peak per horn at 2300 and 3900 metre longshore distance.
The location of these peaks is due to a combination in longshore and cross-shore mean sediment transport. In figure 55b sediment is transported from two longshore directions (positive and negative) towards locations where a peak of 0.0002 to 0.00035 m^2/s is present. For both single-dir and multi-dir results the longshore sediment transport is very low on these locations. The sediment is transported away from locations where a bay is present in the outer bar, hence the relatively low mean dune front volume at the end of the simulation. The outer bar-dune front coupling observed by Castelle et al. 2015 is based on a strong offshore directed current at the outer bar embayment. While the same locations endure erosion in the XBeach model, the driving mechanism is different, as the rip current does not persist all the way towards the dune foot.
The cross-shore component shows a general offshore directed sediment transport, with the exceptions being the longshore boundaries. A larger offshore transport is present at horn locations, while bay locations have a slightly lower offshore transport. The cross-shore component shows the distinctive two smaller peaks in the single-dir results. The off-shore transport is an order of magnitude smaller than the longshore component (Figure 55b). Although the offshore transport is stronger at horns and uniform bars, it is not strong enough to transport the sediment to these locations by the longshore component, resulting in a relatively low loss of dune volume. This confirms the hypothesis of van Thiel et al. (2011) that the longshore component is an important driver in modelling dune erosion using XBeach. As the less directional spread of IG wave energy occurs, the longshore component is even larger using single-dir calculations, than proposed by van Thiel et al. (2011).

Although the longshore component of the sediment transport strongly resembles the mean longshore current, the cross-shore components have some crucial differences. The mean cross-shore current calculated under static bed conditions (Figure 55c) is shore directed at bay locations and offshore directed at horn conditions (Figure 55, dotted lines), while the cross-shore sediment transport is offshore directed at both locations. The offshore directed sediment transport is very likely due to the wave asymmetry as a result of wave breaking. XBeach does not solve the short waves but accounts for wave asymmetry and skewness in the advection-diffusion equation.

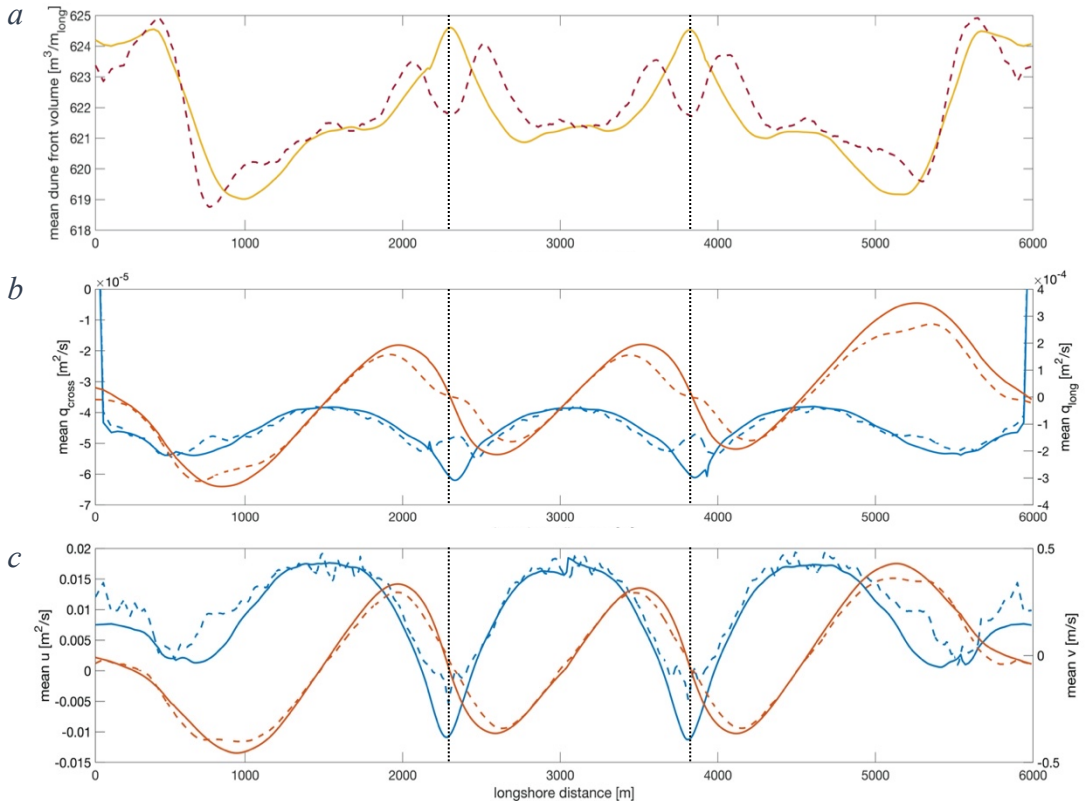

Figure 55: Figure 55a displays the mean dune front volume over the longshore dimension at the end of the 0°simulations. The yellow, solid line represent the multi-dir result (Phase SNMaC) and the red, striped line is the result of the single-dir method (Phase SNSaC). Figure 55b is the mean sediment transport averaged over simulation time periods at the dune foot. The blue lines are the mean cross-shore transport for the multi-dir (solid) and single-dir (striped) results. The orange lines illustrate the longshore sediment with the solid line for the multi-dir results and the striped line for the single-dir results. Figure 55c consists of the longshore components calculated under static bed conditions (Phase SFMaC & SFSaC). The blue lines are the multi-dir (solid) and single-dir (striped) cross-shore components of the mean current. The orange lines represent the longshore component of the mean component with both multi-dir (solid) and single-dir (striped) methods. The black dotted lines represent the longshore location of the horns in the outer bar.

5.2.2 Erosion under 45°

Under a constant wave angle of 45° and no avalanches changing the bed level, the erosion is current driven as well. More variation in loss of mean dune front volume is observed for the single-dir option as seen in section 4.5.1. Both methods show relatively large longshore sediment transport which is, contrary to 0° conditions, entirely in one direction. The longshore component of sediment transport is positive, meaning a transport towards the right (Figure 56b). The longshore distribution of mean dune front volume matches the longshore component of sediment transport. Locations with a large longshore sediment transport, have more loss in dune front volume. The cross-shore sediment transport has a lower magnitude than the longshore sediment transport.

While van Thiel et al. (2011) only focused on shore-normal waves, here it was shown that a larger wave angle leads to earlier avalanching. This results in even more longshore variability in dune erosion, compared to 0° wave angle conditions. As the single-dir method has higher peaks in the longshore mean current (Figure 56c), locations with a large loss of dune front volume have a higher erosion rate than locations with a large loss of volume under multi-dir conditions.
The cross-shore sediment transport has the same trends as the cross-shore current, the peaks in offshore directed sediment at the longshore locations of the horns (Figure 56, black dotted lines) coincide with the peaks in offshore directed mean current. These peaks in cross-shore transport correspond to locations where relatively less sediment is eroded, while the peaks in mean longshore current and sediment transport do coincide with locations with larger erosion. This confirms the hypothesis that the magnitude difference between the longshore and cross-shore component and results in a dominance of the longshore component in overall sediment transport at the dune foot. For an analysis on the contribution of IG wave height to the longshore current at the dune foot, a higher spatial resolution is necessary. The grid size of the domain is, with its minimum of 8 by 8 metres at the dune foot, relatively large. Although in general the results still seem to be representative, it limits a detailed spatial analysis of dune erosion. Few research is done on the sensitivity of XBeach results to the angle of incidince in Roelvink et al. (2009) the model was validated on a wave angle of 16°. As the longshore component plays a key role in dune erosion, a potential focus for future research presents itself.

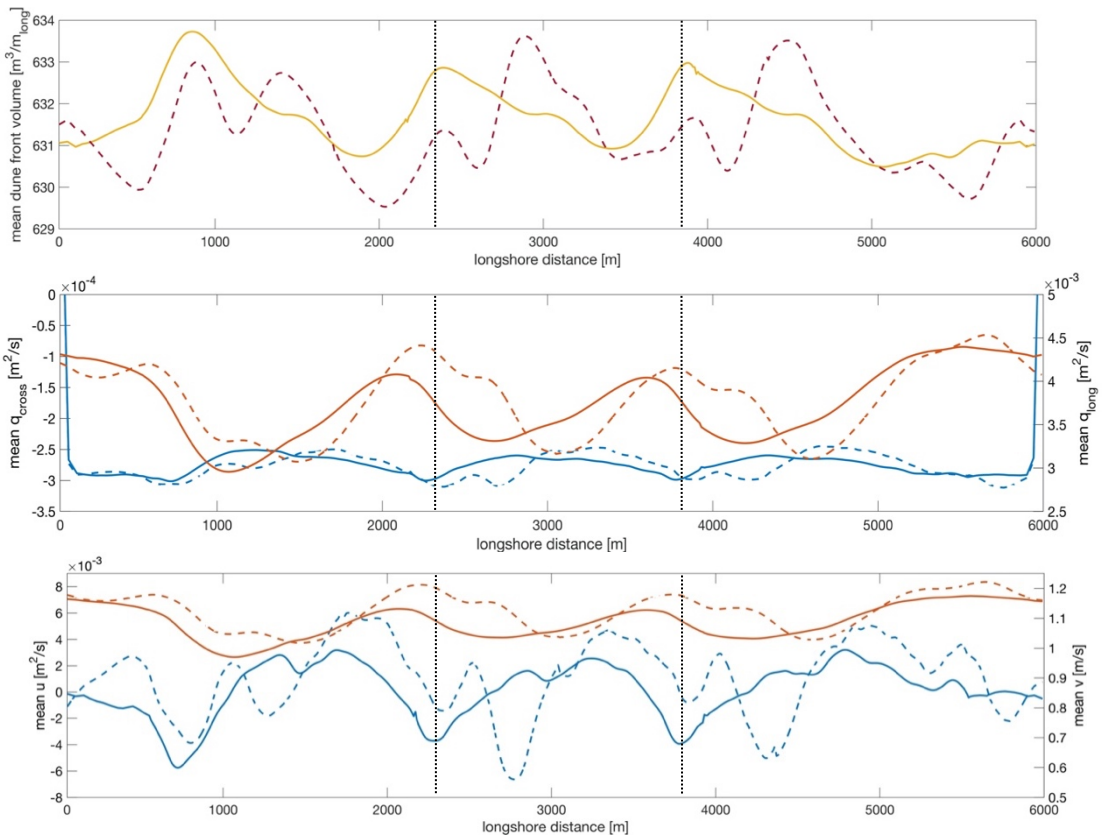

Figure 56: Figure 56a displays the mean dune front volume over the longshore dimension at the end of the -45 ° interval simulations of phase SNMdC and SNSdC. The yellow, solid line represent the multi-dir result (Phase SNMdC) and the red, striped line is the result of the single-dir method (Phase SNSdC). Figure 56b is the mean sediment transport averaged over simulation time periods at the dune foot. The blue lines are the mean cross-shore transport for the multi-dir (solid) and single-dir (striped) results. The orange lines illustrate the longshore sediment with the solid line for the multi-dir results and the striped line for the single-dir results. Figure 56c consists of the longshore components calculated under static bed conditions (Phase SFMdC & SFSdC). The blue lines are the multi-dir (solid) and single-dir (striped) cross-shore components of the mean current. The orange lines represent the longshore component of the mean component with both multi-dir (solid) and single-dir (striped) methods. The black dotted lines indicate the longshore locations of the outer bar horns.

When the 45° conditions persist, avalanching events will occur. In section 4.4.1 and 4.5.1 it becomes visible that the timing of these events differs for single-dir and multi-dir method. As depicted in figure 56 the locations with high erosion under single-dir conditions, endure a larger sediment loss than multi-dir conditions. This means that the single-dir option reached the 0.3 wet slope after 17.5 hours and the multi-dir method 7 hours later. In a more detailed look on the avalanching events (Figure 57), the longshore distribution is comparable to the results in the section above. It becomes clear that the locations of the avalanching events are in the positions where the currents, especially the longshore component, have eroded the most sediment from the dune front. The avalanches lead to a large increase in dune front volume immediately downstream. These are visible in the colour plots of section 4.4.1 to 4.5.3 as sudden, red-coloured spots and can therefore be seen as an indicator of avalanching.
In multiple animations[9] of the beach and dune front the response of the dune front to avalanching can be distilled. In the post-avalanching regime, the longshore current transports the avalanched sediment, reducing the longshore variation in bed levels. The distribution of dune front volume will, eventually, move back towards a similar profile as seen in figure 56.

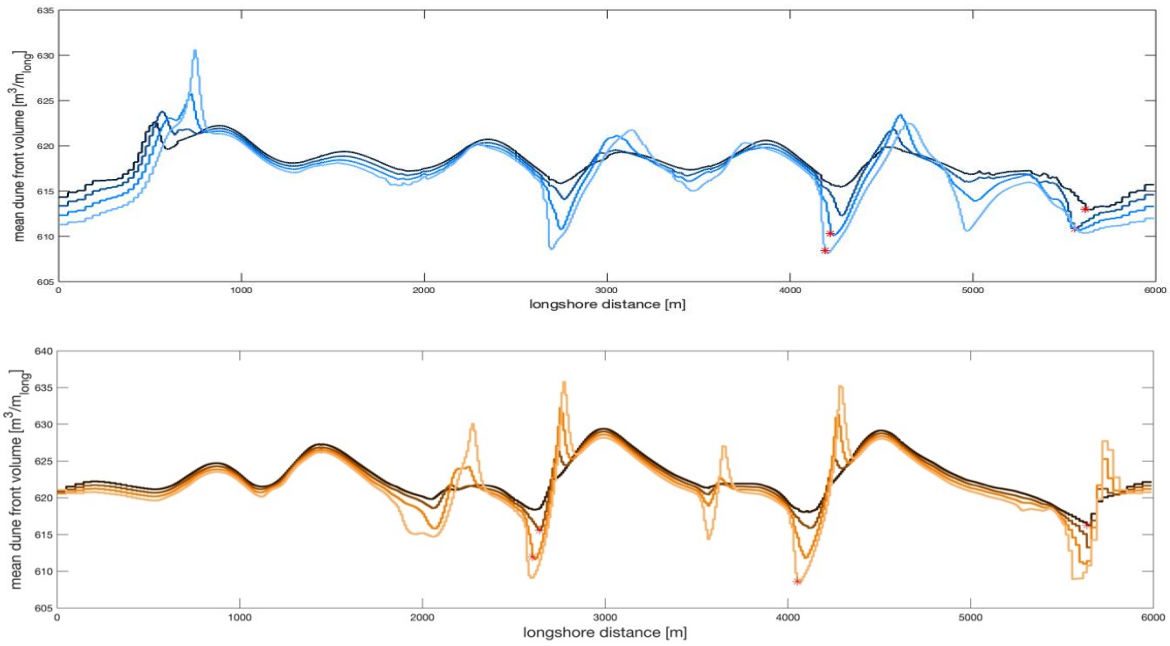

Figure 57: The upper panel displays the mean dune front volume of multiple consecutive time steps of half an hour. For the multi-dir method the avalanching starts after 24.5 hours. The bottom panel is similar but for the single-dir method. The avalanching starts earlier at 19.5 hours.

[9] https://youtu.be/0Ha7qNb6em8
https://youtu.be/ypY-_XA76u4
https://youtu.be/ZOtnsZq64WI

5.2.3 Varying conditions

Considering that the current is the dominant driver in the initiation of the avalanching process in phase SFMaC and SFSaC, it can be assumed that this is also the case for conditions where the wave angle and wave height change over time. This is confirmed when the timing of the avalanching under these conditions is compared between the two methods, with the single-dir initiating the avalanche sequences earlier. Although Roelvink et al. (2018) proved that the single-dir method improved swash predictions in a 2DH domain compared to the multi-dir method, a comparison of the single-dir method to empirical data under varying storm conditions would be recommended. Especially storm conditions where large wave angle are present, like the storm conditions in de Winter et al. (2015).
Figure 58 depict the difference between mean maximum dune front volume and the mean minimum dune front volume. A sharp increase indicates dune erosion, followed by a deposition downstream of the longshore current.
The difference between maximum and minimum values is larger for the single-dir results, under a constant angle of -45° and a variable wave angle. For phase SFMcV and SFScV the magnitude of the difference is similar. As the avalanching is driven by duration and the area of the dune that is 'wetted' (Equation 8.44 and 8.45), the magnitude of the avalanches could be related to the mean set-up or the mean IG wave height. The largest set-up values are observed at the longshore locations of horns (Figure 18, 23 and 27), while the erosional hotspots are more aligned with the embayments. As the peaks in mean IG wave height are more aligned with the embayments it could act as a driver of the differences in avalanche magnitude as the difference in mean IG wave heights between the two methods is considerably larger than the difference in set-up.

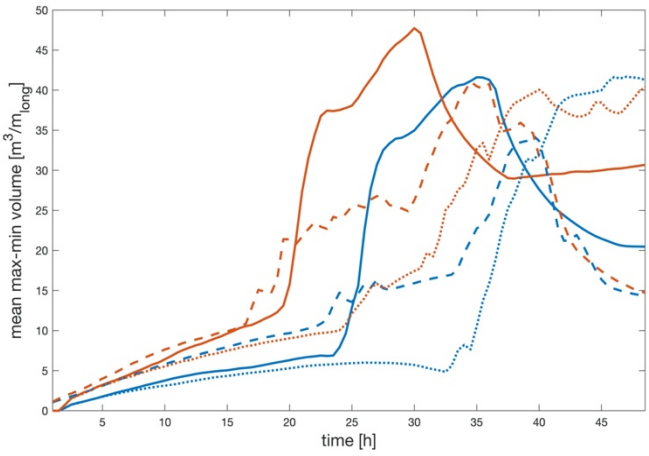

Figure 58: The difference between the mean maximum values and mean minimum values of dune front volume over time. The blue lines indicate the use of the multi-dir method, while the orange lines represent the single-dir method. The solid lines are the result of a constant -45 ° angle. The striped lines indicate a varying wave angle between -45 ° and 45 °. The dotted lines are for a varying wave angle and a varying H_{rms}.

5.2.4 Morphological context

Compared to the observations by Castelle et al. (2015) the simulation confirm that the outer bar morphology can lead to longshore variability in dune erosion. The features in both in this research and the research of Castelle et al. (2015) are more distinct than the longshore variability in bathymetry used by de Winter et al. (2015). Considering that the longshore variability in dune erosion by de Winter et al. (2015) was primarily driven by pre-storm dune topography and therefor the sediment available at the total water level, it can be said that the amount of longshore variability in dune erosion is a combination of a longshore variability in total water level, longshore current and pre-storm dune topography (Figure 59). XBeach could play a vital role in quantifying the sensitivity of dune erosion to these two contributions.

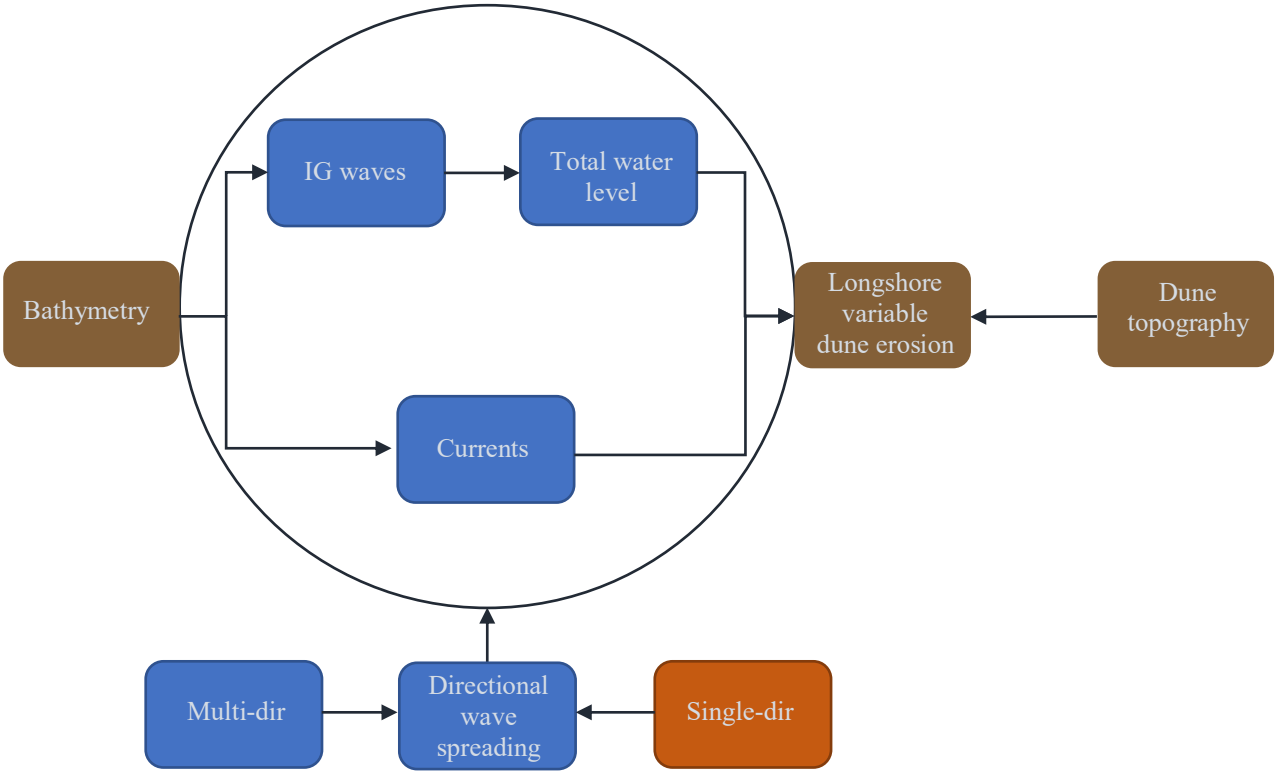

Figure 59: An overview of the processes that have an impact on longshore variability in dune erosion. Longshore variability in erosion is coupled with the outer bar trough hydrodynamic processes as hypothesized in this research and by Castelle et al. (2015). On the other hand, dune topography influences the longshore variability in dune erosion as well in line of the research of de Winter et al. (2015). The hydrodynamic processes in XBeach vary, depending on the choice between the single-dir method or multi-dir method. The former results in less directional wave spreading in the longshore direction and the latter in more directional wave spread in the longshore direction.

6. Conclusion

To conclude the research, first the impact of different wave angles and wave heights over a longshore variable bathymetry on nearshore hydrodynamic processes is addressed. Subsequently, the impact of different wave angles and wave height over a longshore variable bathymetry on dune erosion is discussed. Then, correlations between the longshore variation in dune erosion and the hydrodynamic processes are evaluated. In the answers to the final sub question, the differences in longshore variation in dune erosion and hydrodynamic conditions between the single-dir and multi-dir method are covered. With the answers to these sub questions, an overall conclusion with regards to the following main question can be established: Which processes drive longshore variability in dune erosion in numerical modelling using XBeach multi-dir and single-dir settings over crescentic sandbars?

The impact of different wave angles and wave heights on nearshore hydrodynamic processes is related to a longshore variable bathymetry. The hydrodynamic processes in the nearshore area using XBeach are coupled to an outer bar with a longshore variable morphology, consisting of regularly spaced horns and bays (crescentic sandbars). Under 0° wave angle conditions, the $\overline{H_{s,hf}}$ on the beach is largest on sections where the outer bar is characterized by a horn feature, but eventually becomes zero towards the dune foot. The IG wave height increases towards the dune front.
The nearshore is characterized by cell circulation patterns under 0° wave angle conditions. Rip currents are present over the outer bar embayments. Over the beach, the current is offshore directed over horn profiles and onshore direct on locations characterized by an embayment in the outer bar. This is opposite to the cell circulation of the double-barred beach in the research of Castelle et al. (2015).
Under a time-varying wave height and a 0° wave angle, the cell circulation changes during low H_s conditions. The result is an onshore directed current along the cross-shore dimension on locations with a horn in the outer bar, while for high H_s conditions a seaward directed current is observed over the beach and at the dune foot. The magnitude of the mean current increases with an increase in H_s as well.
With an increasing wave angle, the longshore component of the mean current becomes more dominant, reaching values of 1.6 m/s. The cell circulation pattern disappears and a unidirectional current with longshore variation in magnitude is the result.
With the increase in wave angle, a longshore crest-trough pattern in $\overline{H_{s,lf}}$ occurs at the dune foot. Up to 6 cm higher values of $\overline{H_{s,lf}}$ are observed at longshore positions with an outer bar horn. The position of this crest-trough pattern shifts leeward of the angle of incidence. This phenomenon could be the result of a coupling between an edge wave field and a periodic rip channel beach as observed by Reniers et al. (2006)

As a result of different wave angles and wave height over a longshore variable bathymetry, dune erosion is longshore variable as well. Without the avalanching mechanism initiated, variation in erosion along the dune front is relatively low. Under a 0°, less dune front erosion is observed. The slopes of the dune front take a relatively long time to reach the critical wet slope, resulting in no observed avalanches. Larger erosion is observed under larger wave angles. With a time-varying wave hight avalanching generally occurs later in time. It takes longer for the currents to erode the dune front to its critical slope. Avalanching of the dune front occurs predominantly on locations left of the embayment positions and therefor leeward of a -45°. This is the case for both a time-constant wave angle -45°of and a time-varying wave angle.
An avalanche sequence can be followed by a reducing longshore variability in bed level as a result of sediment transport in the longshore direction (van Thiel De Vries et al., 2011).

As there are two main mechanisms of dune erosion in this research, correlations between the longshore variation in dune erosion and the hydrodynamic processes can be analysed. The first mechanism that updates the bed level is sediment transport by current. As the longshore sediment transport is an order of magnitude larger under all conditions, the results confirm the findings of van Thiel de Vries et al. (2011) that the longshore component is an important driver of dune erosion. The locations with the strongest mean longshore location endure the most erosion. It is therefore very likely that the longshore component of the mean current is a dominant driver of dune erosion. Longshore locations where avalanches occur coincide with a relatively high longshore mean current, leading to the assumption that the current also plays an important role in initiating the avalanching mechanism. The avalanching mechanism is steered by the total water level, as the total water level determines the area that is 'wet' and therefor the area where the wet slope is applied. As IG wave energy can be a significant component of the total water level, it can have an impact on the magnitude of the avalanche. This is similar to the research of Castelle et al. (2015), where wave impact on the dune front is the main erosional mechanism.

The differences in longshore variation hydrodynamic conditions between the single-dir and multi-dir method are predominantly in magnitude. The single-dir method has significantly higher values of mean IG wave height in the nearshore area and at the dune foot the difference can be up to 15 cm. This is in line with the intention of the adjustments to XBeach by Roelvink et al. (2018). The $\overline{H_{s,hf}}$ up to 0.4 is lower in the near-shore area. The mean current shows some minor differences in magnitude in the cell circulation pattern under 0° conditions and at the foot of the dune more longshore variation in both the mean cross-shore and longshore component of the current is observed. When the wave angle increases, the longshore component of the mean current using the single-dir method can be up to 0.2 m/s stronger than the multi-dir method. Considering the avalanching events, the single-dir leads to an earlier initiation and larger magnitudes compared to the multi-dir method.

To conclude, the processes driving longshore variability in dune erosion in numerical modelling using XBeach multi-dir and single-dir settings over crescentic sandbars are two-fold. Before reaching a critical slope, the longshore variation in dune erosion is driven by the longshore current. This is increasingly visible under the conditions with a larger wave angle. The longshore variation in the current is linked to the outer bar morphology. Locations with a bay present in the outer bar, have a stronger longshore current. When the wave angle shifts, these locations migrate leeward of the incoming wave direction. The second mechanism in dune erosion present in XBeach is avalanching. When the slope reaches a critical value, which is less steep under 'wet' conditions, an avalanche changes the bed level in order to reach a state where the slope no longer steep enough for avalanches to occur. The critical slope is reached earlier at locations where the dune front has eroded most, as a result of the mean current. The magnitude of the avalanching could be the result of IG wave energy. After an avalanching event, the current distributes the sediment in the longshore dimension, resulting in a more uniform dune front. For future research, the exact contribution of IG wave energy during these avalanching events could be an interesting topic to further deepen our knowledge of the importance of IG wave energy in coastal dynamics. Furthermore, an analysis of the drivers of longshore variability in the mean current could add to our understanding of longshore variability in dune erosion.
If XBeach is used for this purpose, one should consider that more validation for the single-dir method is necessary. Especially for conditions where the wave angle increases. Under these conditions, the single-dir method leads to a larger longshore variability as a result of less directional spreading of short-wave groups.
For our global understanding of longshore variability in dune erosion two insights are important. As Castelle et al. (2015) observed in the field, the total water level, influenced by bathymetry can play a large role in the longshore variability of dune erosion. On the other hand, the amount of sediment present at the total water level as a result of a variable dune topography can also be a dominant driver of longshore variable dune erosion (de Winter et al. 2015). Future research should be focused on determining the favourable conditions for these two hypotheses and, more interestingly, the conditions in which a shift from total water level to dune topography as an important driver in dune erosion is occurring.

7. Acknowledgements

Many have supported me in the process of this research. First of all, I would like to thank Timothy Price for the support as first supervisor. As a result of his feedback the report improved greatly, and the results came fully to their rights.
Furthermore, a special thanks is in place to Mark Heij, without the generous gesture of lending me his laptop for the computations, I would never be able to create the dataset necessary for this research.
I want to thank my family for their great support and providing me with an ‘office’, where I laid the groundwork of this thesis. Last but not least I want to thank Debora van der Velden for supporting me along this journey, no one could have done this better than you.

8. Appendix A

8A.1 XBeach in depth

8A.1.1 Short wave action

To solve the variation in wave forcing of short-wave envelopes on a group scale, Roelvink et al. (2009) use the wave-action balance equation (Eq. 8.1). This equation is based on the HISWA model and calculates the time-dependent motion of short waves (Holthuijsen et al., 1989):

$$\frac{\partial A}{\partial t} + \frac{\partial c_x A}{\partial x} + \frac{\partial c_y A}{\partial y} + \frac{\partial c_\theta A}{\partial \theta} = -\frac{D_w}{\sigma} \tag{8.1}$$

where t is time, x and y represent respectively the cross-shore and long-shore direction. θ is the directional angle with respect to the x-axis. c is the wave-action propagation speed. The subscript in c determines the directional bin. A is the wave-action density:

$$A(x, y, t, \theta) = \frac{S_w(x, y, t, \theta)}{\sigma(x, y, t)} \tag{8.2}$$

S_w is the wave energy density in the directional dimensions. Normally the wave energy density is used in an energy balance equation. The wave-action density uses a Eulerian approach (Holthuijsen et al., 1989). The intrinsic frequency σ is calculated as follows:

$$\sigma = \sqrt{gk \tanh kh} \tag{8.3}$$

Where k represents the absolute wavenumber, the number of times a wave occurs over a unit distance, and h is the local water depth. Because the waves and currents interact with each other by exchanging energy, the wavenumber has to be updated every time step. This has to be done for both the x and y wave vector.

$$k_x = k_x^{n-1} + k_x^{:} \tag{8.4}$$
$$k_y = k_y^{n-1} + k_y^{:} \tag{8.5}$$

$n-1$ refers to the wavenumber in the previous time step. $k^{:}$ is the correction component on the wavenumber in the previous time step and is calculated using a set of Eikonal equations:

$$\frac{\partial k_x}{\partial t} + \frac{\partial \omega}{\partial x} = 0 \tag{8.6}$$
$$\frac{\partial k_y}{\partial t} + \frac{\partial \omega}{\partial y} = 0 \tag{8.7}$$

This leads to the computation of the absolute wavenumber k.

$$k = \sqrt{k_x^2 + k_y^2} \tag{8.8}$$

The absolute radial frequency ω is given by:

$$\omega = \sigma + k_x u^L + k_y v^L \tag{8.9}$$

u^L and v^L respectively represent the cross-shore and longshore Lagrangian depth-averaged velocity, which is calculated using shallow water equations (Section 8.1.3). With no currents present, interaction between wave action and current does not occur. u^L and v^L values would be zero, resulting in an intrinsic frequency (σ) equal to the absolute radial frequency ω (Eq. 8.9).

To calculate the propagation speed with current interference in every directional bin necessary for the wave-action balance equation (Eq. 8.1), the following set of equations is used:

$$c_x(x,y,t,\theta) = c_g \cos(\theta) + u^L \tag{8.10}$$

$$c_y(x,y,t,\theta) = c_g \sin(\theta) + v^L \tag{8.11}$$

$$c_\theta(x,y,t,\theta) = \frac{\sigma}{\sinh 2kh}\left(\frac{\partial h}{\partial x}\sin\theta - \frac{\partial h}{\partial y}\cos\theta\right) + \cos\theta\left(\sin\theta\frac{\partial u}{\partial x} - \cos\theta\frac{\partial u}{\partial y}\right) + \sin\theta\left(\sin\theta\frac{\partial v}{\partial x} - \cos\theta\frac{\partial v}{\partial y}\right) \tag{8.12}$$

where c_g indicates the group, velocity based on the wave envelopes. The left-hand side of equation 1 has now been completed.
Changes of incoming wave action over time and space have to be balanced by an energy dissipation. In the wave-action balance the dissipation of energy is the result of the breaking of waves (D_w). When the wave action increases over space or time, the dissipation of energy as the result of wave breaking, increases as well. In the initial release, D_w is calculated using the method of Roelvink (1993). This method starts by first resolving the total dissipation by wave breaking $\overline{D}_w$:

$$\overline{D}_w = \frac{\alpha}{\pi} Q_b \sigma E_w \frac{H_{rms}}{h} \tag{8.13}$$

When the water depth (h) decreases and wave energy reaches the bottom, waves start to deform. The waves steepen and eventually start breaking. The relation between depth and wave height, would imply that there is a deterministic element based on the characteristics of the waves, which causes the waves to break. This is calculated based on the Battjes and Janssen model, where the breaking wave acts like a bore (Battjes & Janssen, 1978). The wave characteristics are represented in the equation above as total short-wave energy E_w and σ. α is a calibration coefficient.
In reality the breaking of waves is very complex. It is therefore difficult to accurately predict the location where a wave starts to break. This problem is resolved by including the probabilistic factor Q_b. Q_b represents the probability that the wave is breaking. The probability of a wave breaking increases towards 1 when wave energy increases or depth decreases (Roelvink, 1993). It is calculated as follows:

$$Q_b = 1 - \exp\left(-\left(\frac{H_{rms}}{H_{max}}\right)^n\right) \tag{8.14}$$

$$H = \sqrt{\frac{8E_w}{\rho g}} \tag{8.15}$$

$$H_{max} = \frac{\gamma \tanh kh}{k} \tag{8.16}$$

with ρ representing the water density, g the gravitational constant and γ the breaker index. Equation 8.15 shows that the wave height is calculated based on the total wave energy. The total wave energy (E_w) is an integration of the wave energy density S_w over the directional bins.

$$E_w(x,y,t) = \int_0^{2\pi} S_w(x,y,t,\theta)\,d\theta \tag{8.17}$$

In order to implement the wave-action balance, the total dissipation by breaking $\overline{D}_w$ is assigned in the right proportions to the directional bins.

$$D_w(x,y,t,\theta) = \frac{S_w(x,y,t,\theta)}{E_w(x,y,t)}\overline{D}_w(x,y,t) \tag{8.18}$$

Solving the wave action balance has leads to the determination of the wave energy and its spatial distribution. The radiation stress can now be calculated (Longuet-Higgins & Stewart, 1962).

$$S_{xx,w}(x,y,t) = \int \left(\frac{c_g}{c}(1 + \cos^2\theta) - \frac{1}{2}\right) S_w d\theta \tag{8.19}$$

$$S_{xy,w}(x,y,t) = S_{yx,w} = \int \sin\theta \cos\theta \left(\frac{c_g}{c} S_w\right) d\theta \tag{8.20}$$

$$S_{yy,w}(x,y,t) = \int \left(\frac{c_g}{c}(1 + \sin^2\theta) - \frac{1}{2}\right) S_w d\theta \tag{8.21}$$

8A.1.2 Roller energy balance

In XBeach, an additional element is present for modelling hydrodynamic conditions. When a wave breaks a turbulent wall of foam forms at the shoreward side of the wave. This circulating wall of foam is known as the 'roller'. The roller contributes to the total radiation stress, influencing the local sea level. The derivation of the roller radiation stress starts with the roller energy balance, where dissipation of waves by breaking (D_w) is the energy input (Roelvink et al., 2009). $S_r$is the roller energy as a function of x, y, t and θ:

$$\frac{\partial S_r}{\partial t} + \frac{\partial c_x S_r}{\partial x} + \frac{\partial c_y S_r}{\partial y} + \frac{\partial c_\theta S_r}{\partial \theta} = -D_r + D_w \tag{8.22}$$

The propagation speed in the x- and y-direction differ from equation 8.10 and 8.11. In the wave energy balance c_x and c_y are calculated based on the group velocity c_g, while in the roller energy balance the phase speed c is used. The phase speed is calculated in equation 8.23. c_θ is computed in the same way as in equation 8.12 (Roelvink et al., 2009).

$$c = \frac{\sigma}{k} \tag{8.23}$$

The total roller energy dissipation ($\overline{D}_r$) is calculated and assigned to the wave directions as follows (Nairn et al., 1991, Reniers, 2004):

$$\overline{D}_r = \frac{2g\beta_r E_r}{c} \tag{8.24}$$

$$D_r(x, y, t, \theta) = \frac{S_r(x, y, t, \theta)}{E_r(x, y, t)} \overline{D}_r(x, y, t) \tag{8.25}$$

β_r is the mean slope of the wave front under the roller. This results in the following calculations of the radiation stress contribution of the roller (Nairn et al., 1991):

$$S_{xx,r}(x, y, t) = \int \cos^2\theta \, S_r d\theta \tag{8.26}$$

$$S_{xy,r}(x, y, t) = S_{yx,r}(x, y, t) = \int \sin\theta \cos\theta S_r d\theta \tag{8.27}$$

$$S_{yy,r}(x, y, t) = \int \sin^2\theta S_r d\theta \tag{8.28}$$

The wave forcing in the cross-shore and longshore current is determined using the combined gradient in radiation stress of wave action and the roller.

$$F_x(x, y, t) = -\left(\frac{\partial S_{xx,w} + S_{xx,r}}{\partial x} + \frac{\partial S_{xy,w} + S_{xy,r}}{\partial y}\right) \tag{8.29}$$

$$F_y(x, y, t) = -\left(\frac{\partial S_{xy,w} + S_{xy,r}}{\partial x} + \frac{\partial S_{yy,w} + S_{yy,r}}{\partial y}\right) \tag{8.30}$$

8A.1.3 Shallow water equations

To complete the set of equations for modelling the wave-forcings over an arbitrary beach profile, the interaction between waves and currents (u^L and v^L) needs to be resolved. The mean and long-wave currents are calculated using the shallow water equations. XBeach uses the Lagrangian velocity for calculating the velocity of these current. In calculating the Lagrangian velocity, a particle of water is followed during a wave period. The travelling distance of the particle divided by the wave period represents the velocity.
The difficulties in tracking particles of water led to the development of the Generalized Lagrangian Mean formulation. Andrews & Mcintyre (1978) based their calculation of the Lagrangian velocity on the Eulerian velocity. The perceived velocity at a fixed point is the Eulerian velocity (u^E, v^E). The GLM was implemented by Walstra et al. (2001) to model the wave-induced mass flux and resulting in the following set of equations:

$$u^L = u^E + u^S \tag{8.31}$$
$$v^L = v^E + v^S \tag{8.32}$$

The Lagrangian velocity in x- and y-directions is equal to the Eulerian velocity plus the Stokes drift (u^S, v^S). Where the Stokes drift is calculated in equation 8.33 and 8.34.

$$u^S = \frac{E_w \cos\theta}{\rho h c} \tag{8.33}$$
$$v^s = \frac{E_w \sin\theta}{\rho h c} \tag{8.34}$$

A set of momentum equations can now be given for the mean and long-wave currents:

$$\frac{\partial u^L}{\partial t} + u^L \frac{\partial u^L}{\partial x} + v^L \frac{\partial u^L}{\partial y} - f v^L - v_h \left(\frac{\partial^2 u^L}{\partial x^2} + \frac{\partial^2 u^L}{\partial y^2} \right) = \frac{\tau_{sx}}{\rho h} - \frac{\tau_{bx}^E}{\rho h} - g \frac{\partial \eta}{\partial x} + \frac{F_x}{\rho h} \tag{8.35}$$

$$\frac{\partial v^L}{\partial t} + v^L \frac{\partial v^L}{\partial x} + v^L \frac{\partial v^L}{\partial y} - f u^L - v_h \left(\frac{\partial^2 v^L}{\partial x^2} + \frac{\partial^2 v^L}{\partial y^2} \right) = \frac{\tau_{sy}}{\rho h} - \frac{\tau_{by}^E}{\rho h} - g \frac{\partial \eta}{\partial y} + \frac{F_y}{\rho h} \tag{8.36}$$

$$\frac{\partial \eta}{\partial t} + \frac{\partial h u^L}{\partial x} + \frac{\partial h v^L}{\partial y} = 0 \tag{8.37}$$

Where f represents the Coriolis force, $v_h$the horizontal viscosity, η the water level. τ_s and τ_b are respectively the wind shear stress and the bottom shear stress. The superscript in the shear stress terms indicates that they are calculated using Eulerian velocity. The combination of the wave action balance and the shallow water equations provide the hydrodynamical boundary conditions required for calculating the sediment transport.

8A.1.4 Sediment transport and dune erosion

As the result of wave action over time, currents transport sediment and the morphology of the coastal area changes. The depth-averaged advection diffusion equation based on the work of Galappatti and Vreugdenhil (1985), is used to model the behaviour of sediment concentrations. To calculate the depth averaged sediment transport, the equation has to parameterized. The sediment source on the right-hand side of equation 8.38, is based on the difference between sediment concentration (C) and an equilibrium concentration (C_{eq}).

$$\frac{\partial hC}{\partial t} + \frac{\partial hC(u^E - u_a \sin\theta_m)}{\partial x} + \frac{\partial hC(v^E - u_a \cos\theta_m)}{\partial y} + \frac{\partial}{\partial x}\left[D_h h \frac{\partial C}{\partial x}\right] + \frac{\partial}{\partial y}\left[D_h h \frac{\partial C}{\partial y}\right] = \frac{hC_{eq} - hC}{T_s} \tag{8.38}$$

Where D_h represents the diffusion coefficient. u_a compensates for the effects of wave asymmetry and skewness. T_s is the adaptation time of the sediment. Lower values of T_s indicate a faster response of the sediment:

$$T_s = \max\left(0.05\frac{h}{w_s}, 0.2\right)s \tag{8.39}$$

The fall velocity of the sediment is represented by w_s. XBeach has different possibilities for calculating the equilibrium sediment concentration. In initial surfbeat modus, XBeach calculates the equilibrium sediment concentration based on the formulation of Soulsby (1997) and Van Rijn (1985):

$$C_{eq} = \frac{A_{sb}+A_{ss}}{h}\left(\left(|u^E|^2 + 0.018\frac{u_{rms}^2}{C_d}\right)^{0.5} - u_{cr}\right)^{2.4}(1\text{-}\alpha_b m) \tag{8.40}$$

A_{sb} and A_{ss} are sediment coefficient for, respectively, the bed load and the suspended sediment. u_{rms} represents the near bed orbital velocity varying over wave-groups and C_d is the drag coefficient. The critical velocity (u_{cr}) is based on water depth and grainsize of the sediment. The blue section of equation 8.40 can be seen as the sediment stirring component. The combination of mean, IG and short-wave orbital velocity, has to exceed the critical velocity for sediment to be set in motion.
Finally, the bed slope influences the equilibrium concentration as well. This is expressed in the term $1 - \alpha_b m$. m is the bed slope and α_b is a calibration factor. This closes the set of equations for the depth-averaged advection diffusion equation and makes it possible for XBeach to calculate the transport of sediment in x- and y-directions:

$$q_x(x,y,t) = \left[\frac{\partial hCu^E}{\partial x}\right] + \left[\frac{\partial}{\partial x}\left[D_h h \frac{\partial C}{\partial x}\right]\right] \tag{8.41}$$

$$q_y(x,y,t) = \left[\frac{\partial hCu^E}{\partial y}\right] + \left[\frac{\partial}{\partial y}\left[D_h h \frac{\partial C}{\partial y}\right]\right] \tag{8.42}$$

When the transport in both directions is calculated, the final step in modelling morphological change is updating the bed (z_b). The change in bed-level over time is based on the sediment transport of equation 8.41 and 8.42.

$$\frac{\partial z_b}{\partial t} + \frac{f_{mor}}{(1-p)}\left(\frac{\partial q_x}{\partial x} + \frac{\partial q_y}{\partial y}\right) = 0 \tag{8.43}$$

With p representing the porosity of the sediment. With increasing porosity, the sediment is less compact and will be transported in higher rates. f_{mor} acts as an acceleration factor and can be used to speed up the morphological process (Reniers, 2004).

An adjustable threshold is added to XBeach to solve the dune erosion processes. The model uses a critical slope (m_{cr}) for activating slumping and avalanching. When the critical slope is exceeded, sediment is exchanged between the grid-cells, until the slope is less steep than the critical slope (Roelvink et al., 2009). The values for the critical slope differ between wet or dry conditions. In the case of inundated areas, slumping occurs under less steep conditions. This includes the total water level at a given location as a driver of dune erosion. This avalanching mechanism results in the following equations:

$$\left|\frac{\partial z_b}{\partial x}\right| > m_{cr} \tag{8.44}$$

$$\left|\frac{\partial z_b}{\partial y}\right| > m_{cr} \tag{8.45}$$

The default wet and dry critical slopes are based on the research of Vellinga (1986) and are respectively 0.3 and 1.

Appendix 8B

8B.1 Longshore IG wave height

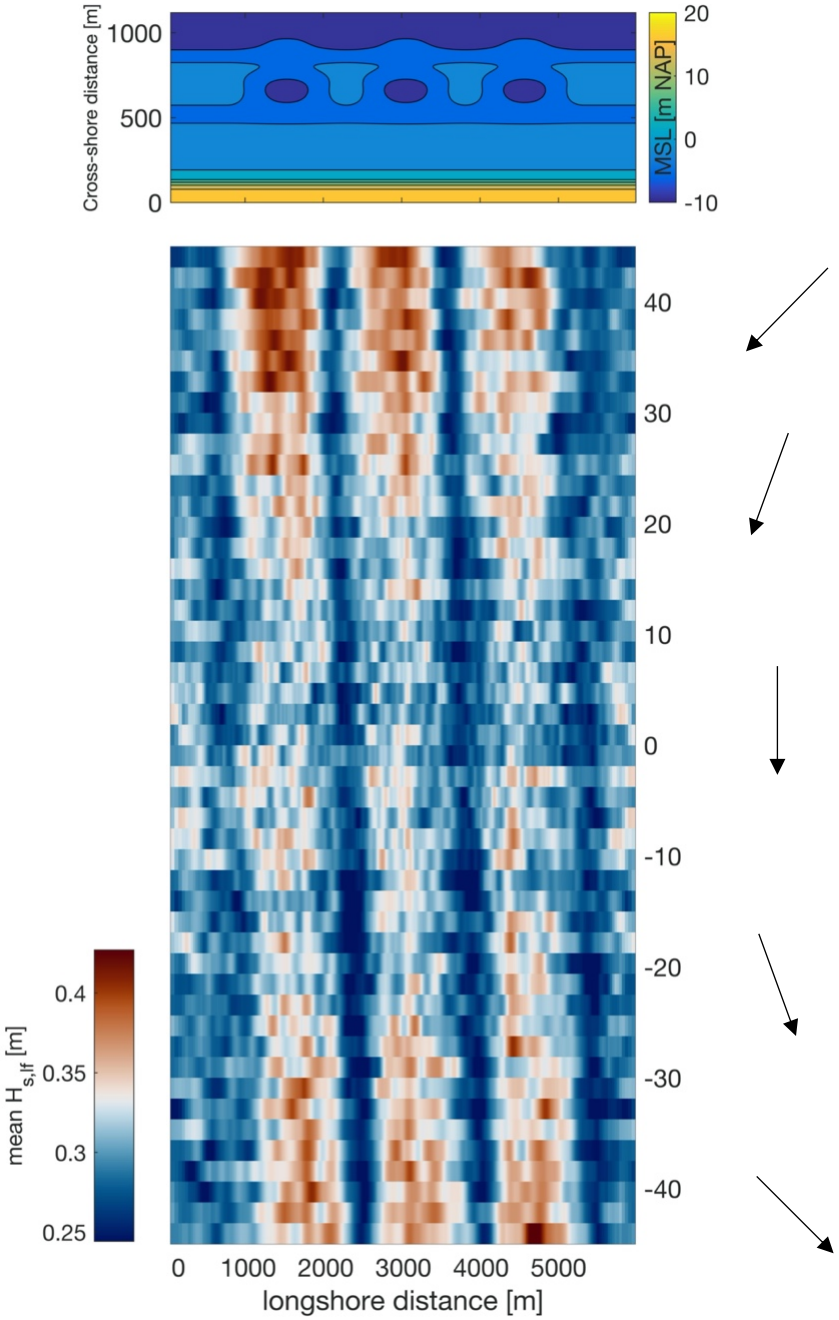

Figure 60: The upper displays the bathymetry with the location of the horns and bays. The bottom panel shows the mean significant IG wave height at the dune foot, indicated by a colour scale. The arrows indicate a time-varying wave angle.

8B.2 Cross-shore profiles

8B.2.1 *SFMbC*, -45°

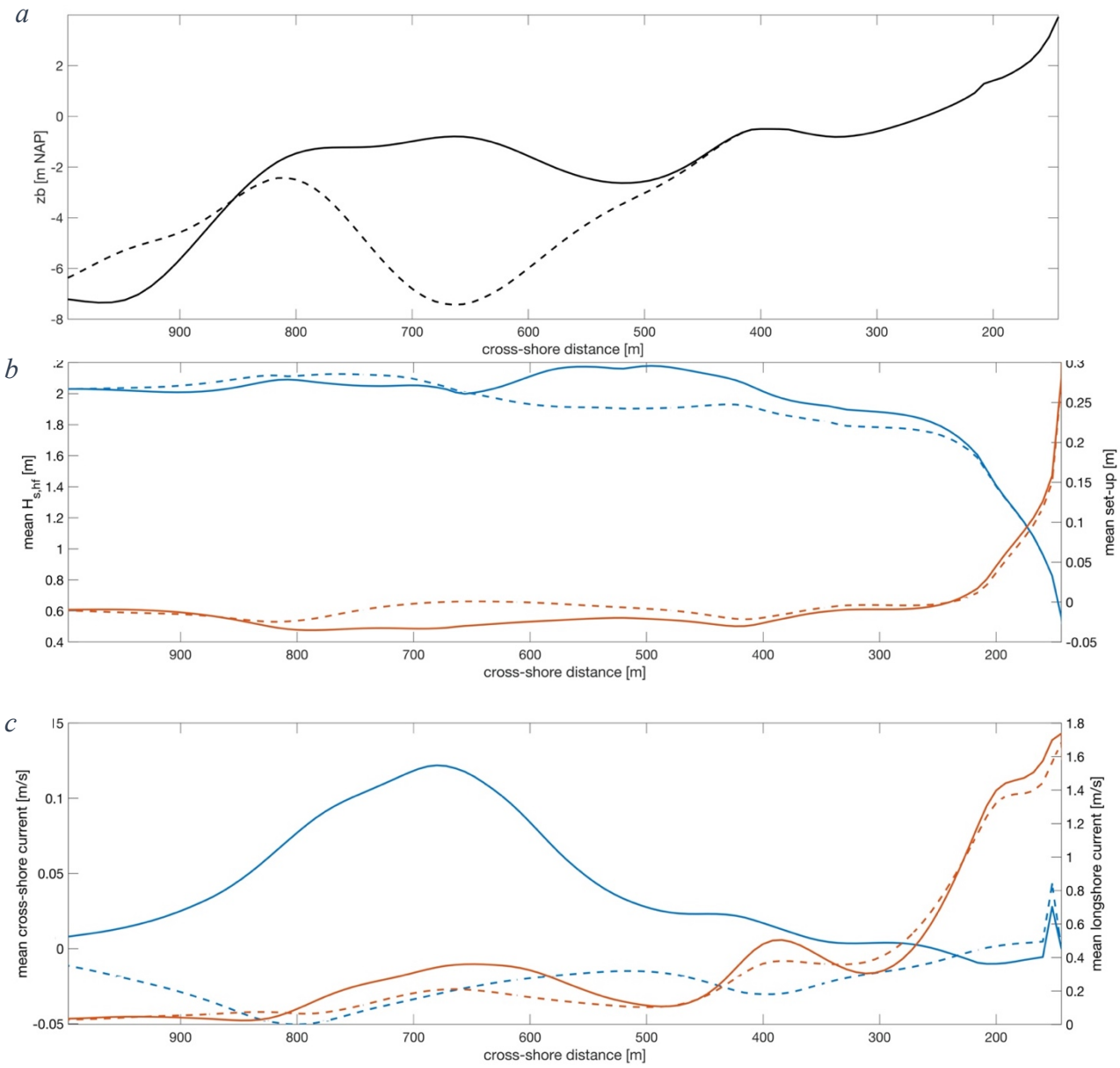

Figure 61: Figure 61a displays the cross-shore profile of a horn (solid) and an embayment (striped) in metres NAP. In figure 61b the mean significant short-wave height (blue) is plotted for the horn profile (solid) and the embayment profile (striped) of phase SFMcC. On the right-hand x-axis the mean set-up is plotted in orange. Figure 61c displays both the cross-shore (blue) and longshore (orange) components of the mean current.

8B.2.2 *SFSaC*

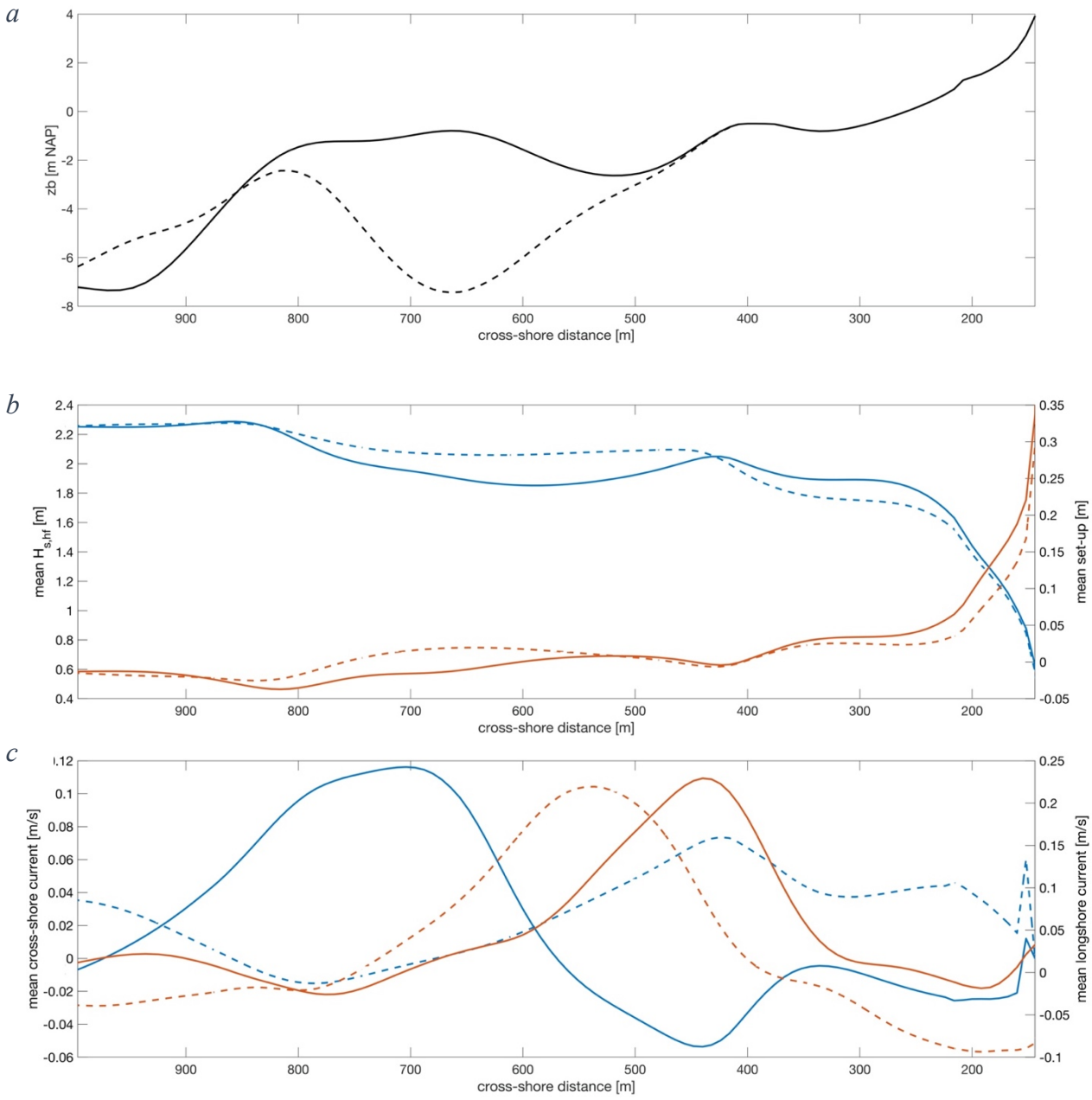

Figure 62: Figure 62a displays the cross-shore profile of a horn (solid) and an embayment (striped) in metres NAP. In fgure 62b the mean significant short-wave height (blue) is plotted for the horn profile (solid) and the embayment profile (striped) of phase SFSaC. On the right-hand x-axis the mean set-up is plotted in orange. Figure 62c displays both the cross-shore (blue) and longshore (orange) components of the mean current.

8B.2.3 *SFSbC*, -45°

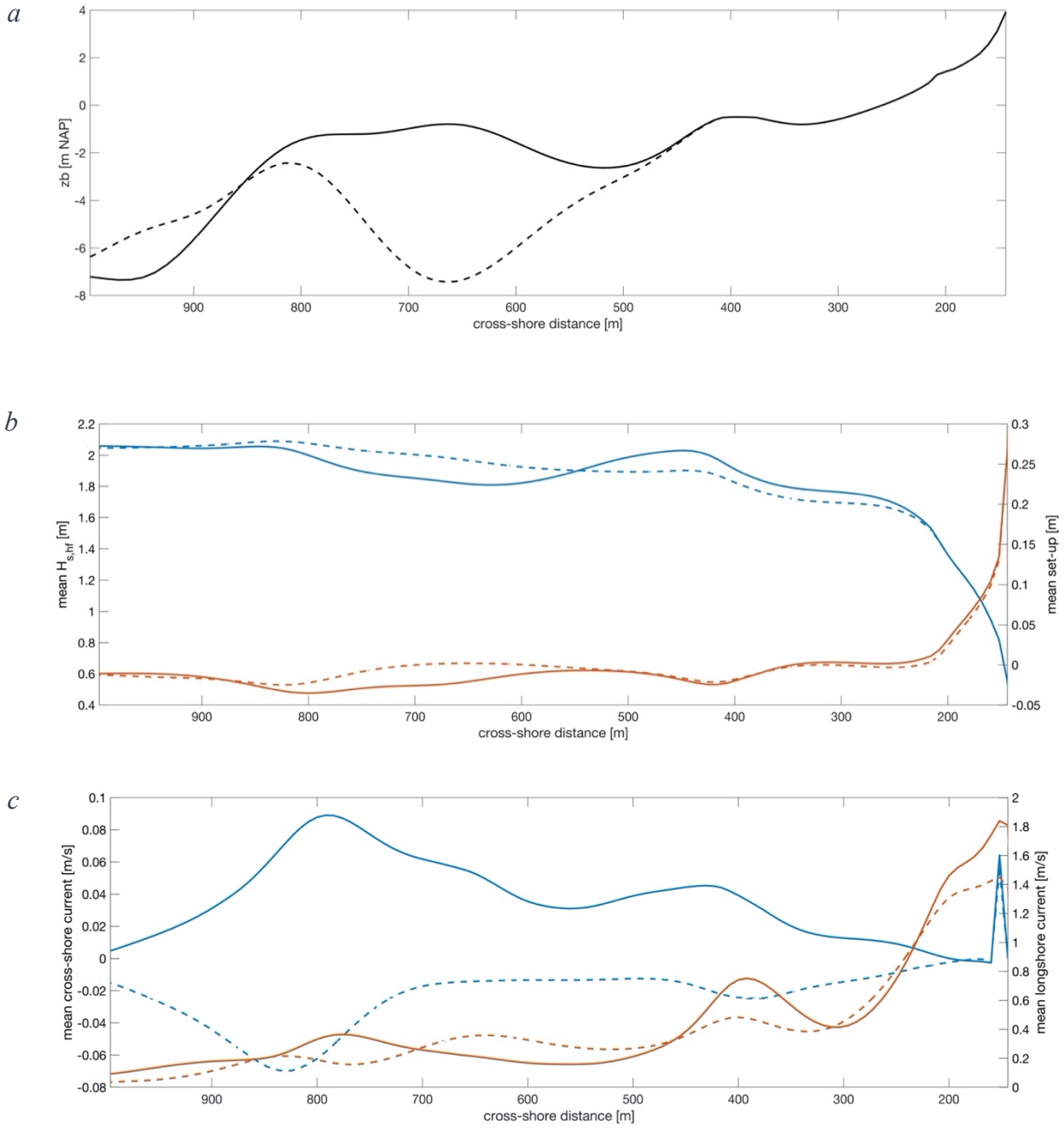

Figure 63: Figure 63a displays the cross-shore profile of a horn (solid) and an embayment (striped) in metres NAP. In figure 63b the mean significant short-wave height (blue) is plotted for the horn profile (solid) and the embayment profile (striped) of phase SFSbC. On the right-hand x-axis the mean set-up is plotted in orange. Figure 63c displays both the cross-shore (blue) and longshore (orange) components of the mean current.

8B.3 Longshore profiles

8B.3.1 *SFSaC*

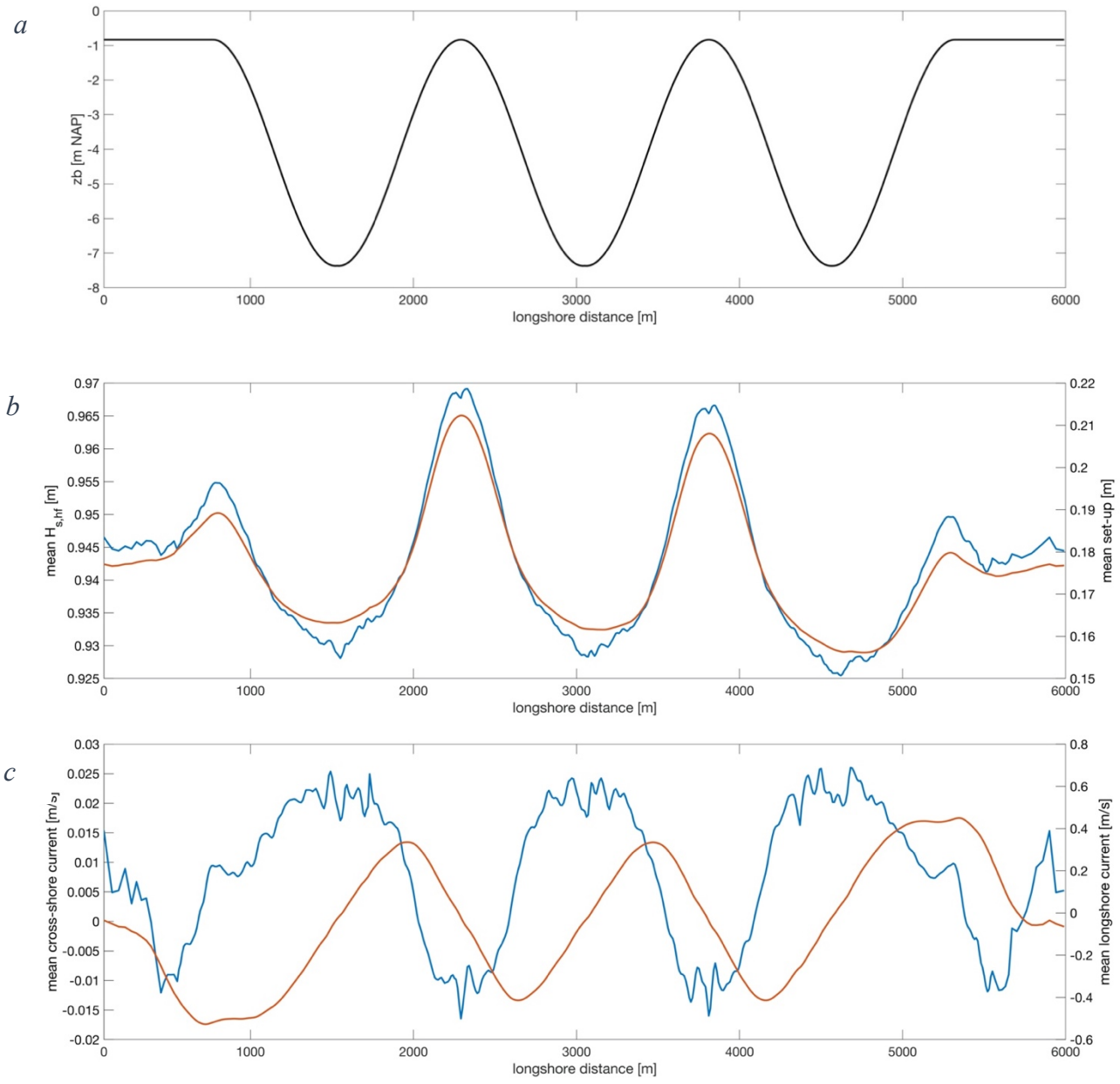

Figure 64: Figure 64a displays the longshore profile of the outer bar in metres NAP. In figure 64b the mean significant short-wave height (blue) is plotted averaged over the beach of phase SFSaC. On the right-hand x-axis the mean set-up is plotted in orange. Figure 64c displays both the cross-shore (blue) and longshore (orange) components of the mean current averaged over the beach.

8B.3.2 *SFSbC*, -45°

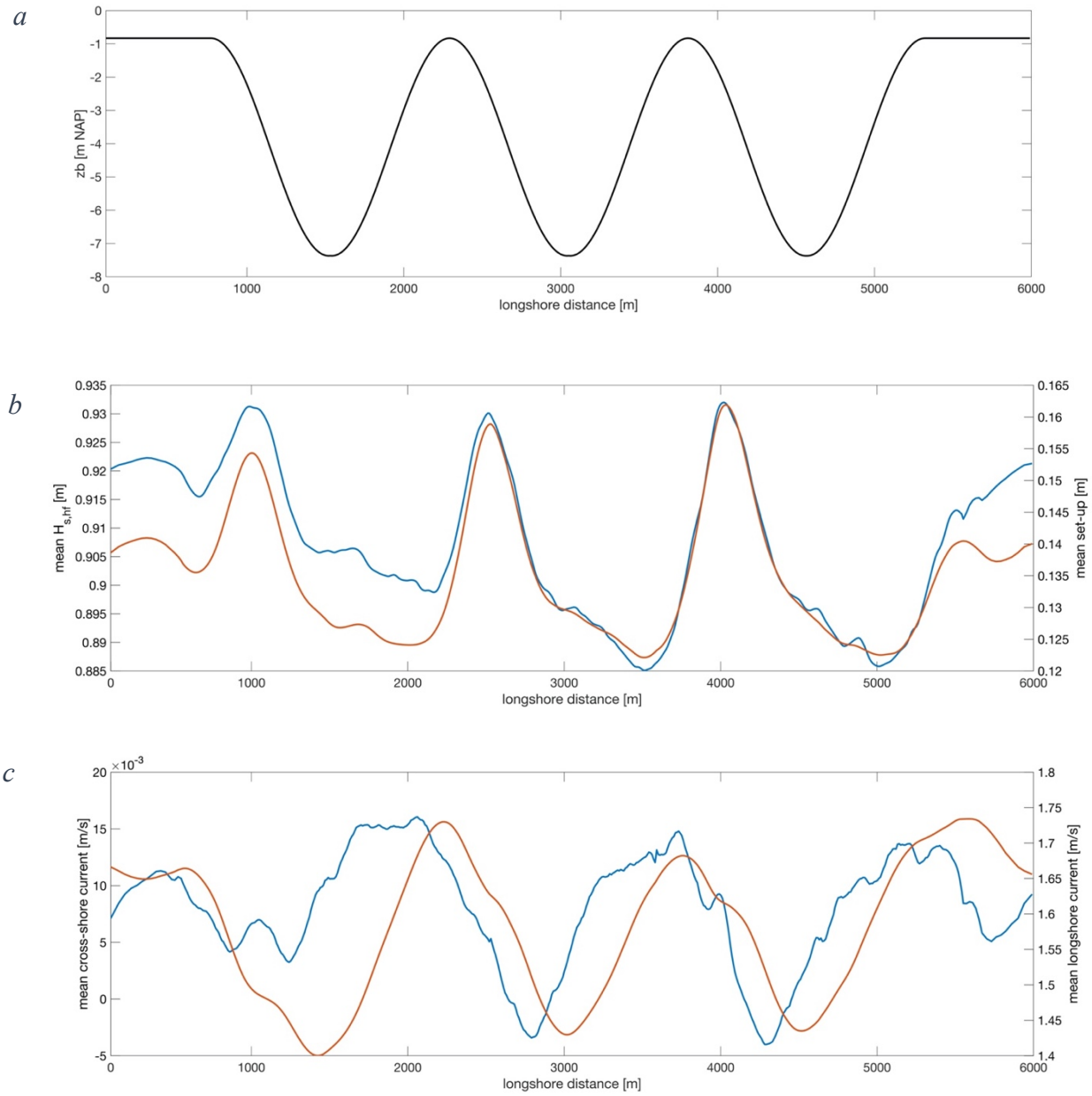

Figure 65: Figure 65a displays the longshore profile of the outer bar in metres NAP. In figure 65b the mean significant short-wave height (blue) is plotted averaged over the beach of phase SFSbC. On the right-hand x-axis the mean set-up is plotted in orange. Figure 65c displays both the cross-shore (blue) and longshore (orange) components of the mean current averaged over the beach.

8B.4 Dune erosion

8B.4.1 *SNSaC*

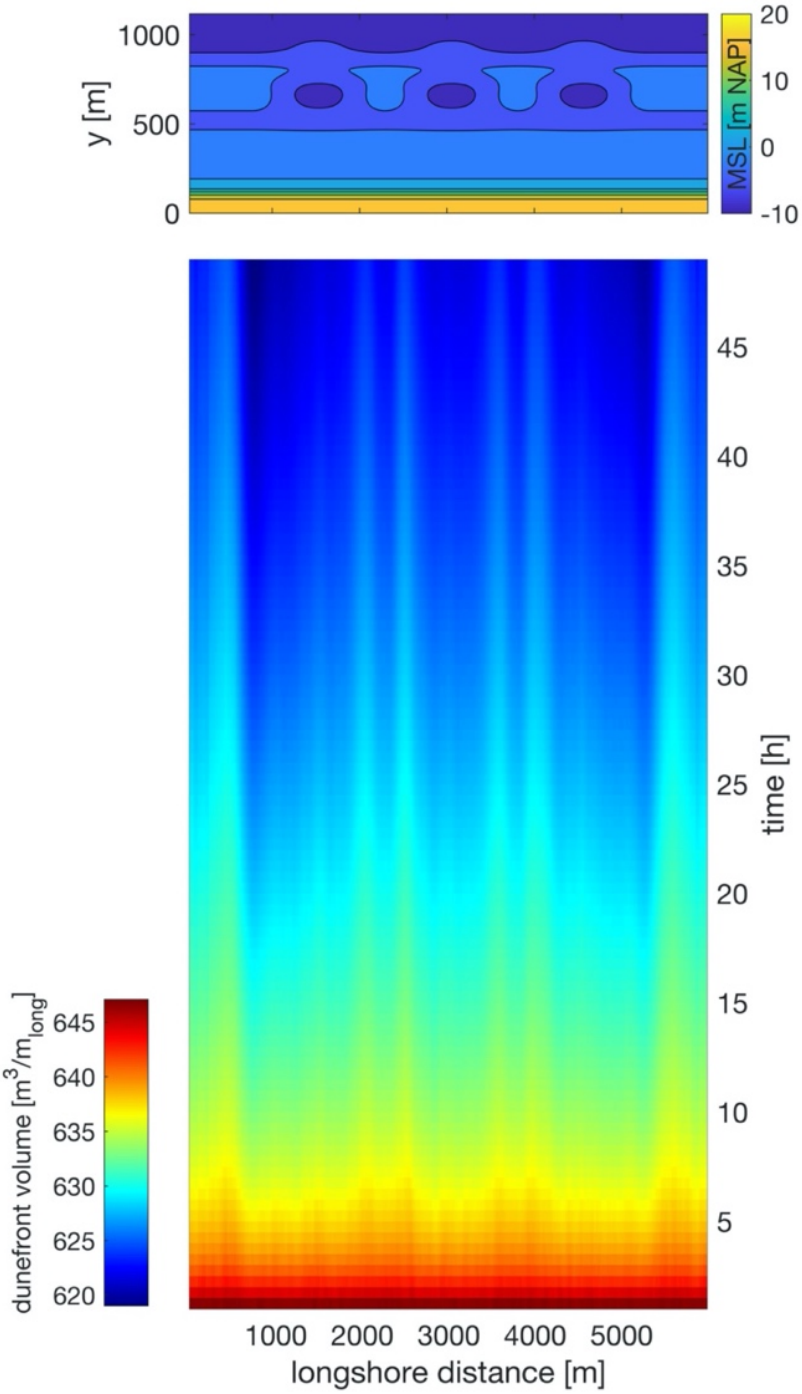

Figure 66: The upper panel in figure 66a displays the bathymetry with the location of the horns and bays for phase SNSaC. The bottom panels show the volume of the dune front per longshore meter over time.

8B.4.2 *SNSbC*

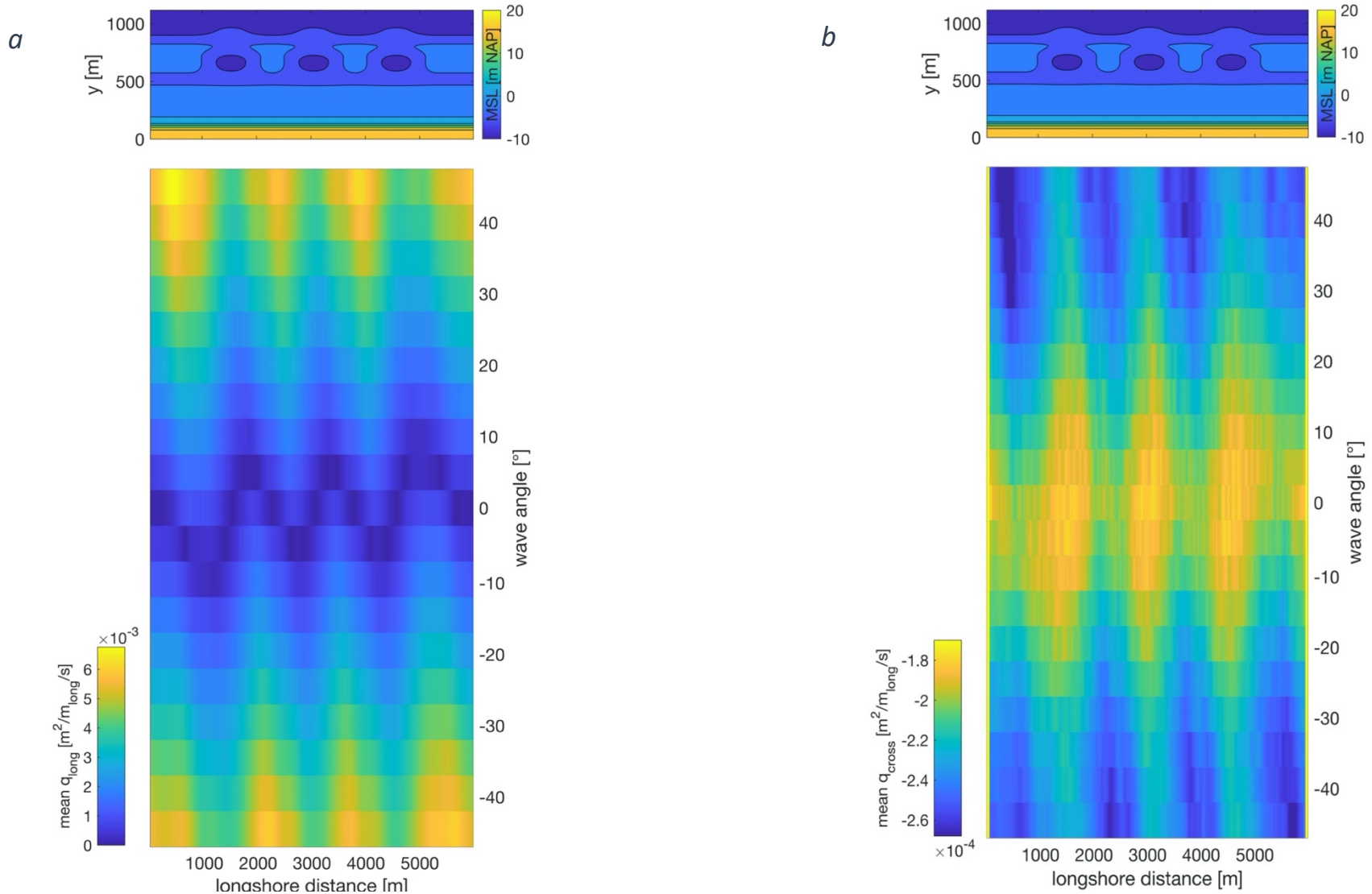

Figure 67: The upper panel in both 67a and 67b displays the bathymetry with the location of the horns and bays. Figure 67a shows the mean longshore sediment transport per metre per second in the longshore dimension at 5 °intervals. Figure 67b represents the cross-shore component of sediment transport for every 5 °interval.

8B.4.3 *SNSaV*

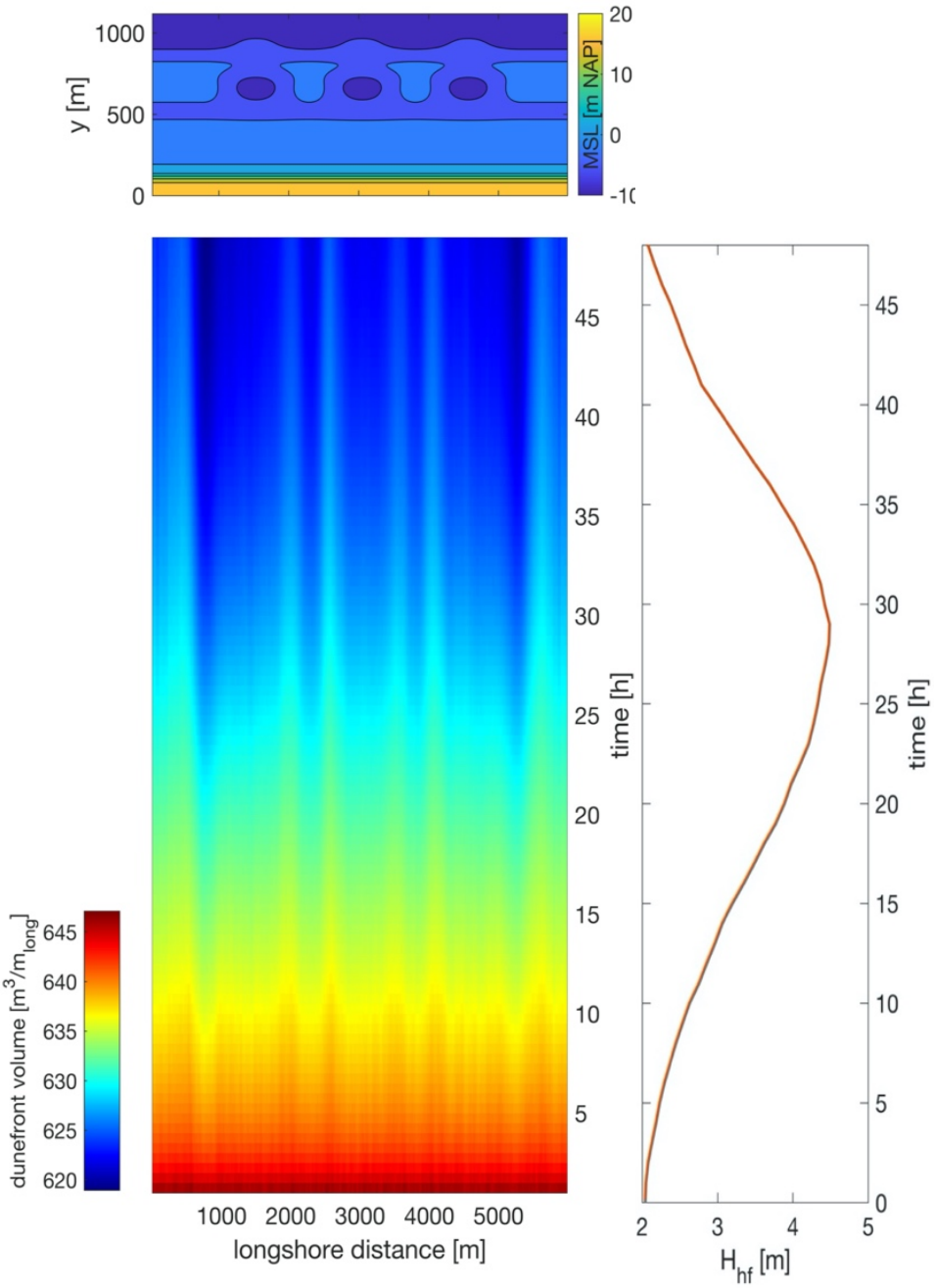

Figure 68: The upper panel in figure 68 displays the bathymetry with the location of the horns and bays. The bottom panels show the mean volume of the dune front per longshore metre over time for respectively phase SNSaV. *The right-hand panel displays the* H_s.

References

Aagaard, T., Kroon, A., Andersen, S., Møller Sørensen, R., Quartel, S., & Vinther, N. (2005). Intertidal beach change during storm conditions; Egmond, The Netherlands. *Marine Geology*, *218*(1–4), 65–80. https://doi.org/10.1016/j.margeo.2005.04.001

Andrews, D. G., & Mcintyre, M. E. (1978). An exact theory of nonlinear waves on a Lagrangian-mean flow. *Journal of Fluid Mechanics*, *89*(4), 609–646. https://doi.org/10.1017/s0022112078002773

Arens, S. M. (1996). Rates of aeolian transport on a beach in a temperate humid climate. *Geomorphology*, *17*(1–3), 3–18. https://doi.org/10.1016/0169-555x(95)00089-n

Arens, S. M., Mulder, J. P. M., Slings, Q. L., Geelen, L. H. W. T., & Damsma, P. (2013). Dynamic dune management, integrating objectives of nature development and coastal safety: Examples from the Netherlands. *Geomorphology*, *199*, 205–213. https://doi.org/10.1016/j.geomorph.2012.10.034

Armaroli, C., Grottoli, E., Harley, M. D., & Ciavola, P. (2013). Beach morphodynamics and types of foredune erosion generated by storms along the Emilia-Romagna coastline, Italy. *Geomorphology*, *199*, 22–35. https://doi.org/10.1016/j.geomorph.2013.04.034

Battjes, J. A., & Janssen, J. P. F. M. (1978). *Energy loss and set-up due to breaking random waves*. 16th Conference on Coastal Engineering, Hamburg, Germany.

Battjes, J. A., Bakkenes, H. J., Janssen, T. T., & van Dongeren, A. R. (2004). Shoaling of subharmonic gravity waves. *Journal of Geophysical Research*, *109*(C2), 1–15. https://doi.org/10.1029/2003jc001863

Bertin, X., de Bakker, A., van Dongeren, A., Coco, G., André, G., Ardhuin, F., Bonneton, P., Bouchette, F., Castelle, B., Crawford, W. C., Davidson, M., Deen, M., Dodet, G., Guérin, T., Inch, K., Leckler, F., McCall, R., Muller, H., Olabarrieta, M., … Tissier, M. (2018). Infragravity waves: From driving mechanisms to impacts. *Earth-Science Reviews*, *177*, 774–799. https://doi.org/10.1016/j.earscirev.2018.01.002

Bowen, A. J., & Inman, D. L. (1971). Edge waves and crescentic bars. *Journal of Geophysical Research*, *76*(36), 8662–8671. https://doi.org/10.1029/jc076i036p08662

Brown, J., & Bearman, G. (2013). *Waves, Tides and Shallow-Water Processes* (2de editie). Elsevier Gezondheidszorg.

Callaghan, D. P., Ranasinghe, R., & Roelvink, D. (2013). Probabilistic estimation of storm erosion using analytical, semi-empirical, and process-based storm erosion models. *Coastal Engineering*, *82*, 64–75. https://doi.org/10.1016/j.coastaleng.2013.08.007

de Bakker, A. T. M., Tissier, M. F. S., & Ruessink, B. G. (2014). Shoreline dissipation of infragravity waves. *Continental Shelf Research*, *72*, 73–82. https://doi.org/10.1016/j.csr.2013.11.013

de Bakker, A. T. M., Herbers, T. H. C., Smit, P. B., Tissier, M. F. S., & Ruessink, B. G. (2015). Nonlinear Infragravity–Wave Interactions on a Gently Sloping Laboratory Beach. *Journal of Physical Oceanography*, *45*(2), 589–605. https://doi.org/10.1175/jpo-d-14-0186.1

De Vet, P.L.M., McCall, R.T., Den Bieman, J.P., van Ormondt, M., Stive, M.J.F. (2015). *Modelling dune erosion, overwash and breaching at fire island (NY) during hurricane Sandy.* Paper Presented at the Proc. Coastal Sediments. https://doi.org/10.1142/9789814689977_0006

De Winter, R. C., Gongriep, F., & Ruessink, B. G. (2015). Observations and modeling of alongshore variability in dune erosion at Egmond aan Zee, the Netherlands. *Coastal Engineering*, *99*, 167–175. https://doi.org/10.1016/j.coastaleng.2015.02.005

Elfrink, B., & Baldock, T. (2002). Hydrodynamics and sediment transport in the swash zone: a review and perspectives. *Coastal Engineering*, *45*(3–4), 149–167. https://doi.org/10.1016/s0378-3839(02)00032-7

Elfrink, B., Hanes, D. M., & Ruessink, B. G. (2006). Parameterization and simulation of near bed orbital velocities under irregular waves in shallow water. *Coastal Engineering*, *53*(11), 915–927. https://doi.org/10.1016/j.coastaleng.2006.06.002

Erikson, L. H., Larson, M., & Hanson, H. (2007). Laboratory investigation of beach scarp and dune recession due to notching and subsequent failure. *Marine Geology*, 245(1–4), 1–19. https://doi.org/10.1016/j.margeo.2007.04.006

Funke, E. R., & Mansard, E. P. D. (1980). On the Synthesis of Realistic Sea States. *Coastal Engineering*, 2974–2991. https://doi.org/10.1061/9780872622647.179

Galappatti, G., & Vreugdenhil, C. B. (1985). A depth-integrated model for suspended sediment transport. *Journal of Hydraulic Research*, *23*(4), 359–377. https://doi.org/10.1080/00221688509499345

Gallagher, B. (1971). Generation of surf beat by non-linear wave interactions. *Journal of Fluid Mechanics*, *49*(1), 1–20. https://doi.org/10.1017/s0022112071001897

van Gent, M. R. A., van Thiel de Vries, J. S. M., Coeveld, E. M., de Vroeg, J. H., & van de Graaff, J. (2008). Large-scale dune erosion tests to study the influence of wave periods. *Coastal Engineering*, *55*(12), 1041–1051. https://doi.org/10.1016/j.coastaleng.2008.04.003

Guza, R. T., & Thornton, E. B. (1982). Swash oscillations on a natural beach. *Journal of Geophysical Research*, *87*(C1), 483. https://doi.org/10.1029/jc087ic01p00483

Guza, R. T., & Thornton, E. B. (1985). Observations of surf beat. *Journal of Geophysical Research*, *90*(C2), 3161. https://doi.org/10.1029/jc090ic02p03161

Harris, D. L. (1963). Characteristics of the Hurricane Storm Surge. *Weather Bureau Technical Papers*, 48, 1–144. Retrieved from https://play.google.com/books/reader?id=scj2tfIIAi8C&hl=nl&pg=GBS.PP3

Hasselmann, K., Barnett, T. P., Bouws, E., Carlson, H., Cartwright, D. E., Enke, K., Ewing, J. A., Gienapp, H., Hasselmann, D. E., Kruseman, P., Meerburg, A., Müller, P., Olbers, D. J., Richter, K., Sell, W., & Walden, H. (1973). Measurements of wind-wave growth and swell decay during the Joint North Sea Wave Project (JONSWAP). *Deutschen Hydrographischen Zeitschrift*, *8*(12), 1–94. https://repository.tudelft.nl/islandora/object/uuid:f204e188-13b9-49d8-a6dc-4fb7c20562fc

Henderson, S. M. (2002). Observations of surf beat forcing and dissipation. *Journal of Geophysical Research*, *107*(C11), 1–10. https://doi.org/10.1029/2000jc000498

Henderson, S. M., Guza, R. T., Elgar, S., Herbers, T. H. C., & Bowen, A. J. (2006). Nonlinear generation and loss of infragravity wave energy. *Journal of Geophysical Research*, 111(C12), 1–9. https://doi.org/10.1029/2006jc003539

Hibberd, S., & Peregrine, D. H. (1979). Surf and run-up on a beach: a uniform bore. *Journal of Fluid Mechanics*, 95(2), 323–345. https://doi.org/10.1017/s002211207900149x

Holman, R. A., & Sallenger, A. H. (1985). Setup and swash on a natural beach. *Journal of Geophysical Research*, *90*(C1), 945. https://doi.org/10.1029/jc090ic01p00945

Holman, R. A. (1986). Extreme value statistics for wave run-up on a natural beach. *Coastal Engineering*, *9*(6), 527–544. https://doi.org/10.1016/0378-3839(86)90002-5

Holthuijsen, L. H., Booij, N., & Herbers, T. H. C. (1989). A prediction model for stationary, short-crested waves in shallow water with ambient currents. *Coastal Engineering*, *13*(1), 23–54. https://doi.org/10.1016/0378-3839(89)90031-8

Hoonhout, B. (2015). *Introduction — XBeach pre-1.22.4344 documentation*. XBeach's documentation. https://XBeach.readthedocs.io/en/latest/XBeach_manual.html#processes-and-model-formulation

Huntley, D. A., Guza, R. T., & Bowen, A. J. (1977). A universal form for shoreline run-up spectra? *Journal of Geophysical Research*, 82(18), 2577–2581. https://doi.org/10.1029/jc082i018p02577

Kriebel, D. L., & Dean, R. G. (1985). Numerical simulation of time-dependent beach and dune erosion. *Coastal Engineering*, *9*(3), 221–245. https://doi.org/10.1016/0378-3839(85)90009-2

Larson, M., Erikson, L., & Hanson, H. (2004). An analytical model to predict dune erosion due to wave impact. *Coastal Engineering*, 51(8–9), 675–696. https://doi.org/10.1016/j.coastaleng.2004.07.00

Lin, Y.-H., & Hwung, H.-H. (2012). Infragravity wave generation by the shoaling wave groups over beaches. *China Ocean Engineering*, *26*(1), 1–18. https://doi.org/10.1007/s13344-012-0001-9

Lindemer, C. A., Plant, N. G., Puleo, J. A., Thompson, D. M., & Wamsley, T. V. (2010). Numerical simulation of a low-lying barrier island's morphological response to Hurricane Katrina. *Coastal Engineering*, *57*(11–12), 985–995. https://doi.org/10.1016/j.coastaleng.2010.06.004

Longuet-Higgins, M. S., & Stewart, R. W. (1962). Radiation stress and mass transport in gravity waves, with application to 'surf beats.' *Journal of Fluid Mechanic*s, 13(4), 481–504. https://doi.org/10.1017/s0022112062000877

Longuet-Higgins, M. S., & Stewart, R. (1964). Radiation stresses in water waves; a physical discussion, with applications. *Deep Sea Research and Oceanographic Abstracts*, *11*(4), 529–562. https://doi.org/10.1016/0011-7471(64)90001-4

McCall, R. T., Van Thiel de Vries, J. S. M., Plant, N. G., Van Dongeren, A. R., Roelvink, J. A., Thompson, D. M., & Reniers, A. J. H. M. (2010). Two-dimensional time dependent hurricane overwash and erosion modeling at Santa Rosa Island. *Coastal Engineering*, *57*(7), 668–683. https://doi.org/10.1016/j.coastaleng.2010.02.006

Nairn, R. B., Roelvink, J. A. D., & Southgate, H. N. (1991). Transition Zone Width and Implications for Modelling Surfzone Hydrodynamics. *Coastal Engineering 1990*, 68–81. https://doi.org/10.1061/9780872627765.007

Nishi, R., & Kraus, N. C. (1996). MECHANISM AND CALCULATION OF SAND DUNE EROSION BY STORMS. *Coastal Engineering Proceedings*, *1*(25). https://doi.org/10.9753/icce.v25.%p

Nishi, R., & Kraus, N. C. (1997). Mechanism and Calculation of Sand Dune Erosion by Storms. *Coastal Engineering 1996*, 3034–3047. https://doi.org/10.1061/9780784402429.235

Nielsen, A. F., Williams, B., McComb, P., & Treloar, P. D. (2015). *Infragravity wave processes: Recent experience in New Zealand and Australia*. Australasian Coasts & Ports Conference 2015: 22nd Australasian Coastal and Ocean Engineering Conference and the 15th Australasian Port and Harbour Conference. Auckland, New Zealand: Engineers Australia and IPENZ, 2015: 609-615.

Overton, M. F., Fisher, J. S., & Hwang, K.-N. (1995). Development of a Dune Erosion Model using SUPERTANK Data. *Coastal Engineering 1994*, 2488–2502. https://doi.org/10.1061/9780784400890.181

Palmsten, M. L., & Splinter, K. D. (2016). Observations and simulations of wave runup during a laboratory dune erosion experiment. *Coastal Engineering*, *115*, 58–66. https://doi.org/10.1016/j.coastaleng.2016.01.007

Reniers, A. J. H. M. (2004). Morphodynamic modeling of an embayed beach under wave group forcing. *Journal of Geophysical Research*, *109*(C1), 1–22. https://doi.org/10.1029/2002jc001586

Reniers, A. J. H. M. (2004). Morphodynamic modeling of an embayed beach under wave group forcing. *Journal of Geophysical Research*, *109*(C1), 1–22. https://doi.org/10.1029/2002jc001586

Roelvink, J. A. (1993). Dissipation in random wave groups incident on a beach. *Coastal Engineering*, *19*(1–2), 127–150. https://doi.org/10.1016/0378-3839(93)90021-y

Roelvink, D., Reniers, A., van Dongeren, A., van Thiel de Vries, J., McCall, R., & Lescinski, J. (2009). Modelling storm impacts on beaches, dunes and barrier islands. *Coastal Engineering*, *56*(11–12), 1133–1152. https://doi.org/10.1016/j.coastaleng.2009.08.006

Roelvink, D., McCall, R., Mehvar, S., Nederhoff, K., & Dastgheib, A. (2018). Improving predictions of swash dynamics in XBeach: The role of groupiness and incident-band runup. *Coastal Engineering*, *134*, 103–123. https://doi.org/10.1016/j.coastaleng.2017.07.004

Ruessink, B. G. (1998). Bound and free infragravity waves in the nearshore zone under breaking and nonbreaking conditions. *Journal of Geophysical Research: Oceans*, *103*(C6), 12795–12805. https://doi.org/10.1029/98jc00893

Ruessink, G., Schwarz, C. S., Price, T. D., & Donker, J. J. A. (2019). A Multi-Year Data Set of Beach-Foredune Topography and Environmental Forcing Conditions at Egmond aan Zee, The Netherlands. *Data*, *4*(2), 73. https://doi.org/10.3390/data4020073

Sallenger, A. H. (2000). Storm Impact Scale for Barrier Islands. *Journal of Coastal Research*, *16*(3), 890–895. https://www.jstor.org/stable/4300099

Schäffer, H. A. (1993). Infragravity waves induced by short-wave groups. *Journal of Fluid Mechanics*, *247*, 551–588. https://doi.org/10.1017/s0022112093000564

Shen, M. C., & Meyer, R. E. (1963). Climb of a bore on a beach Part 3. Run-up. *Journal of Fluid Mechanics*, *16*(01), 113. https://doi.org/10.1017/s0022112063000628

Smit, P. B., Stelling, G. S., Roelvink, D., van Thiel de Vries, J., McCall, R., van Dongeren, A., Zwinkels, C., & Jacobs, R. (2010, januari). *XBeach: Non-hydrostatic model Validation, verification and model description*. https://www.researchgate.net/publication/257305594_XBeach_Nonhydrostatic_model_Validation_verification_and_model_description

Splinter, K. D., & Palmsten, M. L. (2012). Modeling dune response to an East Coast Low. *Marine Geology*, *329–331*, 46–57. https://doi.org/10.1016/j.margeo.2012.09.005

Stockdon, H. F., Thompson, D. M., Plant, N. G., & Long, J. W. (2014). Evaluation of wave runup predictions from numerical and parametric models. *Coastal Engineering*, *92*, 1–11. https://doi.org/10.1016/j.coastaleng.2014.06.004

Suhayda, J. N. (1974). Standing waves on beaches. *Journal of Geophysical Research*, *79*(21), 3065–3071. https://doi.org/10.1029/jc079i021p03065

Symonds, G., Huntley, D. A., & Bowen, A. J. (1982). Two-dimensional surf beat: Long wave generation by a time-varying breakpoint. *Journal of Geophysical Research*, *87*(C1), 492. https://doi.org/10.1029/jc087ic01p00492

Thomson, J., Elgar, S., Raubenheimer, B., Herbers, T. H. C., & Guza, R. T. (2006). Tidal modulation of infragravity waves via nonlinear energy losses in the surfzone. *Geophysical Research Letters*, *33*(5), 1–4. https://doi.org/10.1029/2005gl025514

Thornton, E. B., MacMahan, J., & Sallenger, A. H. (2007). Rip currents, mega-cusps, and eroding dunes. *Marine Geology*, *240*(1–4), 151–167. https://doi.org/10.1016/j.margeo.2007.02.018

Tissier, M., Bonneton, P., & Ruessink, B.G. (2017). Infragravity waves and bore merging. *Coastal dynamics*, 451-460.

Ursell, F. (1952). Edge waves on a sloping beach. *Proceedings of the Royal Society of London. Series A. Mathematical and Physical Sciences*, *214*(1116), 79–97. https://doi.org/10.1098/rspa.1952.0152

Van Dongeren, A. (2003). Numerical modeling of infragravity wave response during DELILAH. *Journal of Geophysical Research*, *108*(C9), 3288. https://doi.org/10.1029/2002jc001332

van Dongeren, A., Battjes, J., Janssen, T., van Noorloos, J., Steenhauer, K., Steenbergen, G., & Reniers, A. (2007). Shoaling and shoreline dissipation of low-frequency waves. *Journal of Geophysical Research*, *112*(C2), C02011. https://doi.org/10.1029/2006jc003701

Van Dongeren, A., Bolle, A., Vousdoukas, M. I., Plomaritis, T., Eftimova, P., Williams, J., Armaroli, C., Idier, D., Van Geer, P., Van Thiel de Vries, J., Haerens, P., Taborda, R., Benavente, J., Trifonova, E., Ciavola, P., Balouin, Y., & Roelvink, D. (2009). 82. MICORE: DUNE EROSION AND OVERWASH MODEL VALIDATION WITH DATA FROM NINE EUROPEAN FIELD SITES. *Proceedings of Coastal Dynamics 2009*, 1–15. https://doi.org/10.1142/9789814282475_0084

Van Thiel De Vries, J., Dongeren, A.V., McCall, R., Reniers, A., 2011. The effect of the longshore dimension on dune erosion. 32nd International Conference on Coastal Engineering. ICCE 2010, June 30–July 5 2010, Shanghai, China.

Vellinga, P. (1982). Beach and dune erosion during storm surges. *Coastal Engineering*, *6*(4), 361–387. https://doi.org/10.1016/0378-3839(82)90007-2

Walstra, D. J. R., Roelvink, J. A., & Groeneweg, J. (2001). Calculation of Wave-Driven Currents in a 3D Mean Flow Model. *Coastal Engineering 2000*, 1050–1063. https://doi.org/10.1061/40549(276)81

Warming, R. F., & Beam, R. M. (1976). Upwind Second-Order Difference Schemes and Applications in Aerodynamic Flows. *AIAA Journal*, *14*(9), 1241–1249. https://doi.org/10.2514/3.61457

Woth, K., Weisse, R., & von Storch, H. (2005). Climate change and North Sea storm surge extremes: an ensemble study of storm surge extremes expected in a changed climate projected by four different regional climate models. *Ocean Dynamics*, *56*(1), 3–15. https://doi.org/10.1007/s10236-005-0024-3